

Supermassive Black Holes with High Accretion Rates in Active Galactic Nuclei. XV. Reverberation Mapping of Mg II Emission Lines

HUA-RUI BAI,^{1,2} PU DU,¹ CHEN HU,¹ YONG-JIE CHEN,^{1,3} ZHU-HENG YAO,^{4,5} YAN-RONG LI,¹ YI-XIN FU,^{1,2} YI-LIN WANG,^{1,2}
YU ZHAO,^{1,2} HAO ZHANG,^{1,2} JUN-RONG LIU,¹ SEN YANG,⁶ YUE-CHANG PENG,¹ FENG-NA FANG,¹ YU-YANG SONGSHENG,^{1,3}
MING XIAO,¹ SHUO ZHAI,⁷ SHA-SHA LI,⁸ KAI-XING LU,⁸ ZHI-XIANG ZHANG,⁹ DONG-WEI BAO,⁴ WEI-JIAN GUO,⁷ JIA-QI FENG,^{1,2}
YI-PENG ZHAO,^{1,2} JESÚS ACEITUNO,^{10,11} JIN-MING BAI,⁸ LUIS C. HO^{12,13} AND JIAN-MIN WANG^{1,14,4}
(SEAMBH COLLABORATION)

- ¹Key Laboratory for Particle Astrophysics, Institute of High Energy Physics, Chinese Academy of Sciences, 19B Yuquan Road, Beijing 100049, China;
dupu@ihep.ac.cn, wangjm@mail.ihep.ac.cn
²School of Physics, University of Chinese Academy of Sciences, Beijing 100049, China
³Dongguan Neutron Science Center, 1 Zhongziyuan Road, Dongguan 523808, China
⁴National Astronomical Observatories of China, Chinese Academy of Sciences, 20A Datun Road, Beijing 100101, China
⁵Key Laboratory of Space Astronomy and Technology, National Astronomical Observatories, Chinese Academy of Sciences, Beijing 100101, China
⁶College of Physics and Electrical Engineering, Anyang Normal University, Anyang, Henan 455000, China
⁷Key Laboratory of Optical Astronomy, National Astronomical Observatories, Chinese Academy of Sciences, Beijing 100101, China
⁸Yunnan Observatories, Chinese Academy of Sciences, Kunming 650011, China
⁹College of Physics and Information Engineering, Quanzhou Normal University, Quanzhou, Fujian 362000, China
¹⁰Centro Astronomico Hispano Alemán, Sierra de los filabres sn, E-04550 Gergal. Almería, Spain
¹¹Instituto de Astrofísica de Andalucía (CSIC), Glorieta de la astronomía sn, E-18008 Granada, Spain
¹²The Kavli Institute for Astronomy and Astrophysics, Peking University, Beijing 100871, China
¹³Department of Astronomy, School of Physics, Peking University, Beijing 100871, China
¹⁴School of Astronomy and Space Sciences, University of Chinese Academy of Sciences, Beijing 100049, China

ABSTRACT

As the 15th paper in a series reporting on a large reverberation mapping (RM) campaign of super-Eddington accreting massive black holes (SEAMBHs) in active galactic nuclei (AGNs), we present the results of measurements of the Mg II lines in 18 SEAMBHs monitored spectroscopically from 2017 to 2024. Among these, the time lags of Mg II have been successfully determined for 8 of the 18 objects, thereby expanding the current Mg II RM sample, particularly at higher accretion rates. By incorporating measurements of the line widths, we determine the masses of their central supermassive black holes. Based on these new measurements, we update the relation between the Mg II radius and the monochromatic luminosity at 3000 Å ($R_{\text{MgII}} - L_{3000}$ relation), yielding a slope of 0.24 ± 0.03 , which is slightly shallower than, yet still consistent with, previously reported values. Similar to the H β lines, the Mg II time lags in SEAMBHs are shorter than those of AGNs with normal accretion rates at comparable luminosities. The deviation of AGNs from the best-fit $R_{\text{MgII}} - L_{3000}$ relation shows a strong correlation with the accretion rate, while no significant correlation is found between the deviation and the flux ratio of UV iron to Mg II.

Keywords: Active galactic nuclei (16); Quasars (1319); Supermassive black holes (1663); Reverberation mapping (2019)

1. INTRODUCTION

Accurate determination of the mass of supermassive black hole (SMBH) is crucial for understanding the evolution of SMBHs over cosmic timescales and their co-evolution with host galaxies (e.g., Ferrarese & Ford 2005; Kormendy & Ho 2013). In the past three decades, reverberation mapping (RM, e.g., Blandford & McKee 1982; Peterson 1993) has been demonstrated as an effective way to measure the masses of SMBHs in the centers of active galactic nuclei

(AGNs). The underlying physics of this approach is based on the nearly virial kinematics of the gas in broad-line regions (BLRs), which are primarily governed by the gravitational potential of the central SMBHs (e.g., Peterson & Wandel 1999, 2000; Onken & Peterson 2002). RM determines the sizes of BLRs through measuring the time delays between variations of broad emission lines and those of the continuum

fluxes. Then the SMBH mass can be obtained by

$$M_{\bullet} = f \frac{\Delta V^2 R_{\text{BLR}}}{G}, \quad (1)$$

where $R_{\text{BLR}} = c\tau$ represents the typical size of the BLR, c is the speed of light, τ is the time lag, G is the gravitational constant, ΔV is the width of the emission line, and f is a factor that accounts for the geometry, kinematics, and inclination of the BLR.

However, RM remains a resource-intensive observational technique, requiring extensive telescope time, which limits its practicality for large samples of AGNs. For AGNs with only single-epoch spectroscopic data, an empirical correlation between continuum luminosity and BLR size (called “radius-luminosity relation”, see e.g., Kaspi et al. 2000; Bentz et al. 2013), as established through RM campaigns in the past decades, enables mass estimation of their SMBHs despite the absence of direct RM measurements. The single-epoch virial mass estimation method, which combines the radius-luminosity relation with broad emission-line width measurements, has been widely applied to large AGN samples from the local universe to high redshifts and provided the foundation for our current knowledge of AGN evolution (e.g., Greene & Ho 2005; Vestergaard & Peterson 2006; Shen et al. 2011; Yang et al. 2023).

Most RM campaigns (e.g., Peterson et al. 1998; Kaspi et al. 2000; Bentz et al. 2010; Grier et al. 2012; Du et al. 2014; Barth et al. 2015; De Rosa et al. 2018; U et al. 2022; Shen et al. 2024; Woo et al. 2024) primarily focus on $H\beta$ emission lines. This preference is due to the accessibility of $H\beta$ in the optical spectra obtained with ground-based telescopes, and older spectrographs and CCDs were mainly sensitive to blue wavelengths. Additionally, the flux of $H\beta$ can be calibrated more easily using the adjacent narrow $[\text{O III}]\lambda 5007$ emission line, which is commonly employed as a reliable reference for flux calibration in most RM campaigns. Through these RM campaigns, the radius-luminosity relation for $H\beta$ (hereafter referred to as the $R_{H\beta} - L_{5100}$ relation) has been relatively well established (e.g., Kaspi et al. 2000; Bentz et al. 2013) and can be applied as the single-epoch mass estimator for low-redshift AGNs.

For AGNs with redshifts $z \gtrsim 1$, the $H\beta$ line falls outside the optical band. In such cases, the $\text{Mg II } \lambda 2800$ emission line serves as the primary diagnostic for AGNs in the range $1 \lesssim z \lesssim 2$, while $\text{C IV } \lambda 1549$ becomes the dominant feature at $2 \lesssim z \lesssim 4$. Accordingly, for AGNs at higher redshifts where $H\beta$ becomes observationally inaccessible, ultraviolet emission lines such as Mg II (and in some cases C IV) must be employed as surrogate virial indicators. Prior to the development of robust Mg II radius-luminosity relations, currently limited by the scarcity of high-quality RM campaigns for Mg II (and also for C IV), the single-epoch mass estimators calibrated either based on the SMBH masses derived from $H\beta$ RM measurements (e.g., McLure & Jarvis 2002; Wang et al. 2009; Bahk et al. 2019) or based on the established $R_{H\beta} - L_{5100}$ relation (e.g., McGill et al. 2008; Woo et al. 2018; Le et al. 2020) were adopted. Nevertheless, the validity of

these Mg II calibrations (effectively extrapolations from the $H\beta$ lines) requires rigorous verification through direct Mg II RM measurements. Furthermore, implementing SMBH mass measurements derived explicitly from Mg II lag measurements, rather than relying on $H\beta$ -based “extrapolation”, could potentially yield significant improvements in mass estimation accuracy.

Moreover, considering that the Mg II line may be dominated by collisional excitation, unlike the recombination lines (e.g., $H\beta$ and $H\alpha$), a question arises regarding the existence of a solid radius-luminosity relation for the Mg II line. Theoretically, calculations based on CLOUDY models (e.g., Korista & Goad 2000; Guo et al. 2020; Du et al. 2023) suggest that the Mg II line exhibits a relatively weaker response to continuum variations compared to $H\beta$, implying that RM results may be more challenging to obtain for Mg II . This could be attributed to the larger optical depth for the Mg II line. For a given continuum flux, compared to recombination lines, Mg II line photons originating close to the continuum sources are less likely to escape. Consequently, flux variations tend to be dominated by gas clouds at larger radii, where variations in the continuum may be diluted (e.g., Korista & Goad 2004; Yang et al. 2020). From an observational perspective, prior to successful RM measurements, variations in the Mg II lines were indeed found to respond to continuum emission variations; however, these responses exhibited smaller amplitudes compared to those of $H\beta$, as shown in multi-epoch observations (e.g., Kokubo et al. 2014; Sun et al. 2015; Zhu et al. 2017; Yang et al. 2020). In contrast, some studies (e.g., Goad et al. 1999; Trevese et al. 2007; Woo 2008; Hryniewicz et al. 2014; Cackett et al. 2015) found that the Mg II lines in certain AGNs did not show significant variations despite substantial changes in the continuum, highlighting the difficulties in obtaining RM results for Mg II .

With the investment of more observational resources, successful Mg II RM observations gradually occur although the number of objects is still limited (e.g., Metzroth et al. 2006; Shen et al. 2016; Lira et al. 2018; Czerny et al. 2019; Homayouni et al. 2020; Zajaček et al. 2020; Prince et al. 2022, 2023; Yu et al. 2021, 2023). Specifically, two relatively large samples are from Sloan Digital Sky Survey (SDSS) RM (Homayouni et al. 2020; Shen et al. 2024) and Australian Dark Energy Survey (OzDES) RM (Yu et al. 2023) projects. Homayouni et al. (2020) reported Mg II lags for 57 quasars, among which 24 were identified as “gold sample” with most reliable measurements of lags. Shen et al. (2024) further expanded the sample by reporting lag measurements for 125 objects in the final results of the SDSS-RM project. Additionally, Yu et al. (2023) presented Mg II lags for 25 quasars. With the limited samples of successful and accurate Mg II measurements, merely a preliminary radius-luminosity relation of Mg II (hereafter $R_{\text{MgII}} - L_{3000}$ relation) was built (e.g., Homayouni et al. 2020; Yu et al. 2023; Shen et al. 2024). The slope of the derived $R_{\text{MgII}} - L_{3000}$ relation is around 0.3, which is shallower than the typical slope (~ 0.5) of the $R_{H\beta} - L_{5100}$ in

Bentz et al. (2013). In order to refine $R_{\text{MgII}} - L_{3000}$ relation, more RM observations for Mg II lines are highly required.

Moreover, recent studies have shown that super-Eddington AGNs exhibit shorter $H\beta$ time lags compared to AGNs with normal accretion rates at the same luminosities, suggesting that the accretion rate is a parameter that influences the scatter of the $R_{H\beta} - L_{5100}$ relation (e.g., Du et al. 2015, 2016a, 2018a; Du & Wang 2019). Martínez-Aldama et al. (2020) found a similar phenomenon in the $R_{\text{MgII}} - L_{3000}$ relation for Mg II, indicating that its scatter may be also primarily driven by the accretion rate. To further investigate the possible dependency of the scatter of $R_{\text{MgII}} - L_{3000}$ on the accretion rate, it is essential to expand the RM sample of Mg II lines, particularly by including AGNs with high accretion rates.

As the fifteenth paper of the series reporting the RM campaign of super-Eddington accreting massive black holes (SEAMBHs) in AGNs, here we report the results of Mg II lines in eighteen luminous quasars with high accretion rates at intermediate redshift to advance the investigation of $R_{\text{MgII}} - L_{3000}$ relation. The time lags of eight among them are successfully measured and the latest $R_{\text{MgII}} - L_{3000}$ relation were established based on this sample and the historical samples. The paper is organized as follows. In Section 2, we describe the target selection, observation, and data reduction. The data analyses and measurements are provided in Section 3, including the mean and root-mean-square (rms) spectra, the light curves, the line widths, the time lags, and the SMBH masses. The $R_{\text{MgII}} - L_{3000}$ relation based on this new sample is provided in Section 4. Discussions regarding the comparison between the Mg II and $H\beta$ lags, as well as the implications of the shortened lags, are given in Section 5. Section 6 offers a brief summary. Throughout the paper, we use the standard Λ CDM cosmology with $H_0 = 67 \text{ km s}^{-1} \text{ Mpc}^{-1}$, $\Omega_M = 0.32$ and $\Omega_\Lambda = 0.68$ (Planck Collaboration et al. 2020).

2. OBSERVATIONS AND DATA REDUCTION

2.1. Target Selection

We selected the SEAMBH targets for Mg II measurements primarily based on the dimensionless accretion rate derived from the standard accretion disk model (e.g., Du et al. 2014, 2018a). The accretion rate, based on the monochromatic luminosity L_{3000} at 3000\AA , is given by

$$\dot{M} = 7.0 \left(\frac{\ell_{44}}{\cos i} \right)^{3/2} m_7^{-2} \quad (2)$$

where $\ell_{44} = L_{3000}/10^{44} \text{ erg s}^{-1}$, and $m_7 = M_\bullet/10^7 M_\odot$ is the SMBH mass. Here, i denotes the inclination angle of the disk relative to the line of sight, and we adopt $\cos i = 0.75$ as a typical value throughout this paper (see further details in Du et al. 2016a).

We sorted the quasars from SDSS Data Release 7 (Shen et al. 2011) by their accretion rates and selected targets with the highest values. Only those targets with redshifts ($z = 0.7 - 0.9$) for which the Mg II emission lines fall within the wavelength range where the spectrographs (described in Section 2.2) exhibit the highest sensitivity, along with SDSS r' -

band magnitudes brighter than 17.5, were selected, ensuring that we could achieve optimal signal-to-noise ratios (S/N). Additionally, only objects suitable for the observational seasons and the latitude of the observatories (see Section 2.2) with predicted time lags in the observed frames of less than 450 days were considered. During the target selection process for the present sample, there were very few successful Mg II RM observations; therefore, we assumed that the Mg II and $H\beta$ lags are the same and simply estimated the Mg II lags by the $R_{H\beta} - L_{5100}$ relation, given that their line widths are not significantly different (e.g., McLure & Jarvis 2002; Shen et al. 2008; Wang et al. 2009). The SDSS names and redshifts of the 18 selected targets in the present sample are listed in Table 1.

2.2. Spectroscopy and Photometry

The Mg II campaign started from the fall of 2017. Spectroscopic and photometric observations of twelve targets were conducted using the Lijiang 2.4 m telescope at the Yunnan Observatories of the Chinese Academy of Sciences. Additionally, observations of six other targets were carried out at the 2.2 m telescope of the Calar Alto Astronomical Observatory, part of the Centro Astronómico Hispano en Andalucía (CAHA) in Spain. The locations of the observations and the detailed monitoring periods are listed in Table 1. The spectroscopic and photometric observations at the Lijiang and CAHA are briefly described below.

2.2.1. Spectroscopy

Data were collected using the Yunnan Faint Object Spectrograph and Camera (YFOSC) mounted on the Lijiang 2.4 m telescope, and the Calar Alto Faint Object Spectrograph (CAFOS) on the CAHA 2.2 m telescope. Both instruments are capable of performing spectroscopic and photometric observations. Due to the absence of narrow emission lines in the vicinity of the Mg II lines, we employed a comparison-star-based calibration method for our spectroscopic observations. The field de-rotators of the Lijiang 2.4 m and CAHA 2.2 m telescopes allow the slits to rotate, accommodating a nearby comparison star (listed in Table 1) while simultaneously exposing the target, thereby enabling the star to serve as the flux calibration standard.

With the in-slit comparison star, we achieved accurate relative flux measurements, even under relatively poor weather conditions (e.g., Maoz et al. 1990; Kaspi et al. 2000; Du et al. 2014). The typical separation between the target and the chosen comparison star was approximately 1-3 arcminutes. More details regarding this comparison-star-based calibration method can be found in, e.g., Du et al. (2014) and Du et al. (2018a). To minimize light loss, we utilized long slits with relatively broad widths ($5.05''$ at Lijiang and $3''$ at CAHA). We used Grism 3 at Lijiang, which provided a wavelength coverage of $3400 - 9100 \text{ \AA}$ and a dispersion of $2.9 \text{ \AA pixel}^{-1}$, and Grism G-200 at CAHA, which covered a wavelength range of $4000 - 8500 \text{ \AA}$ with a dispersion of $4.47 \text{ \AA pixel}^{-1}$. The typical exposure time for each observation was 1800 seconds.

To mitigate the impact of cosmic rays, we conducted two consecutive exposures for each epoch, which were combined to produce the individual-night spectra. All spectra were extracted using a uniform aperture of 30 pixels (approximately 8.5 arcseconds), with background windows of [-26 pixels, -50 pixels] and [26 pixels, 50 pixels] on the left and right sides (both for the Lijiang and CAHA data). Wavelength calibration was performed based on the standard neon and helium lamps. The data were reduced using the standard IRAF v2.16.

Flux calibration was performed using a two-step procedure. Firstly, we generated the fiducial spectra of the comparison stars using spectrophotometric standards (e.g., G191B2B, Feige 56, and Feige 34) during photometric nights (when conditions were good). Secondly, for each individual-night spectrum of the target/comparison star pair, we compared the flux of the in-slit star with that of the fiducial spectrum to generate a wavelength-dependent sensitivity function, which was then applied to the target spectrum for flux calibration (see also Du et al. 2014 and Du et al. 2018a).

2.2.2. Photometry

As a double check on the accuracy of the flux calibration for the spectroscopic observations and to ensure that the comparison stars did not exhibit significant variability during the campaign, we also conducted photometric observations of the targets and comparison stars. We obtained three broad-band photometric images of the targets just prior to the spectral exposures each night, with typical exposure times of 80 seconds for each image. The filters used at Lijiang and CAHA are provided in Table 1.

The data were reduced using standard IRAF procedures for bias and flat-field correction. We performed differential photometry of the target and comparison stars with respect to 3-6 nearby reference stars in the same field of view. The fluxes of the targets and stars were extracted using circular apertures with radii of 4.2'' and 5'' for the Lijiang and CAHA observations, respectively. As shown in Appendix A, the comparison stars during the campaign are fairly stable.

To supplement and extend the coverage of the continuum light curves, we utilized archival time-domain photometric data from the Zwicky Transient Facility¹ (ZTF; see Masci et al. 2019). ZTF provides photometric light curves in three bands (ZTF-g, r, i). In our subsequent analysis, we adopted only the r band light curves from ZTF because the g band overlaps with the Mg II lines in wavelength, and the i band light curves provide less temporal coverage than those in the r band.

3. ANALYSIS

3.1. Mean and rms Spectra

The mean and root-mean-square (rms) spectra are always a useful way to quickly check the profiles of the emission lines

and to evaluate their variabilities during the RM campaign. The mean and rms spectra can be derived from the formula

$$\bar{F}_\lambda = \frac{1}{N} \sum_{i=1}^N F_\lambda^i, \quad (3)$$

and

$$S_\lambda = \left[\frac{1}{N} \sum_{i=1}^N (F_\lambda^i - \bar{F}_\lambda)^2 \right]^{1/2}, \quad (4)$$

where F_λ^i is the i -th spectrum of the object and N is the number of its spectra. For comparison, we also present the rms spectra generated from the residual spectra obtained after subtracting the power law and iron template components from the spectral fitting detailed in following Section 3.2. The mean spectra, rms spectra, and rms spectra generated from the residuals for all 18 targets throughout the campaign are shown in Figure 1.

Additionally, the observational uncertainties of spectra may be responsible for some of the signatures showing on the rms spectra. We also present the error spectra defined as

$$E_\lambda = \left[\frac{1}{N} \sum_{i=1}^N (e_\lambda^i)^2 \right]^{1/2} \quad (5)$$

in Figure 1, where e_λ^i is the observational error of the i -th spectrum at wavelength λ , as obtained from the IRAF spectrum extracting procedure. The error spectra clearly indicate that some features observed around the 3000 Å to 3200 Å wavelength range in the rest frames are attributable to observational errors (specifically the Poisson noise caused by the strong 5577 Å emission line from the atmosphere). Considering both the rms spectra and the error spectra, the Mg II variations in J082338, J084808, J092835, and J101730 are not significant.

3.2. Light Curves

The light curves of the H β emission lines can be measured using either a direct integration scheme (e.g., Peterson et al. 1998; Kaspi et al. 2000; Bentz et al. 2010; Du et al. 2014, 2018b) or a spectral fitting scheme (e.g., Barth et al. 2013; Hu et al. 2015, 2021; U et al. 2022; Woo et al. 2024). The advantages and disadvantages of these two schemes have been discussed in references such as Du et al. (2018b) and Hu et al. (2015). For Mg II lines, strong iron emission features are often present (e.g., Wills et al. 1980; Verner et al. 1999), which can influence the direct integration scheme due to their contributions and variabilities. Therefore, the fitting scheme is typically adopted for Mg II measurements (e.g., Prince et al. 2023; Yu et al. 2023).

Furthermore, for SEAMBHs, the relative strength of the iron emission in the UV and optical, with respect to H β (e.g., Boroson & Green 1992; Sulentic et al. 2000; Marziani et al. 2001; Shen & Ho 2014; Du et al. 2016b; Panda et al. 2019) and Mg II (e.g., Dong et al. 2011; Shin et al. 2021; Jiang et al. 2024; Pan et al. 2025), is generally stronger than that in

¹ <https://www.ztf.caltech.edu/>

AGNs with normal accretion rates. Consequently, we measured the flux of the Mg II lines in our sample using the fitting scheme.

The spectral fitting was performed using the software DASPEC² (Du 2024), which is a multi-component spectral fitting code for AGN spectra based on the Levenberg-Marquardt algorithm (Press et al. 1992) and features a user-friendly graphical interface. We adopted the following components in the fitting: (1) a power law to model the AGN continuum, (2) a UV iron template compiled by Shen et al. (2019) convolved with a Gaussian kernel to model the iron emission, and (3) two Gaussian functions to model the Mg II emission line. The template compiled by Shen et al. (2019) is a composite one: it incorporates the template from Salvander et al. (2007) for the wavelength range of 2200–3090 Å, and the template from Tsuzuki et al. (2006) for the range of 3090–3500 Å. Yu et al. (2021) tested three different iron templates from Vestergaard & Wilkes (2001), Tsuzuki et al. (2006), and Salvander et al. (2007) in their Mg II measurements and found that the three templates produced generally consistent results. As a simple test, we also performed the analysis by replacing the Salvander et al. (2007) template by the Tsuzuki et al. (2006) template and obtained fully consistent results. More details are provided in Appendix B. In addition, the contributions from the host galaxies in the spectra were not considered in the fitting, as they are expected to be negligible for the targets in our sample, given their high luminosities (Shen et al. 2011).

We first corrected for Galactic extinction (Schlafly & Finkbeiner 2011) and transformed the observed spectra to their rest frames, after which we performed the fitting in the wavelength range of 2260–3050 Å in those frames. For several objects (J084808, J085557, J091245, J092835 and J093857), a slightly smaller wavelength range (starts from ~2300 Å) was used due to their redshifts. An example of the spectral fitting results is illustrated in Figure 2. After subtracting the components of the power law and iron template, we obtained the Mg II light curves by integrating the fluxes of the residual spectra within the range of 2775–2825 Å, where the Mg II features in the RMS spectra are most significant (see Figure 1). The continuum light curves were generated by measuring the median fluxes in the range of 3000–3100 Å from the power-law components. The continuum light curves derived from the spectroscopic data generally agree well with the photometric light curves, indicating their reliability. Several obvious outliers in the light curves caused by bad weather conditions or inaccurate slit alignments were discarded.

3.3. Intercalibration of Continuum Light Curves

Due to the different apertures used in the spectroscopic and photometric observations, the continuum light curves at 3000 Å from the spectroscopic data and the ZTF r-band continuum light curves must be intercalibrated. The intercalibra-

tion was performed using the Bayesian package PYCALI³ (Li 2024a). This package assumes that the light curves can be modeled by a damped random walk and determines the optimal multiplicative and additive factors by exploring the posterior probability distribution using a diffusive nested sampling algorithm (details can be found in Li et al. 2014). The photometric and spectroscopic continuum light curves after intercalibration are shown in Figure 3 and Appendix C. The consistency between the photometric and spectroscopic continuum light curves demonstrates the effectiveness of the intercalibration process. The light curves after the intercalibration for all 18 targets are provided in Table 2. For subsequent analysis, the photometric and spectroscopic light curves were combined by averaging the observations taken during the same nights.

3.4. Variability

The variability amplitudes and the corresponding uncertainties of the light curves can be quantified by

$$F_{\text{var}} = \frac{(\sigma^2 - \Delta^2)^{1/2}}{\langle F \rangle}, \quad (6)$$

and

$$\sigma_{\text{Fvar}} = \frac{1}{(2N)^{1/2} F_{\text{var}}} \frac{\sigma^2}{\langle F \rangle^2}, \quad (7)$$

where σ , Δ , $\langle F \rangle$, and N are the standard deviation, mean uncertainty, mean flux, and the number of data points of the light curve, respectively (e.g., Rodríguez-Pascual et al. 1997; Edelson et al. 2002). The variability amplitudes and uncertainties of the continuum and Mg II light curves are listed in Table 3. The Mg II variabilities of the present sample are generally lower than ~8%.

3.5. Time-lag Analysis

We employed the interpolated cross-correlation function (ICCF; e.g., Gaskell & Peterson 1987) and the MICA algorithm (Li et al. 2016) to determine the time lags of the Mg II lines in the present sample. Details of both methods can be found in the aforementioned references, and we provide a brief introduction here.

ICCF: ICCF is a commonly used method for determining time lags in RM analysis. We adopted the centroid of the CCF above a threshold of 80% of the peak value as the time lag (referred to as the centroid time lag) and utilized the cross-correlation centroid distributions (CCDs) through “flux randomization/random subset sampling (FR/RSS)” method (Peterson et al. 1998, 2004) to estimate the uncertainties.

MICA: MICA is a Bayesian-based non-parametric method that infers the one-dimensional transfer function from the light curves of the continuum and emission lines. This approach models the transfer function as a combination of one

² <https://github.com/PuDu-Astro/DASpec>

³ <https://github.com/LiyiAstroph/PyCALI>

or more Gaussian or Gamma functions. To derive the posterior distributions of the parameters, it employs the diffusive nested sampling technique. We assumed that the transfer function for the Mg II lines could be represented by a Gaussian function, and we used MICA to compute the corresponding transfer function. The time lag of Mg II was then determined from the centroids of these transfer functions. Ultimately, the median value of the centroid distribution obtained through nested sampling serves as the estimate of the time lag, with its uncertainty assessed using the 68.3% confidence interval.

It is evident that the time lags of the Mg II lines for some of our targets were not well constrained due to their relatively low variability and S/N ratios. We adopted a criterion of a maximum ICCF coefficient (r_{\max}) of 0.5 to determine whether the lags could be reliably measured; below this threshold, we consider the measurements of the Mg II line lag to be unreliable. Eight of our targets meet the criterion of $r_{\max} > 0.5$, and their light curves, along with time lag measurements from both ICCF and MICA, are presented in Figure 3. The light curves for the remaining ten targets, for which we believe the lag measurements were unsuccessful, are shown in Appendix C.

The time lags measured by ICCF and MICA in the observed frame (denoted as $\tau_{\text{ICCF}}^{\text{obs}}$ and $\tau_{\text{MICA}}^{\text{obs}}$) and in the rest frame (denoted as $\tau_{\text{ICCF}}^{\text{rest}}$ and $\tau_{\text{MICA}}^{\text{rest}}$) for the eight successful objects are listed in Table 4. The comparison between $\tau_{\text{ICCF}}^{\text{rest}}$ and $\tau_{\text{MICA}}^{\text{rest}}$ is illustrated in Figure 4. Generally, $\tau_{\text{ICCF}}^{\text{rest}}$ and $\tau_{\text{MICA}}^{\text{rest}}$ are consistent with one another. The time lags of the Mg II emission for the current sample in the observed frames typically range from 100 to 300 days. Considering that MICA employs the damped random walk model to reconstruct the light curves, it is expected to provide more reliable lag measurements, especially in cases with seasonal gaps. Therefore, we adopted the time lag results from MICA for the subsequent black hole mass measurements and analyses.

3.6. Line Width Measurements

To measure the masses of the SMBHs in these AGNs, it is essential to determine the line widths of the Mg II lines. We measured the full width at half maximum (FWHM) and the line dispersion (σ_{line} ; e.g., Peterson et al. 2004) from the line profiles in the mean spectra of the eight successful objects. The contributions from the iron emission beneath the Mg II lines were removed by the spectral fitting method outlined in Section 3.2. In this paper, we do not provide line width measurements from their root-mean-square (rms) spectra, as the Mg II profiles in the rms spectra are not well-defined due to low S/N ratios and variability amplitudes.

The uncertainties of the line widths were estimated using a bootstrap method. We first generated a subsample by randomly selecting N spectra from the original N spectra (with replacement) and then created the mean spectra for line width measurements based on this subsample. This procedure was repeated 500 times. The uncertainties of the line widths were determined from the 16th and 84th percentiles of the gen-

erated distributions. The instrumental broadening (FWHM $\sim 1200 \text{ km s}^{-1}$ for Lijiang and $\sim 1000 \text{ km s}^{-1}$ for CAHA), was then subtracted from the measured widths of both FWHM and σ_{line} . The instrumental broadening was estimated from the spectra of the comparison stars, by comparing the observed spectra of these stars with the high-resolution stellar spectra from the Indo-U.S. Library of Coudé Feed Stellar Spectra (Valdes et al. 2004, more details can be found in Du et al. 2016c).

The Mg II emission line is actually a doublet (2796.35 Å and 2803.53 Å, see, e.g., Morton 1991). Although we used two Gaussian functions in the fitting process (see Section 3.2), these Gaussians do not precisely represent the doublet since we did not fix their wavelengths (or the wavelength separation) to 2796.35 Å and 2803.53 Å (or ~ 7.18 Å). The widths and velocity shifts of the two Gaussians were treated as free parameters during the fitting. Therefore, the line widths measured from the combination of the two Gaussians (here we practically measured the line widths from the residuals after subtracting the power law and Fe II components) may slightly deviate from the intrinsic velocity broadening of each component of the doublet. We estimated the influence of the line width measurements from the wavelength shift of the doublet by assuming that the flux ratio of the doublets is close to 1 (e.g., Marziani et al. 2013; Popović et al. 2019) and that the intrinsic FWHM is 3000 km s^{-1} (which is similar to the typical value for our sample). This leads to the line widths measured from the combination of the doublets being larger than the intrinsic values by approximately 140 km s^{-1} for FWHM and approximately 60 km s^{-1} for σ_{line} , respectively. Consequently, these values were included as additional uncertainties in the lower error bars.

3.7. Measurement of SMBH Masses

The SMBH masses can be determined using Equation (1), given the Mg II time lags and the measured line widths. Additionally, the virial factor f is required. The value of the virial factor for the H β emission line has been extensively investigated. It can be calibrated based on the relationships between SMBH masses and the properties (e.g., stellar velocity dispersion, luminosity, or stellar mass) of the bulges of host galaxies in inactive galaxies (e.g., Onken et al. 2004; Ho & Kim 2014; Woo et al. 2015; Yang et al. 2024). Alternatively, it can be determined through dynamical modeling of the BLR using reverberation mapping (RM) observations (e.g., Pancoast et al. 2011, 2014; Li et al. 2018; Villafañe et al. 2023), interferometric observations (e.g., GRAVITY Collaboration et al. 2018, 2020, 2021), or by joint analysis of RM and interferometry (e.g., Wang et al. 2020; Li et al. 2022, 2025).

However, there is no well-established virial factor for the Mg II line. Considering that the average virial factor corresponding to the FWHM of the H β line is close to 1 (e.g., Onken et al. 2004; Ho & Kim 2014; Woo et al. 2015; Yang et al. 2024), and acknowledging that the average line widths of Mg II and H β are similar for the same object (e.g., Wang et al. 2009; Ho et al. 2012; Bahk et al. 2019), we adopted $f = 1$

as the virial factor corresponding to the FWHM of the Mg II line. It is important to note that the virial factor f may vary from one object to another (e.g., Villafañe et al. 2023). A more accurate determination of the virial factor f and, consequently, a more precise measurement of M_\bullet are beyond the scope of this work. The uncertainties in the SMBH masses due to the variability of the virial factor are not considered here. We acknowledge the significant uncertainty (e.g., Grier et al. 2013; Woo et al. 2015; Fausnaugh et al. 2016) introduced by the virial factor f . The measured SMBH masses range from $8.1 < \log(M_\bullet/M_\odot) < 8.7$ and are listed in Table 4.

4. SIZE-LUMINOSITY RELATION AND DEPENDENCY ON ACCRETION RATE

4.1. $R_{\text{MgII}} - L_{3000}$ Relation

We present the $R_{\text{MgII}} - L_{3000}$ relation for our sample in conjunction with previous works in Figure 5. For the SDSS-RM project, we did not adopt the entire Mg II sample from Shen et al. (2024) due to their relatively larger measurement errors in time lags. Instead, we selected objects based on the same criteria used in the present study. Specifically, we only included objects from Shen et al. (2024) whose peak correlation coefficients from the ICCF are greater than 0.5 ($r_{\text{max}} > 0.5$). Even after applying this criterion, the error bars for the time lags of some remaining objects are still significantly larger than those of the SEAMBH sample in this paper. We further excluded objects with lag uncertainties greater than 1.5 times the mean lag uncertainties of the SEAMBH sample in logarithmic space (relative errors). We also verified that employing a slightly softer criterion does not alter the conclusions of subsequent analysis. More details can be found in Appendix D.

It is evident that our results significantly augment the sample at high luminosities. To parameterize the $R_{\text{MgII}} - L_{3000}$ relation, we adopt the following formalism:

$$\log \left(\frac{R_{\text{MgII}}}{\text{lt-days}} \right) = \alpha \log \left(\frac{L_{3000}}{10^{45} \text{ erg s}^{-1}} \right) + \beta, \quad (8)$$

where α and β represent the slope and intercept of the relation. We perform the linear regression using the LINMIX⁴ algorithm (Kelly 2007), which employs a hierarchical Bayesian approach to linear regression while accounting for measurement errors in both the X and Y axes. An intrinsic random scatter, σ_{int} , is also included in the model. Combining all available samples from the literature with our own, the best-fitting parameters are $\alpha = 0.24 \pm 0.03$, $\beta = 2.05 \pm 0.02$, and $\sigma_{\text{int}} = 0.04 \pm 0.01$.

The total scatter is defined by

$$\sigma_{R_{\text{MgII}}-L_{3000}} = \sqrt{\frac{1}{N_s} \sum_{i=1}^{N_s} \left(\log R_{\text{MgII}}^i - \log R_{R_{\text{MgII}}-L_{3000}}^i \right)^2}, \quad (9)$$

where N_s is the sample size, i is the index of the object, and $R_{R_{\text{MgII}}-L_{3000}}$ is the predicted radius from the best-fitting relation. Given the best parameters of the linear regression, the total scatter of the current sample is $\sigma_{R_{\text{MgII}}-L_{3000}} = 0.20$.

The slope of the $R_{\text{MgII}} - L_{3000}$ relation reported by the OzDES-RM project (Yu et al. 2023), which includes the "gold sample" from Homayouni et al. (2020), is 0.39 ± 0.08 . In contrast, the slope reported by the SDSS-RM project is 0.31 ± 0.06 (Shen et al. 2024). After incorporating our samples, the slope decreases slightly but remains consistent with the values reported by Yu et al. (2023) and Shen et al. (2024) within the uncertainties. Furthermore, the intercept of the $R_{\text{MgII}} - L_{3000}$ relation reported here is also consistent with the values found in these references.

4.2. Dependency on Accretion Rate

For AGNs exhibiting higher accretion rates, the observed $H\beta$ time lags are systematically shorter than those predicted by the standard $R_{H\beta} - L_{5100}$ relation (e.g., Du et al. 2015, 2016a, 2018a). While still preliminary, analogous behavior has been reported for Mg II emission lines in the context of the $R_{\text{MgII}} - L_{3000}$ relation by Martínez-Aldama et al. (2020) and Yu et al. (2021). The targets investigated in this study are candidate super-Eddington accretors, thereby constituting an ideal sample for probing this phenomenon.

As shown in Figure 5, our targets systematically lie below the best-fit $R_{\text{MgII}} - L_{3000}$ relation compared to other AGNs. To further illustrate this trend, Figure 6 displays a color-coded distribution of sources in the $R_{\text{MgII}} - L_{3000}$ plane, clearly indicating that AGNs with higher accretion rates deviate significantly below the canonical best-fit relation. To quantify this offset, we define the deviation parameter:

$$\Delta R_{\text{MgII}} = \log R_{\text{MgII}} - \log R_{R_{\text{MgII}}-L_{3000}}, \quad (10)$$

where $R_{R_{\text{MgII}}-L_{3000}}$ is the expected radius derived from the best-fit $R_{\text{MgII}} - L_{3000}$ relation. The errors of ΔR_{MgII} are merely from errors of time delays and any other errors are not considered. Figure 7 presents the correlation between ΔR_{MgII} and the dimensionless accretion rate \dot{M} , revealing a clear anti-correlation: higher accretion rates correspond to more negative ΔR_{MgII} values. The Pearson correlation coefficient (ρ) for the correlation is -0.51, with the corresponding two-sided p -value for a null hypothesis test of 2.8×10^{-7} . The Mg II time lags in SEAMBHs can be shortened by nearly an order of magnitude compared to those in AGNs with the lowest accretion rates. This behavior closely mirrors the shortened $H\beta$ lags reported in Du et al. (2015, 2016a, 2018a). Since the accretion rate depends on the lag measurement, larger values of \dot{M} may arise from shorter measured lags, thus leading to spurious relevance. To address this, we conduct a partial correlation analysis with respect to the lag, which yields a more robust anti-correlation. The results of the partial correlation analysis are presented in Appendix E.

4.3. Correlation with UV Iron Strength

⁴ <https://github.com/jmeyers314/linmix>

The relative strength of optical iron emission, quantified as $\mathcal{R}_{\text{Fe}}^{\text{opt}} = F_{\text{FeII}}^{\text{opt}}/F_{\text{H}\beta}$, has been established as a reliable indicator of accretion rate in AGNs (e.g., Boroson & Green 1992; Boroson 2002; Marziani et al. 2001; Shen & Ho 2014). Building upon this, Du & Wang (2019) developed an improved $R_{\text{H}\beta}$ – L_{5100} relation by incorporating $\mathcal{R}_{\text{Fe}}^{\text{opt}}$, which significantly reduces the scatter in time lag estimates.

To investigate whether a similar correlation exists for the UV iron emission, we define the UV iron strength parameter:

$$\mathcal{R}_{\text{Fe}}^{\text{UV}} = \frac{F_{\text{FeII}}^{\text{UV}}}{F_{\text{MgII}}}, \quad (11)$$

where F_{MgII} is the Mg II line flux, obtained by integrating the residual spectra from spectral fitting within 2700–2900 Å in the rest frame. $F_{\text{FeII}}^{\text{UV}}$ represents the integrated iron flux between 2250–2650 Å in the rest frame. For objects lacking spectral coverage in this wavelength range, we employed extrapolation using our iron template during the spectral fitting process.

For the measurement of $\mathcal{R}_{\text{Fe}}^{\text{UV}}$, we performed spectral fitting following the procedure described in Section 3.2, but extended the fitting window to cover 2260–3400 Å. This broader range helps mitigate degeneracy between the UV iron emission and the power-law continuum, leading to a more robust determination of the Fe II strength. For the Mg II light curves and lag measurements, however, we found that expanding the window has no significant effect. As demonstrated in Appendix F, the narrower window produces light curves with marginally lower scatter while yielding Mg II time lags fully consistent with those from the broader window. We therefore retained the narrower window for light-curve construction, but used the extended window exclusively for measuring $\mathcal{R}_{\text{Fe}}^{\text{UV}}$.

The final $\mathcal{R}_{\text{Fe}}^{\text{UV}}$ values represent the mean measurements across all available epochs, with uncertainties calculated as:

$$\sigma_{\mathcal{R}_{\text{Fe}}^{\text{UV}}} = \frac{S_{\mathcal{R}_{\text{Fe}}^{\text{UV}}}}{\sqrt{N}}, \quad (12)$$

where $S_{\mathcal{R}_{\text{Fe}}^{\text{UV}}}$ is the standard deviation and N is the number of epochs. Both the dimensionless accretion rates \mathcal{M} and UV iron strengths $\mathcal{R}_{\text{Fe}}^{\text{UV}}$ for our sample are presented in Table 4.

Given that different studies have adopted distinct iron templates and spectral fitting windows to measure $\mathcal{R}_{\text{Fe}}^{\text{UV}}$ (e.g., Yu et al. 2023; Shen et al. 2024), a direct combination of their values could introduce systematic biases. To ensure consistency, we collected the mean spectra from the RM campaigns presented in Yu et al. (2023) and Shen et al. (2024), and re-measured their $\mathcal{R}_{\text{Fe}}^{\text{UV}}$ values using the same iron template and fitting window as applied to our own sample. Similarly, we present the $R_{\text{MgII}} - L_{3000}$ relation color-coded by $\mathcal{R}_{\text{Fe}}^{\text{UV}}$, along with the correlation between ΔR_{MgII} and $\mathcal{R}_{\text{Fe}}^{\text{UV}}$ in Figures 6 and 7, respectively. Additionally, we present the correlation between $\mathcal{R}_{\text{Fe}}^{\text{UV}}$ and \mathcal{M} in Figure 8. The Pearson correlation coefficient for $\Delta R_{\text{MgII}} - \mathcal{R}_{\text{Fe}}^{\text{UV}}$ correlation is 0.06, with the corresponding two-sided p -value for a null hypothesis test of

0.59. The anticorrelation between ΔR_{MgII} and $\mathcal{R}_{\text{Fe}}^{\text{UV}}$ is not as significant as the anticorrelation between ΔR_{MgII} and \mathcal{M} , which is consistent with the findings of Yu et al. (2023). A potential explanation is that the correlation between the accretion rate (or Eddington ratio) and $\mathcal{R}_{\text{Fe}}^{\text{UV}}$ is relatively weaker than the correlation between the accretion rate (or Eddington ratio) and $\mathcal{R}_{\text{Fe}}^{\text{opt}}$ (e.g., Martínez-Aldama et al. 2020; Khadka et al. 2022; Pan et al. 2025). This is further supported by the substantial scatter in the correlation between $\mathcal{R}_{\text{Fe}}^{\text{opt}}$ and $\mathcal{R}_{\text{Fe}}^{\text{UV}}$, as well as their equivalent widths (e.g., Kovačević-Dojčinović & Popović 2015; Pan et al. 2025). Additionally, the current Mg II RM sample remains relatively small and likely incomplete; expanding this sample in future campaigns will be essential to clarify these trends. A larger sample with better quality may enable a more thorough investigation of the $\Delta R_{\text{MgII}} - \mathcal{R}_{\text{Fe}}^{\text{UV}}$ correlation.

5. DISCUSSIONS

5.1. Mg II Lag vs. H β Lag

Given the lower ionization potential of Mg⁺ (7.6 eV), it is expected that the time lags of Mg II lines should be longer than those of H β lines in AGNs with the same luminosities. Here, we present a comparison between the Mg II and H β lags in Figure 9. The L_{3000} values for the Mg II sample were converted to L_{5100} using the flux ratio at these two wavelengths from the quasar mean spectrum provided in Richards et al. (2006).

For the H β lags, we utilized the compilation from Du & Wang (2019) (the collection was updated by Chen et al. 2023 based on more recent observations), which includes samples from Peterson et al. (1998), Kaspi et al. (2000), Du et al. (2014), Bentz et al. (2009), and others, as well as data from some Palomar-Green quasars presented in Hu et al. (2021) and low-redshift galaxies from U et al. (2022). Additionally, we augmented this collection with more recent results from Woo et al. (2024)⁵ and Hu et al. (2025). The $R_{\text{H}\beta} - L_{5100}$ relation from Bentz et al. (2013) and the relation for SEAMBHs from Du et al. (2018a) are also shown in Figure 9. It is evident that the Mg II lags are indeed longer than the H β lags. Assuming that the Mg II and H β emitters at the same luminosities have the same SMBH masses, the line widths of Mg II should be narrower than those of H β , which is consistent with observational studies regarding line widths (e.g., Hu et al. 2008; Wang et al. 2009; Shen & Liu 2012; Marziani et al. 2013; Mejía-Restrepo et al. 2016).

Furthermore, it is noteworthy that, although the luminosity coverage of the present Mg II sample is still limited, the slope of the $R_{\text{MgII}} - L_{5100}$ relation is shallower than that of the $R_{\text{H}\beta} - L_{5100}$ relation. This trend may be associated with the fact that the Mg II line widths are more consistent with those of H β when the line widths are narrower (e.g., Wang et al. 2009; Marziani et al. 2013). Larger samples of high-

⁵ Seven objects with unreliable measurements are excluded; see further details in Woo et al. (2024).

quality Mg II measurements across a wide luminosity range and more detailed BLR dynamical modeling are needed for further investigation of this point in the future.

5.2. Physical Mechanism for Shortened Lags

It has been demonstrated that AGNs with high accretion rates exhibit shorter Mg II time lags compared to AGNs with normal accretion rates (see Figure 7). One possible explanation for this phenomenon is the self-shadowing effects of slim accretion disks in SEAMBHs (Wang et al. 2014). The inner region of the accretion disk is puffed up, thus the ionizing radiation emitted from the innermost region is shielded and cannot reach the gas in the BLRs. This results in a reduced radius of the BLRs that respond to the varying continuum. Furthermore, due to the lower ionization potential of Mg^+ , the radius of the accretion disk emitting photons that ionize Mg II is larger than that for $\text{H}\beta$. Consequently, the degree of self-shadowing for Mg II lines may be slightly weaker than for $\text{H}\beta$ lines. However, as shown in Figure 7, the shortening of Mg II time lags remains significant. More detailed calculations comparing the self-shadowing effects in Mg II and $\text{H}\beta$, as well as comparisons with observational data, are needed in future studies.

6. SUMMARY

In this 15th paper of the SEAMBH series, we present the results of a 7-year reverberation mapping (RM) campaign that monitored the Mg II emission lines in eighteen high-luminosity SEAMBHs, conducted from 2017 to 2024 using the Lijiang 2.4 m and CAHA 2.2 m telescopes. The key findings of this study can be summarized as follows:

1. We successfully measured the Mg II time lags for eight of the eighteen objects. By incorporating the measurements of their line widths, we were able to determine the masses of their central SMBHs. The Mg II time lags typically range from 100 to 300 days in the observed frames, while the SMBH masses span a range of $8.1 < \log(M_\bullet/M_\odot) < 8.7$.
2. By combining our objects with previous Mg II RM samples, we updated the $R_{\text{MgII}} - L_{3000}$ relation. The slope and intercept of the $R_{\text{MgII}} - L_{3000}$ relation obtained here are $\alpha = 0.24 \pm 0.03$ and $\beta = 2.05 \pm 0.02$, respectively, which are consistent with those reported in the existing literature.
3. We found that SEAMBHs exhibit shortened Mg II time lags compared to AGNs with normal accretion rates. This phenomenon closely mirrors the shortened $\text{H}\beta$ lags reported in SEAMBHs. Furthermore, we examined the relationship between the deviation in the $R_{\text{MgII}} - L_{3000}$ relation and the accretion rate, as well as the relative strength of UV iron emissions. The deviation shows a clear correlation with the accretion rate

but no significant correlation with the strength of UV iron emissions.

In the future, larger samples of high-quality Mg II RM data will not only facilitate a more precise refinement of the $R_{\text{MgII}} - L_{3000}$ relation but also deepen our understanding of the accretion physics in SMBHs. This will ultimately allow us to establish more reliable SMBH mass indicators for AGNs at high redshifts and enhance our comprehension of the formation and evolution of SMBHs in the early universe.

ACKNOWLEDGEMENTS

We thank Zhefu Yu for kindly sharing the mean spectra of OzDES RM objects and the anonymous referee for useful comments. We acknowledge the support of the staff at the Lijiang 2.4 m telescope. Funding for the telescope has been provided by the Chinese Academy of Sciences (CAS) and the People's Government of Yunnan Province. This work is also based on observations collected at the Centro Astronómico Hispano en Andalucía (CAHA) at Calar Alto, which is operated jointly by the Andalusian Universities and the Instituto de Astrofísica de Andalucía (CSIC). This research is supported by the National Key R&D Program of China (2021YFA1600404 and 2023YFA1607903), the National Science Foundation of China through grants NSFC-12521005, -12333003, -12122305, -12022301, -11991050, and -11833008, as well as the National Science and Technology Major Project (2024ZD0300303). Additionally, it is funded by the China Manned Space Project (CMS-CSST-2025-A07 and CMS-CSST-2021-A06). L.C.H. was supported by the National Science Foundation of China (12233001) and the China Manned Space Program (CMS-CSST-2025-A09).

This work used archival data obtained with the Samuel Oschin Telescope 48-inch and the 60-inch Telescope at the Palomar Observatory as part of the Zwicky Transient Facility project. ZTF is supported by the National Science Foundation under Grants No.AST-1440341 and AST-2034437 and a collaboration including current partners Caltech, IPAC, the Weizmann Institute for Science, the Oskar Klein Center at Stockholm University, the University of Maryland, Deutsches Elektronen-Synchrotron and Humboldt University, the TANGO Consortium of Taiwan, the University of Wisconsin at Milwaukee, Trinity College Dublin, Lawrence Livermore National Laboratories, IN2P3, University of Warwick, Ruhr University Bochum, Northwestern University and former partners the University of Washington, Los Alamos National Laboratories, and Lawrence Berkeley National Laboratories. Operations are conducted by COO, IPAC, and UW.

Software: LINMIX (Kelly 2007), PYCALI (Li et al. 2014; Li 2024a), MICA (Li et al. 2016; Li 2024b), DASPEC (Du 2024)

APPENDIX

A. PHOTOMETRIC LIGHT CURVES OF COMPARISON STARS

For the comparison stars, their photometric light curves are presented in Figure 10. The magnitudes are shown after subtracting their mean values (differential magnitudes). During the monitoring period, the variations of comparison stars were consistently low.

B. THE CHOICE OF IRON TEMPLATE

Discrepancies in Mg II and Fe II flux measurements arising from different iron templates have been reported in the literature (e.g., Woo et al. 2018; Shin et al. 2019). In our analysis, the iron template used in the main text is the composite template compiled by Shen et al. (2019), which incorporates the Salvander et al. (2007) template across the Mg II wavelength region (see Section 3.2). To examine whether our light curves and lag measurements are sensitive to the choice of iron template, we performed a test by replacing the Salvander et al. (2007) segment with the Tsuzuki et al. (2006) template. The latter is based on synthetic spectra from photoionization calculations and has been recommended as an improved template (e.g., Wang et al. 2009). We re-derived the continuum and Mg II light curves and remeasured the time lags using the ICCF method (Section 3.5) for the eight objects with previously reliable lag measurements. The resulting light curves are shown in Figure 11, and a comparison of the Mg II lags obtained with the Salvander et al. (2007) and Tsuzuki et al. (2006) templates is presented in Figure 12. We find that the time lags derived from the two templates are consistent within the uncertainties, in agreement with a similar test presented by Yu et al. (2021).

Regarding $\mathcal{R}_{\text{Fe}}^{\text{UV}}$, we also tested the results using template from Tsuzuki et al. (2006). In this case, the relation between $\mathcal{R}_{\text{Fe}}^{\text{UV}}$ and the deviation parameter ΔR_{MgII} is shown in Figure 13. The correlation remains statistically ambiguous.

C. LIGHT CURVES OF OBJECTS WITH UNSUCCESSFUL LAG MEASUREMENTS

We present the light curves of ten targets for which reliable lag measurements could not be obtained in Figure 14. During our time-series analysis, the peak values of the cross-correlation functions (r_{max}) for these light curves did not exceed 0.5.

D. REFINE SAMPLES BASED ON LAG MEASUREMENT ERRORS

The error of the time lag in logarithmic space is defined as

$$\sigma_{\log \tau} = \frac{1}{\ln 10} \cdot \frac{\sigma_{\tau}}{\tau}, \quad (\text{D1})$$

where σ_{τ} is the measurement error of the time lag in linear space. We calculate the mean error of lag in logarithmic space for SEAMBH sample in this paper as $\sigma_{\text{critical}} = 0.068$. For all available samples from the literature (where the sample from Shen et al. 2024 is limited to objects with $r_{\text{max}} > 0.5$), objects with errors in logarithmic space larger

than $1.5\sigma_{\text{critical}}$ are discarded. We have verified that the results of the present paper do not change significantly if we instead discard objects whose errors exceed $2\sigma_{\text{critical}}$.

E. PARTIAL CORRELATION ANALYSIS FOR DEPENDENCE ON ACCRETION RATE

An artificial anti-correlation between ΔR_{MgII} and $\dot{\mathcal{M}}$ may arise because $\dot{\mathcal{M}}$ is anti-correlated with the time lag, while ΔR_{MgII} is positively correlated with the time lag. To investigate whether the observed anti-correlation between ΔR_{MgII} and $\dot{\mathcal{M}}$ is due to this effect, we conducted a partial correlation analysis. The results of the partial correlation analysis are shown in Table 5. The correlation coefficient between ΔR_{MgII} and $\dot{\mathcal{M}}$ is -0.51, while the partial correlation coefficient with respect to the time lag τ_{MgII} is -0.85, indicating a more significant anti-correlation.

Furthermore, $\dot{\mathcal{M}}$ is also positively correlated with luminosity. We conducted another partial correlation analysis between ΔR_{MgII} and $\dot{\mathcal{M}}$ while controlling for L_{3000} . The anti-correlation remains substantial, as the partial correlation coefficient is -0.70.

F. THE FITTING WINDOW FOR MG II LIGHT CURVE MEASUREMENT

In measuring $\mathcal{R}_{\text{Fe}}^{\text{UV}}$, we employed a broader fitting window of 2260–3400 Å. For the Mg II flux measurements used in constructing light curves, however, we adopted a narrower range of 2260–3050 Å. To assess the sensitivity of our results to this choice, we compared the Mg II light curves and time lags derived using the two windows: the narrower Window 1 (2260–3050 Å) and the broader Window 2 (2260–3400 Å). As shown in Figures 15 and 16 for the eight targets with reliable lag measurements, the resulting light curves and ICCF-derived time lags are generally consistent within uncertainties. We note that the narrower window yields several light curves with marginally reduced scatter (see, e.g., J093857). Therefore, we adopted the results from the narrower fitting window as our final measurements in the main text.

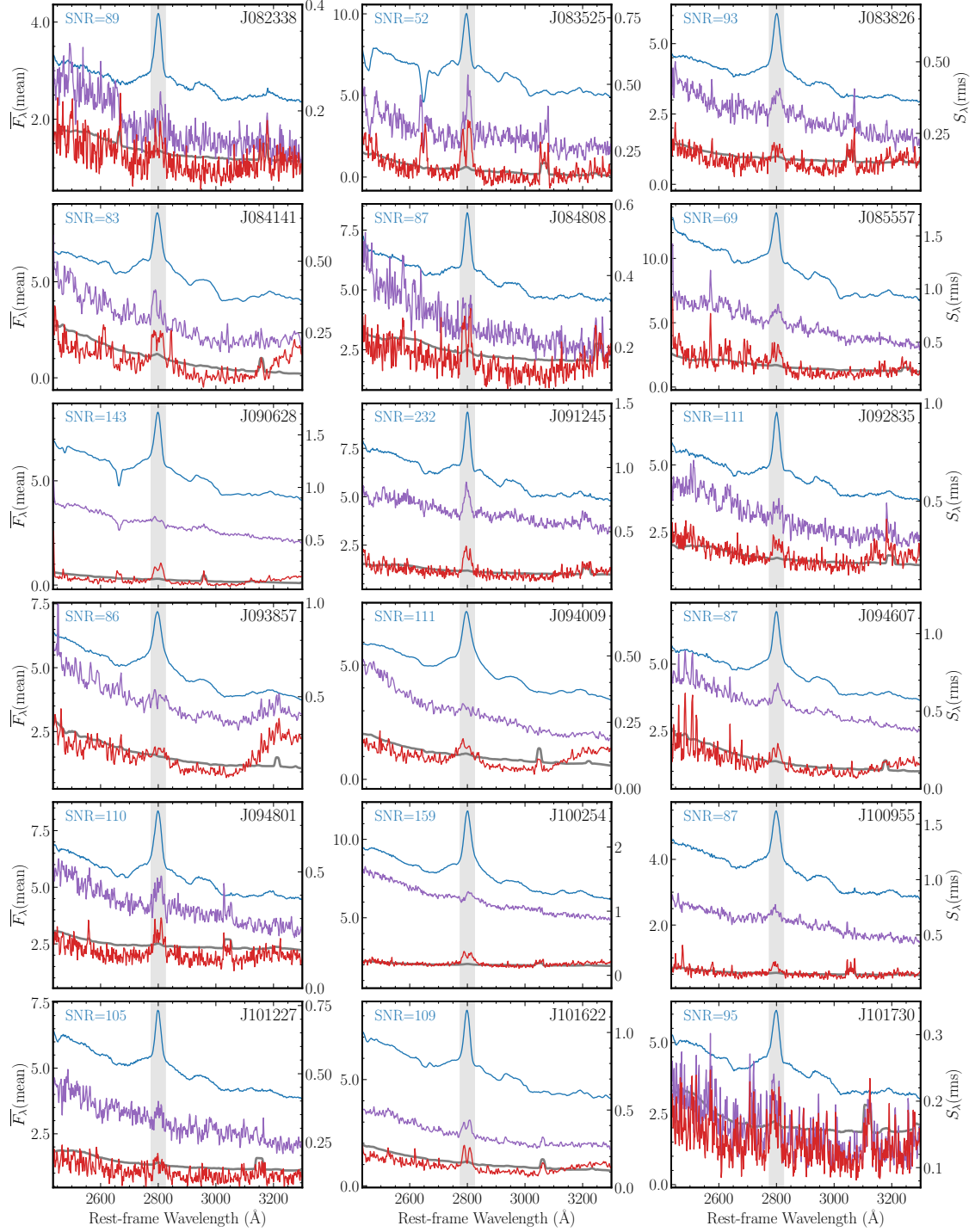


Figure 1. Mean and rms spectra. The blue, purple, and red spectra in each panel represent the mean spectra, rms spectra, and rms spectra generated from the residuals after subtracting the power law and iron template (see more details in Section 3.2), respectively. The spectra are plotted with rest-frame wavelength versus Galactic-extinction-corrected flux in the observed frame, consistent with the subsequent figures. The gray lines represent the error spectra for comparison. The gray shadow marks the 2775–2825 Å integration window for measurements of Mg II light curves. The tick labels on the left and right y axes correspond to the mean and rms spectra, respectively. All spectra are in units of $10^{-16} \text{ erg s}^{-1} \text{ cm}^{-2} \text{ Å}^{-1}$. The signal-to-noise ratio (SNR) at 3000 Å of the mean spectrum is listed at each panel.

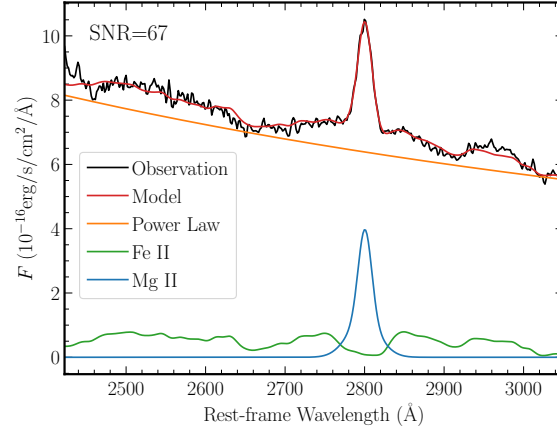


Figure 2. An example of the spectral fitting results. The black line represents a single epoch spectrum of J091245 in the rest frame after correcting for Galactic extinction. The signal-to-noise ratio (SNR) of this spectrum is explicitly written. The red line indicates the best-fit model. The orange, green, and blue lines correspond to the power law, iron template, and Mg II components, respectively (see Section 3.2).

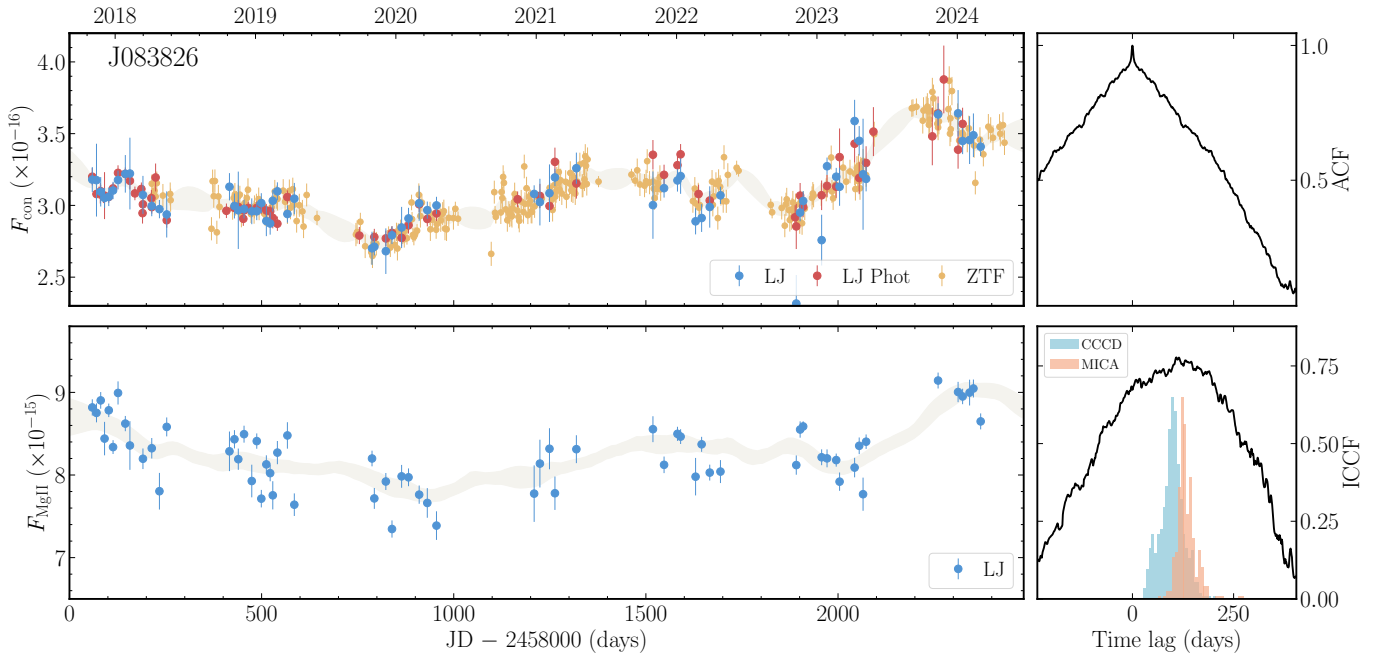


Figure 3. Light curves and time-lag measurements. The left panels show the 3000 Å continuum light curves after intercalibration alongside the Mg II light curves. “LJ/CAHA”, “LJ/CAHA Phot”, and “ZTF” represent the Lijiang/CAHA spectroscopic data, Lijiang/CAHA photometric data, and ZTF photometric data points, respectively. The continuum light curves are in units of $10^{-16} \text{ erg s}^{-1} \text{ cm}^{-2} \text{ Å}^{-1}$, while the Mg II light curves are in units of $10^{-15} \text{ erg s}^{-1} \text{ cm}^{-2}$. The gray shaded regions represent the reconstructions from the MICA model, incorporating additional systematic errors that were automatically included during the reconstruction process. The upper-right panel displays the auto-correlation function (ACF) of the continuum light curve. The lower-right panel shows the ICCF (black line), CCCD (blue histogram), and time-lag distribution obtained from MICA (orange histogram) in the observed frame. The complete figure set (8 images) is available in the online article.

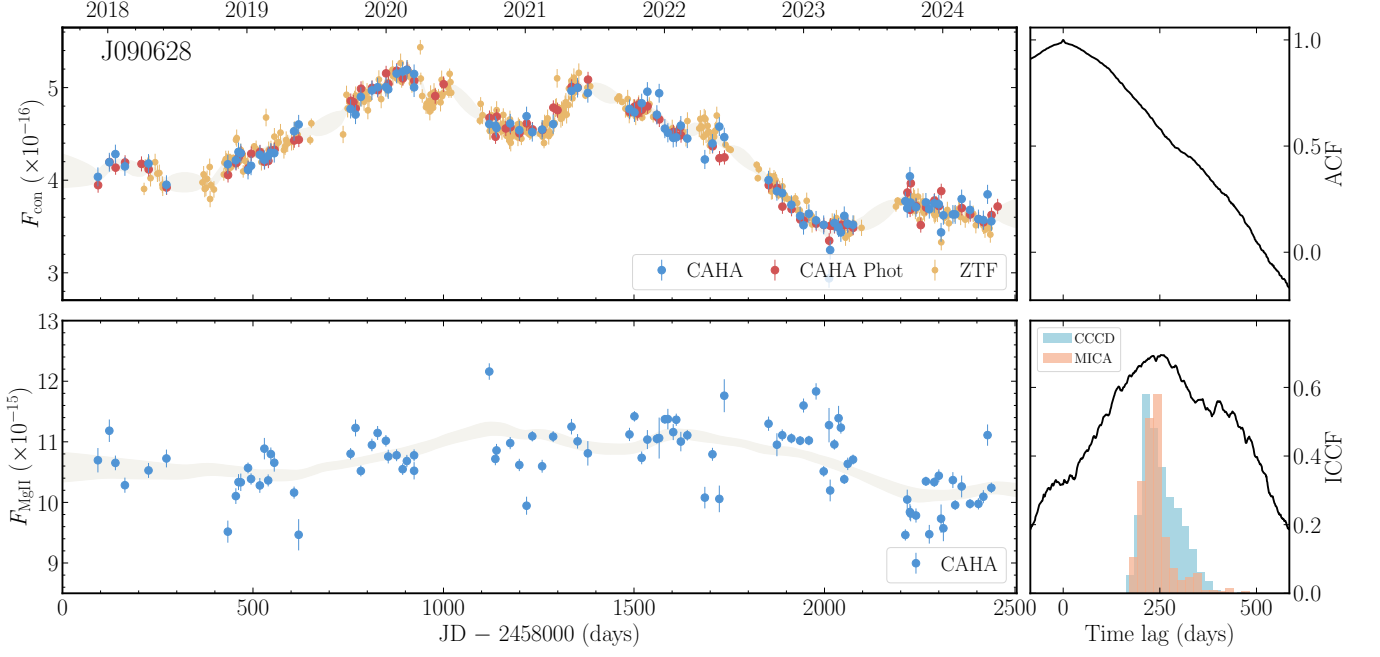


Figure 3. (Continued.)

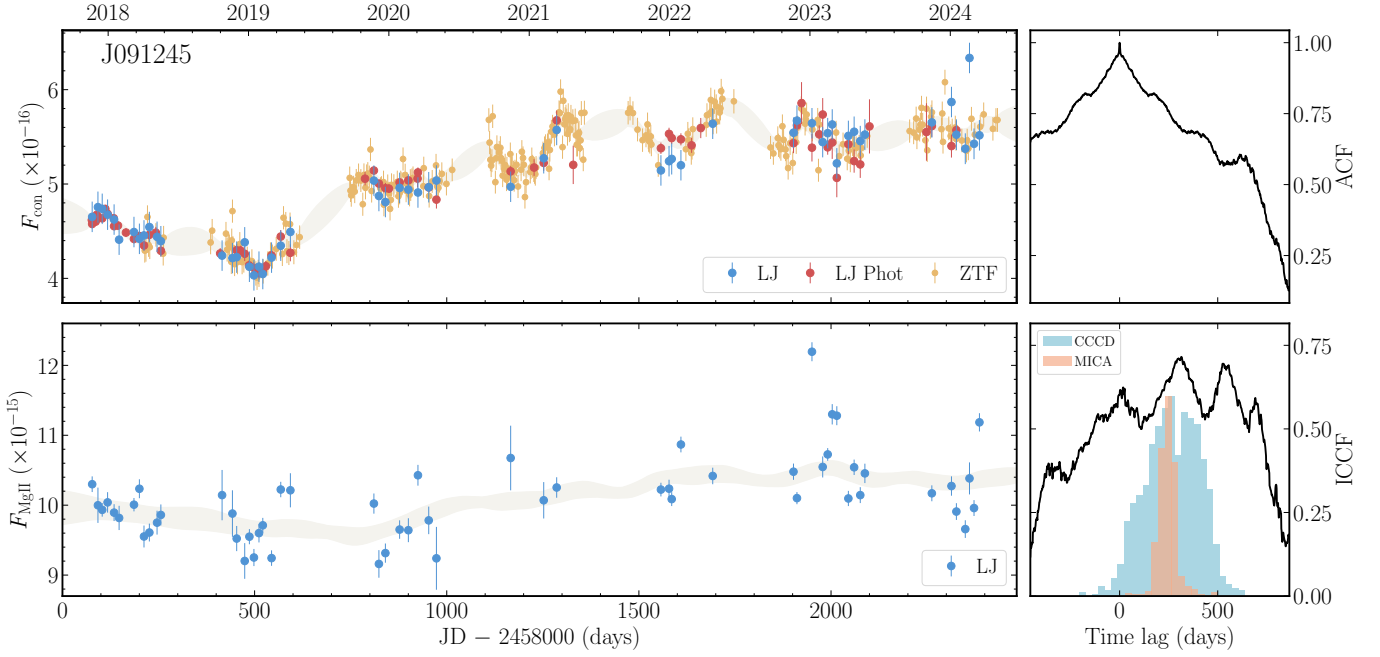


Figure 3. (Continued.)

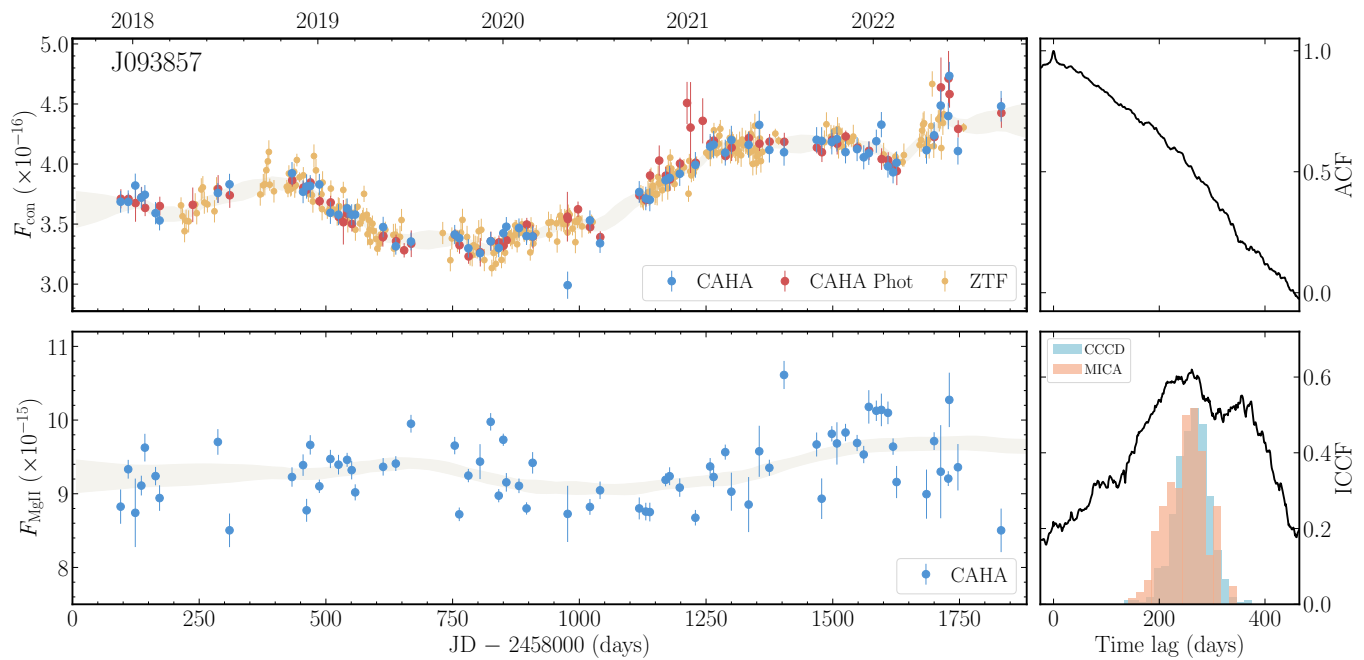


Figure 3. (Continued.)

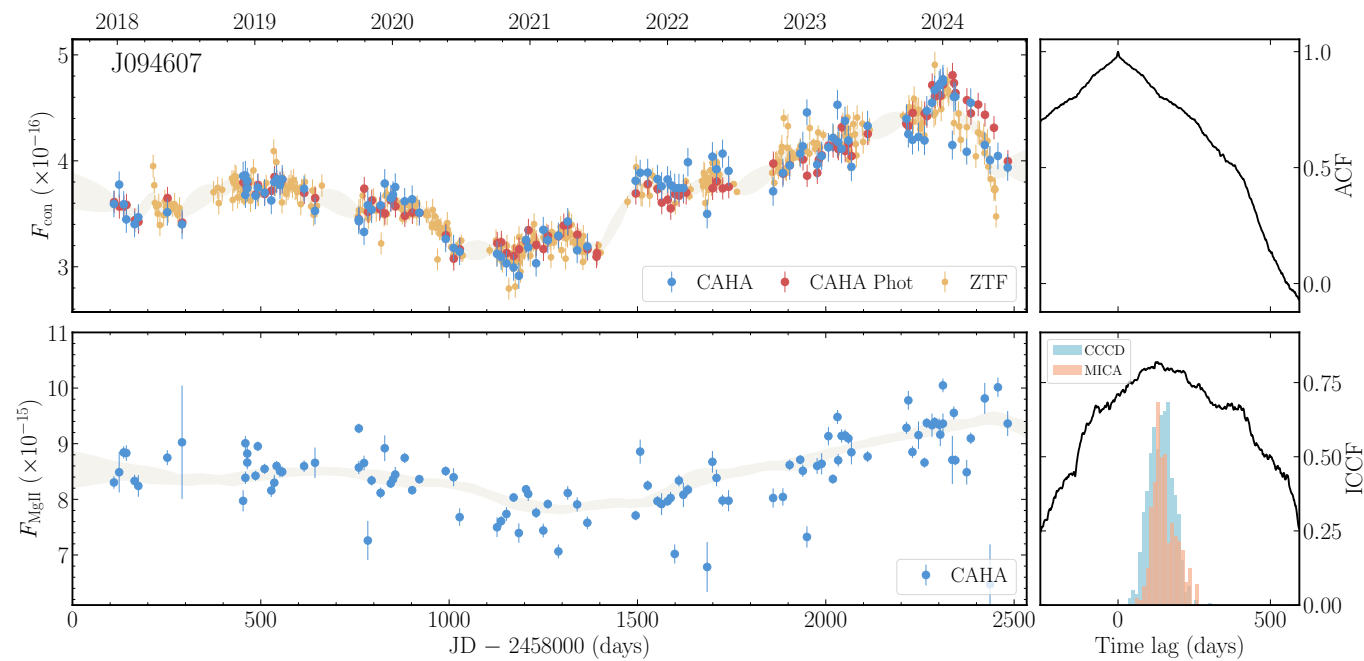


Figure 3. (Continued.)

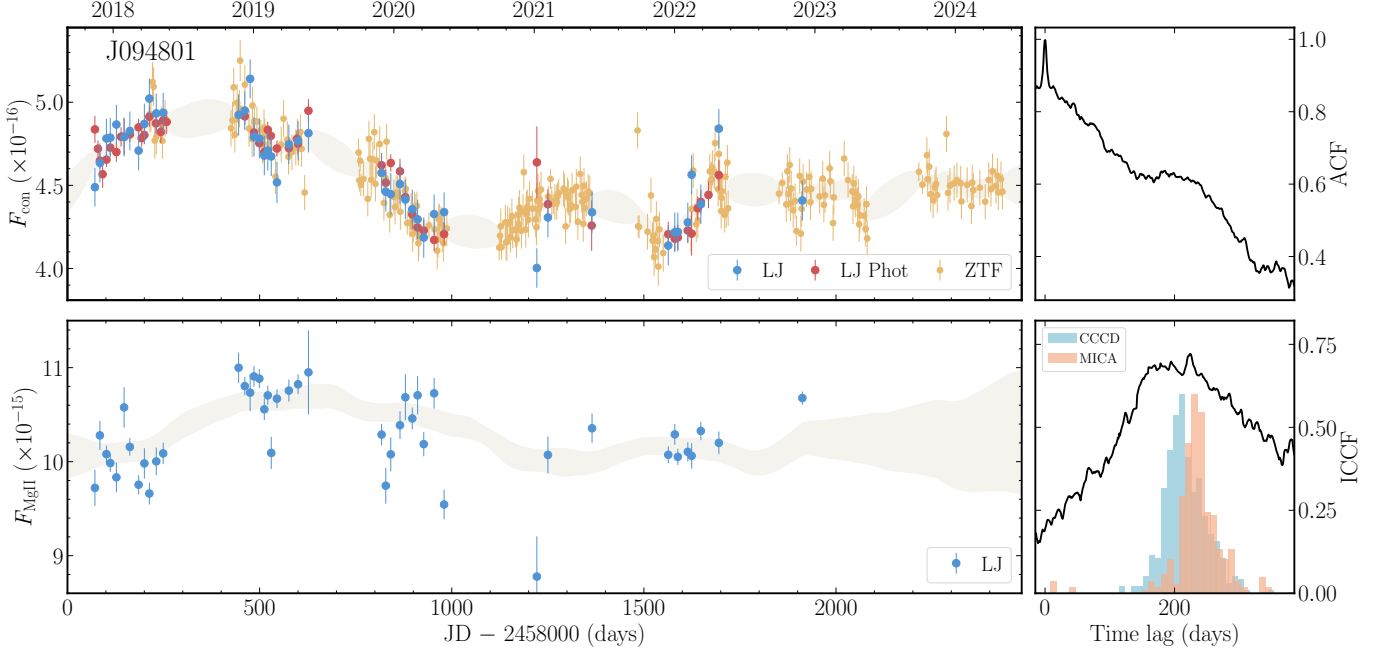


Figure 3. (Continued.)

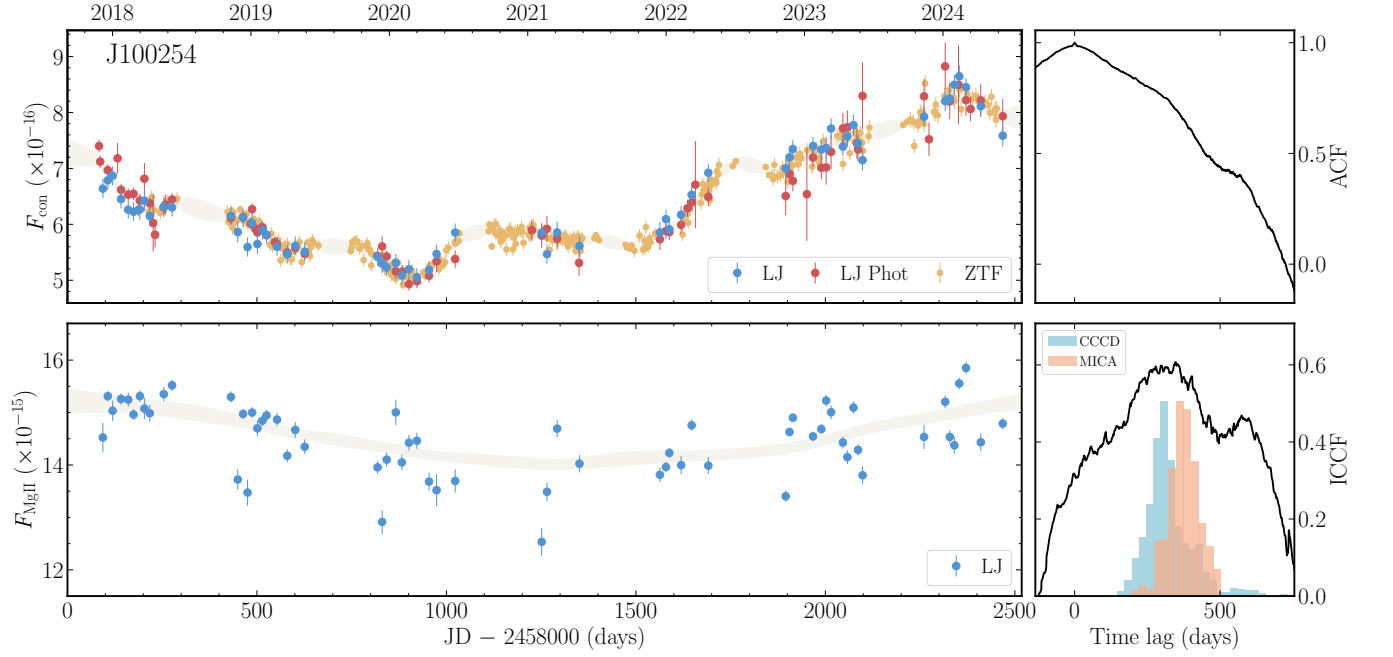


Figure 3. (Continued.)

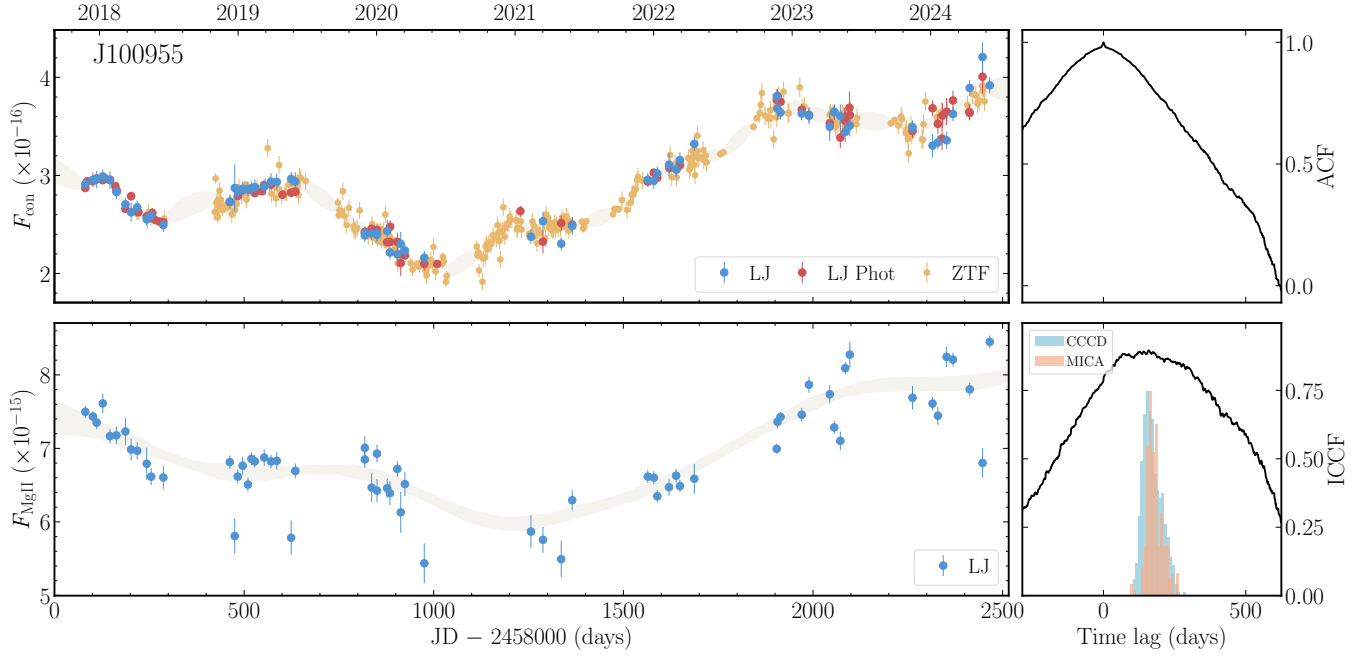
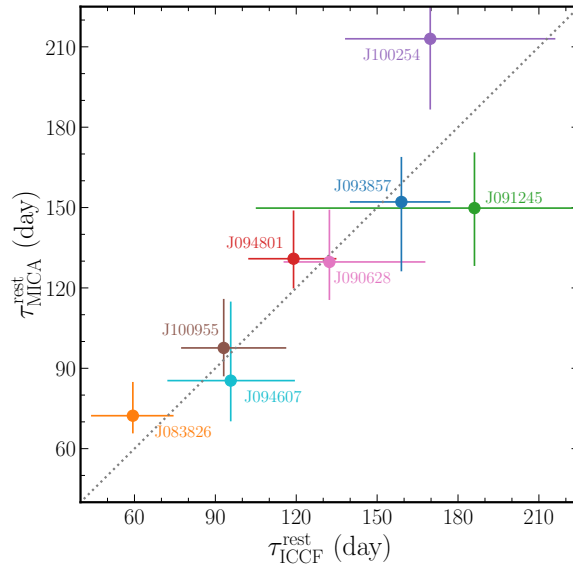


Figure 3. (Continued.)

Figure 4. Comparison between $\tau_{\text{ICCF}}^{\text{rest}}$ and $\tau_{\text{MICA}}^{\text{rest}}$.

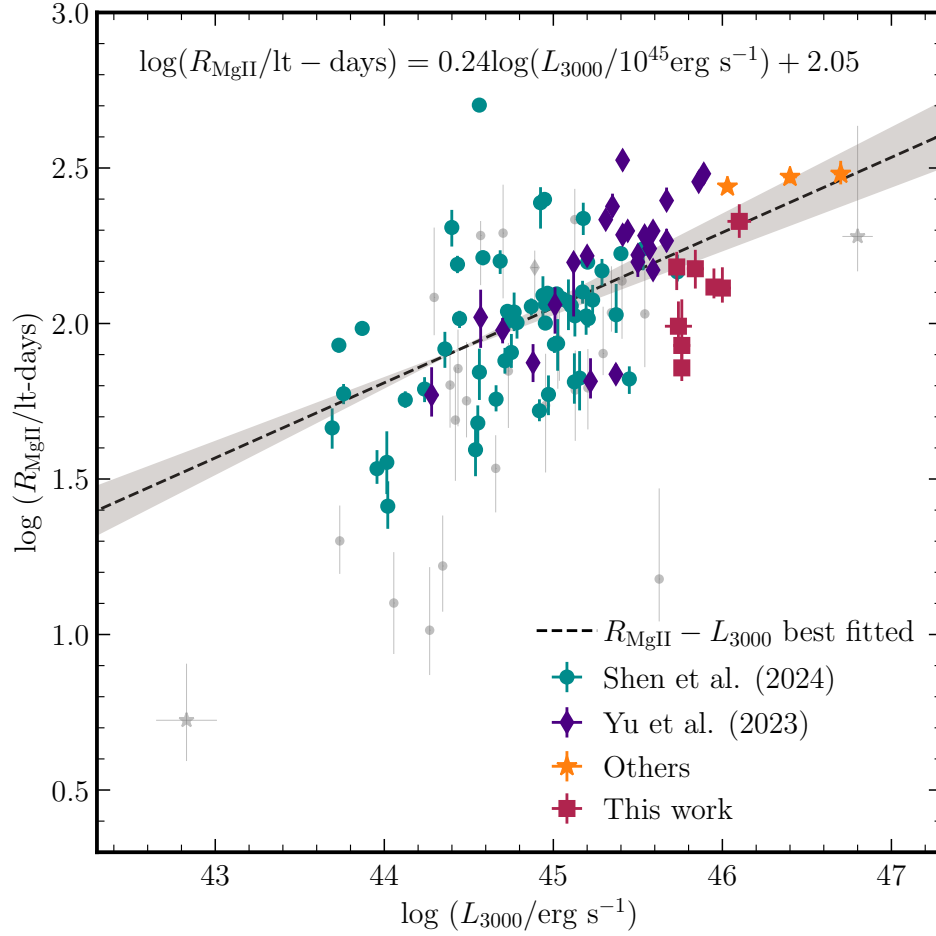


Figure 5. $R_{\text{MgII}} - L_{3000}$ relation. The red squares represent the measurements from this paper. The green circles and purple diamonds correspond to the SDSS sample from Shen et al. (2024) and the OzDES sample from Yu et al. (2023), respectively. The orange stars indicate additional measurements collected from Metzroth et al. (2006), Lira et al. (2018), Zajaček et al. (2020), Zajaček et al. (2021), and Prince et al. (2022). Colors of objects rejected for their large measurement errors are replaced with gray (see Section 4.1). The black dashed line represents the best-fitting $R_{\text{MgII}} - L_{3000}$ relation, while the gray shaded region indicates the 1σ confidence band derived from the LINMIX algorithm.

REFERENCES

- Bahk, H., Woo, J.-H., & Park, D. 2019, *ApJ*, 875, 50.
doi:10.3847/1538-4357/ab100d
- Barth, A. J., Pancoast, A., Bennert, V. N., et al. 2013, *ApJ*, 769, 128. doi:10.1088/0004-637X/769/2/128
- Barth, A. J., Bennert, V. N., Canalizo, G., et al. 2015, *ApJS*, 217, 26. doi:10.1088/0067-0049/217/2/26
- Bentz, M. C., Walsh, J. L., Barth, A. J., et al. 2009, *ApJ*, 705, 199. doi:10.1088/0004-637X/705/1/199
- Bentz, M. C., Horne, K., Barth, A. J., et al. 2010, *ApJL*, 720, L46. doi:10.1088/2041-8205/720/1/L46
- Bentz, M. C., Denney, K. D., Grier, C. J., et al. 2013, *ApJ*, 767, 149. doi:10.1088/0004-637X/767/2/149

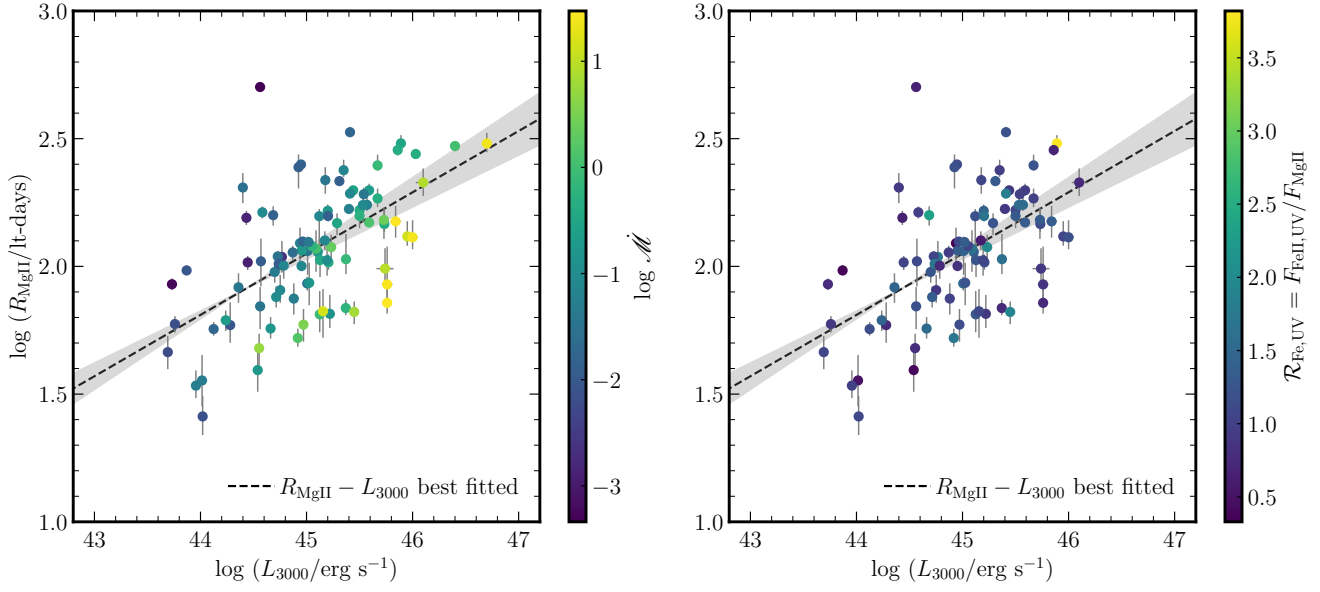


Figure 6. $R_{\text{MgII}} - L_{3000}$ relation color-coded by both the dimensionless accretion rate $\dot{\mathcal{M}}$ (left panel) and the UV iron strength $\mathcal{R}_{\text{Fe,UV}}$ (right panel). The dashed line and shaded region have the same meaning as in Figure 5, representing the best-fit relation and its 1σ uncertainty, respectively. Three targets not from the SDSS and OzDES samples are absent for the $\mathcal{R}_{\text{Fe,UV}}$ measurement, as we do not obtain their corresponding spectra for a unified analysis, consistent with the presentation in subsequent figures.

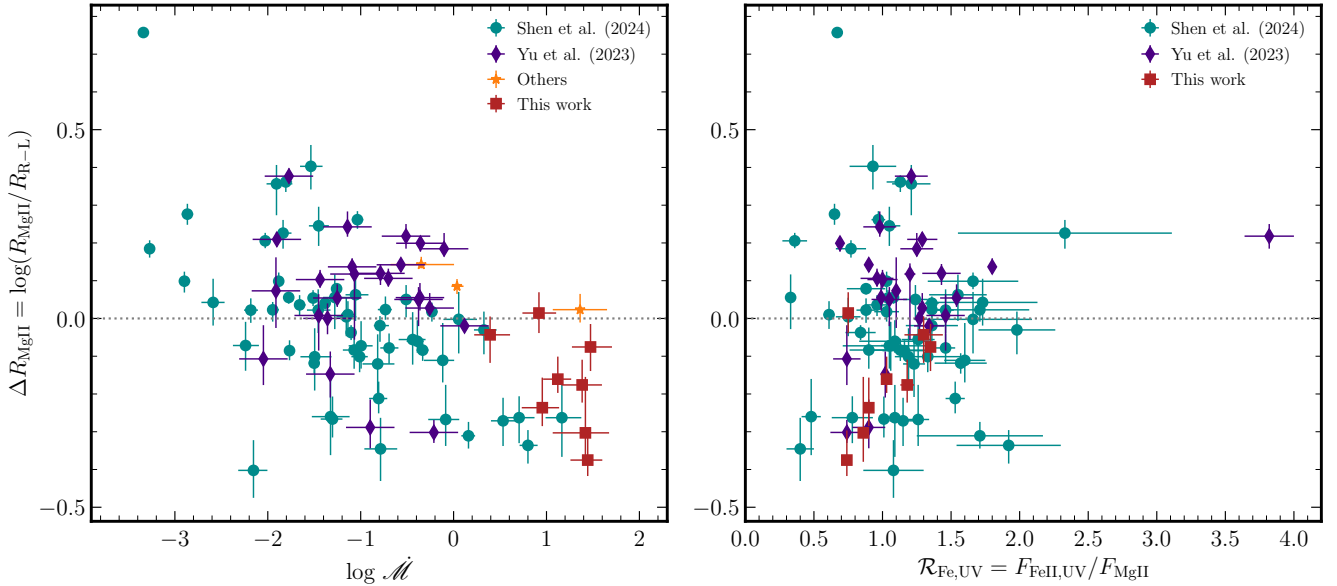


Figure 7. Correlations of ΔR_{MgII} with the dimensionless accretion rate $\dot{\mathcal{M}}$ (left panel) and the UV iron strength $\mathcal{R}_{\text{Fe,UV}}$ (right panel). ΔR_{MgII} represents the residual Mg II lags relative to the $R_{\text{MgII}} - L_{3000}$ relation. The black dotted line indicates the locus where the observed Mg II lags exactly match the predictions from the $R_{\text{MgII}} - L_{3000}$ relation.

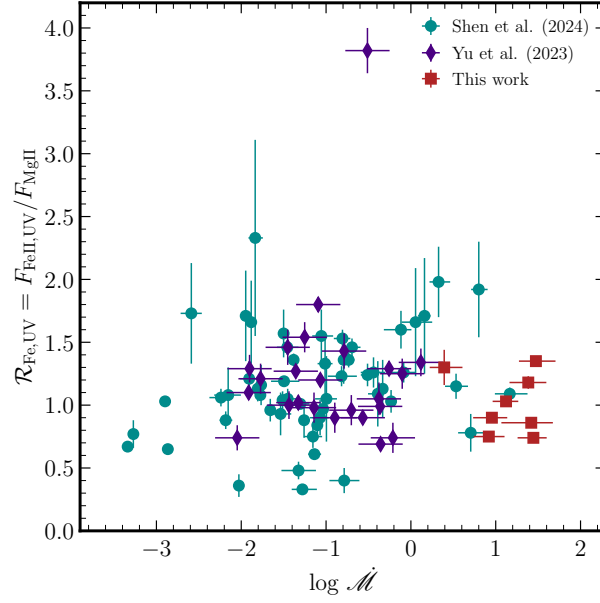


Figure 8. Correlation of the UV iron strength $\mathcal{R}_{\text{Fe,UV}}$ with the dimensionless accretion rate $\dot{\mathcal{M}}$.

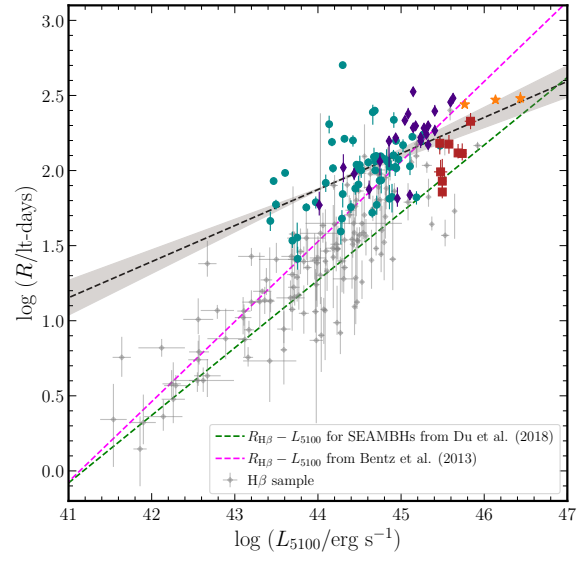


Figure 9. Comparison between Mg II and $H\beta$ time lags. Symbols follow the same color-coding as in Figure 5, with gray diamonds representing $H\beta$ lags. The black dashed line and gray shaded region show the best-fit $R_{\text{MgII}} - L_{5100}$ relation and its uncertainties in Figure 5. The magenta dashed line shows the $R_{H\beta} - L_{5100}$ relation from Bentz et al. (2013), while the green dashed line shows the $R_{H\beta} - L_{5100}$ relation for SEAMBHs from Du et al. (2018a).

Table 1. Objects and Observations

Name	Redshift	Observatory	Filter	Monitoring Period	N_{spec}	T_{median}	Duration	Comparison Star	
				(yyyy/mm-yyyy/mm)		(day)	(day)	α_{2000}	δ_{2000}
(1)	(2)	(3)	(4)	(5)	(6)	(7)	(8)	(9)	(10)
SDSS J082338.49+592648.4	0.76	Lijiang	SDSS r'	2017/10 – 2021/12	42	17	1508	08 23 41.75	+59 27 03.60
SDSS J083525.39+513829.7	0.82	Lijiang	SDSS r'	2017/10 – 2024/04	67	21	2361	08 35 38.72	+51 35 34.42
SDSS J083826.25+253010.8	0.82	Lijiang	SDSS r'	2017/11 – 2024/03	65	18	2312	08 38 19.94	+25 31 48.93
SDSS J084141.66+405237.6	0.77	CAHA	V	2018/01 – 2022/09	56	20	1749	08 41 38.37	+40 53 28.51
SDSS J084808.36+083208.1	0.71	Lijiang	SDSS r'	2017/11 – 2021/12	36	21	1494	08 48 16.06	+08 33 03.16
SDSS J085557.11+561534.7	0.72	Lijiang	SDSS r'	2017/11 – 2022/12	62	14	1853	08 56 15.66	+56 15 26.17
SDSS J090628.04+434225.0	0.89	CAHA	V	2017/12 – 2024/05	95	15	2345	09 06 29.88	+43 43 05.13
SDSS J091245.42+213139.1	0.74	Lijiang	SDSS r'	2017/11 – 2024/04	57	18	2309	09 12 55.78	+21 32 44.73
SDSS J092835.01+623633.1	0.75	Lijiang	SDSS r'	2017/11 – 2024/04	73	17	2346	09 27 49.04	+62 38 08.61
SDSS J093857.97+614019.6	0.74	CAHA	V	2017/12 – 2022/09	71	17	1737	09 39 15.42	+61 40 11.37
SDSS J094009.76+455250.8	0.83	CAHA	V	2017/12 – 2024/06	103	15	2373	09 40 05.51	+45 55 26.10
SDSS J094607.30+495412.8	0.76	CAHA	V	2017/12 – 2024/06	107	14	2373	09 46 17.48	+49 51 41.58
SDSS J094801.95+032118.9	0.83	Lijiang	SDSS r'	2017/11 – 2022/11	45	17	1841	09 48 01.61	+03 22 51.07
SDSS J100254.51+324039.0	0.83	Lijiang	SDSS r'	2017/12 – 2024/06	63	18	2375	10 02 50.99	+32 37 59.37
SDSS J100955.45+302734.3	0.82	Lijiang	SDSS r'	2017/11 – 2024/06	64	18	2385	10 09 49.87	+30 27 55.30
SDSS J101227.21+345515.4	0.77	Lijiang	SDSS r'	2017/12 – 2022/11	42	18	1820	10 12 46.38	+34 54 05.28
SDSS J101622.60+470643.3	0.82	CAHA	V	2017/12 – 2024/07	98	19	2408	10 16 38.36	+47 07 56.24
SDSS J101730.21+474000.0	0.79	Lijiang	SDSS r'	2017/11 – 2021/12	39	14	1467	10 17 16.76	+47 41 48.55

NOTE—Columns (1)–(3) provide the name, redshift, and observatory for each object. Column (4) presents the filter used for the photometric observations. Column (5) lists the start and end dates of observations at Lijiang and CAHA. Columns (6)–(8) indicate the number of spectroscopic epochs, the median sampling cadence, and the total duration of the entire spectroscopic monitoring period. Finally, Columns (9) and (10) present the coordinates of the comparison star used in the spectroscopic observations.

Table 2. Light Curves

J082338					J083525				
Photometry		Spectra			Photometry		Spectra		
JD	F_{phot}	JD	F_{3000}	F_{MgII}	JD	F_{phot}	JD	F_{3000}	F_{MgII}
53.343	2.216 ± 0.039	53.353	2.176 ± 0.072	4.388 ± 0.216	55.316	4.934 ± 0.036	55.343	4.937 ± 0.113	13.642 ± 0.099
54.349	2.214 ± 0.038	54.323	2.272 ± 0.073	4.534 ± 0.058	76.391	4.900 ± 0.032	67.316	4.875 ± 0.095	13.204 ± 0.142
66.272	2.280 ± 0.058	66.291	2.325 ± 0.073	4.292 ± 0.200	79.235	4.861 ± 0.034	79.262	4.806 ± 0.114	12.952 ± 0.117
76.336	2.263 ± 0.032	78.381	2.296 ± 0.073	4.419 ± 0.082	84.291	4.878 ± 0.032	88.331	5.029 ± 0.128	13.820 ± 0.122
78.360	2.324 ± 0.027	87.299	2.305 ± 0.073	4.121 ± 0.173	99.284	4.905 ± 0.031	99.311	4.844 ± 0.112	13.162 ± 0.090

NOTE—Julian date (JD) is from 2,458,000. F_{phot} , F_{3000} , and F_{MgII} are the fluxes of photometric continuum, spectroscopic continuum, and Mg II line, respectively. The continuum fluxes and uncertainties are the values after the PYCALI intercalibration. The continuum and Mg II fluxes are in units of $10^{-16} \text{ erg s}^{-1} \text{ cm}^{-2} \text{ \AA}^{-1}$ and $10^{-15} \text{ erg s}^{-1} \text{ cm}^{-2}$, respectively.

Blandford, R. D. & McKee, C. F. 1982, ApJ, 255, 419.

doi:10.1086/159843

Boroson, T. A. & Green, R. F. 1992, ApJS, 80, 109.

doi:10.1086/191661

Boroson, T. A. 2002, ApJ, 565, 78. doi:10.1086/324486

Cackett, E. M., Gültekin, K., Bentz, M. C., et al. 2015, ApJ, 810, 86. doi:10.1088/0004-637X/810/2/86

Chen, Y.-J., Liu, J.-R., Zhai, S., et al. 2023, MNRAS, 522, 3, 3439.

doi:10.1093/mnras/stad1136

Czerny, B., Olejak, A., Rałowski, M., et al. 2019, ApJ, 880, 46.

doi:10.3847/1538-4357/ab2913

De Rosa, G., Fausnaugh, M. M., Grier, C. J., et al. 2018, ApJ, 866,

133. doi:10.3847/1538-4357/aadd11

Table 3. Light-curve Statistics

Object	3000 Å		Mg II	
	Flux	F_{var}	Flux	F_{var}
	($10^{-16} \text{erg s}^{-1} \text{cm}^{-2} \text{Å}^{-1}$)	(%)	($10^{-15} \text{erg s}^{-1} \text{cm}^{-2}$)	(%)
J082338	2.402 ± 0.111	4.6 ± 0.6	4.533 ± 0.226	4.4 ± 0.6
J083525	4.876 ± 0.231	4.6 ± 0.4	13.288 ± 0.530	3.8 ± 0.4
J083826	3.075 ± 0.231	7.4 ± 0.5	8.256 ± 0.408	4.7 ± 0.5
J084141	3.960 ± 0.180	4.6 ± 0.3	13.441 ± 0.441	3.0 ± 0.3
J084808	4.720 ± 0.179	3.8 ± 0.8	8.317 ± 0.491	5.6 ± 0.8
J085557	6.993 ± 0.481	6.9 ± 0.5	16.526 ± 0.917	5.4 ± 0.5
J090628	4.226 ± 0.540	12.9 ± 0.4	10.666 ± 0.558	5.1 ± 0.4
J091245	4.976 ± 0.557	11.2 ± 0.6	10.084 ± 0.568	5.4 ± 0.6
J092835	3.823 ± 0.281	7.1 ± 0.7	7.473 ± 0.597	7.6 ± 0.7
J093857	3.833 ± 0.359	9.4 ± 0.5	9.335 ± 0.446	4.3 ± 0.5
J094009	3.724 ± 0.216	5.8 ± 0.3	11.028 ± 0.472	4.1 ± 0.3
J094607	3.820 ± 0.437	11.5 ± 0.6	8.474 ± 0.667	7.6 ± 0.6
J094801	4.597 ± 0.272	5.8 ± 0.5	10.297 ± 0.441	4.0 ± 0.5
J100254	6.475 ± 0.989	15.4 ± 0.4	14.513 ± 0.669	4.5 ± 0.4
J100955	2.967 ± 0.499	16.9 ± 0.9	6.912 ± 0.665	9.5 ± 0.9
J101227	4.109 ± 0.258	6.3 ± 0.5	7.013 ± 0.283	3.4 ± 0.5
J101622	4.347 ± 0.253	5.9 ± 0.4	9.220 ± 0.498	5.1 ± 0.4
J101730	3.166 ± 0.054	1.4 ± 0.6	7.625 ± 0.362	4.4 ± 0.6

NOTE—The flux and its uncertainty listed represent the mean and standard deviation measured from the spectroscopic continuum and Mg II light curves. F_{var} denotes the fractional variability amplitude and its uncertainty, as defined in Section 3.4.

Table 4. Time Lags

Name	r_{max}	$\tau_{\text{ICCF}}^{\text{obs}}$	$\tau_{\text{MICA}}^{\text{obs}}$	$\tau_{\text{ICCF}}^{\text{rest}}$	$\tau_{\text{MICA}}^{\text{rest}}$	FWHM	σ_{line}	$\log(L_{3000}/\text{erg s}^{-1})$	$\log(M_{\bullet}/M_{\odot})$	$\mathcal{R}_{\text{Fe,UV}}$	$\log \dot{\mathcal{M}}$
		(day)	(day)	(day)	(day)	(km s $^{-1}$)	(km s $^{-1}$)				
(1)	(2)	(3)	(4)	(5)	(6)	(7)	(8)	(9)	(10)	(11)	(12)
J083826	0.79	108^{+28}_{-28}	132^{+23}_{-12}	59^{+15}_{-16}	72^{+13}_{-7}	3037^{+172}_{-223}	3183^{+144}_{-134}	45.76 ± 0.03	$8.11^{+0.09}_{-0.08}$	0.74 ± 0.02	$1.444^{+0.157}_{-0.186}$
J090628	0.69	250^{+67}_{-32}	244^{+37}_{-27}	132^{+36}_{-17}	130^{+20}_{-14}	2887^{+255}_{-291}	2707^{+155}_{-156}	46.00 ± 0.06	$8.32^{+0.10}_{-0.10}$	1.18 ± 0.05	$1.384^{+0.213}_{-0.221}$
J091245	0.72	323^{+141}_{-141}	260^{+36}_{-37}	186^{+81}_{-81}	150^{+21}_{-22}	2222^{+180}_{-229}	2108^{+156}_{-145}	45.84 ± 0.05	$8.16^{+0.09}_{-0.11}$	1.35 ± 0.04	$1.474^{+0.231}_{-0.200}$
J093857	0.62	278^{+31}_{-32}	264^{+29}_{-45}	159^{+18}_{-19}	152^{+17}_{-26}	3737^{+276}_{-310}	2772^{+242}_{-211}	45.73 ± 0.04	$8.62^{+0.08}_{-0.10}$	1.30 ± 0.14	$0.392^{+0.215}_{-0.171}$
J094607	0.82	168^{+42}_{-41}	150^{+52}_{-27}	96^{+24}_{-24}	85^{+29}_{-15}	2834^{+273}_{-308}	2963^{+129}_{-163}	45.76 ± 0.05	$8.13^{+0.17}_{-0.12}$	0.86 ± 0.03	$1.419^{+0.255}_{-0.352}$
J094801	0.75	218^{+29}_{-31}	240^{+33}_{-20}	119^{+16}_{-17}	131^{+18}_{-11}	3200^{+171}_{-221}	2670^{+156}_{-173}	45.95 ± 0.03	$8.42^{+0.08}_{-0.07}$	1.03 ± 0.03	$1.122^{+0.144}_{-0.158}$
J100254	0.61	310^{+85}_{-58}	389^{+50}_{-48}	170^{+46}_{-32}	213^{+27}_{-26}	3210^{+171}_{-222}	2809^{+141}_{-133}	46.10 ± 0.07	$8.63^{+0.07}_{-0.08}$	0.75 ± 0.02	$0.919^{+0.185}_{-0.178}$
J100955	0.90	170^{+42}_{-29}	178^{+33}_{-19}	93^{+23}_{-16}	98^{+18}_{-11}	3404^{+172}_{-222}	3108^{+141}_{-150}	45.74 ± 0.08	$8.34^{+0.09}_{-0.07}$	0.90 ± 0.03	$0.955^{+0.181}_{-0.221}$

NOTE—Column (1) presents the names of the targets. Column (2) provides the peak values (r_{max}) of the cross-correlation functions. Columns (3)–(6) list the time lags and uncertainties measured from the ICCF and MICA methods in both the observed and rest frames. Columns (7) and (8) indicate the FWHM and σ_{line} of the Mg II line, respectively. Column (9) presents the monochromatic continuum luminosities at 3000 Å along with their uncertainties. Column (10) gives the black hole masses and their uncertainties, noting that the uncertainty in the f factor is not included. Finally, Column (11) and (12) present the ultraviolet iron ratio $\mathcal{R}_{\text{Fe,UV}}$ and the dimensionless accretion rate $\dot{\mathcal{M}}$ measured, respectively.

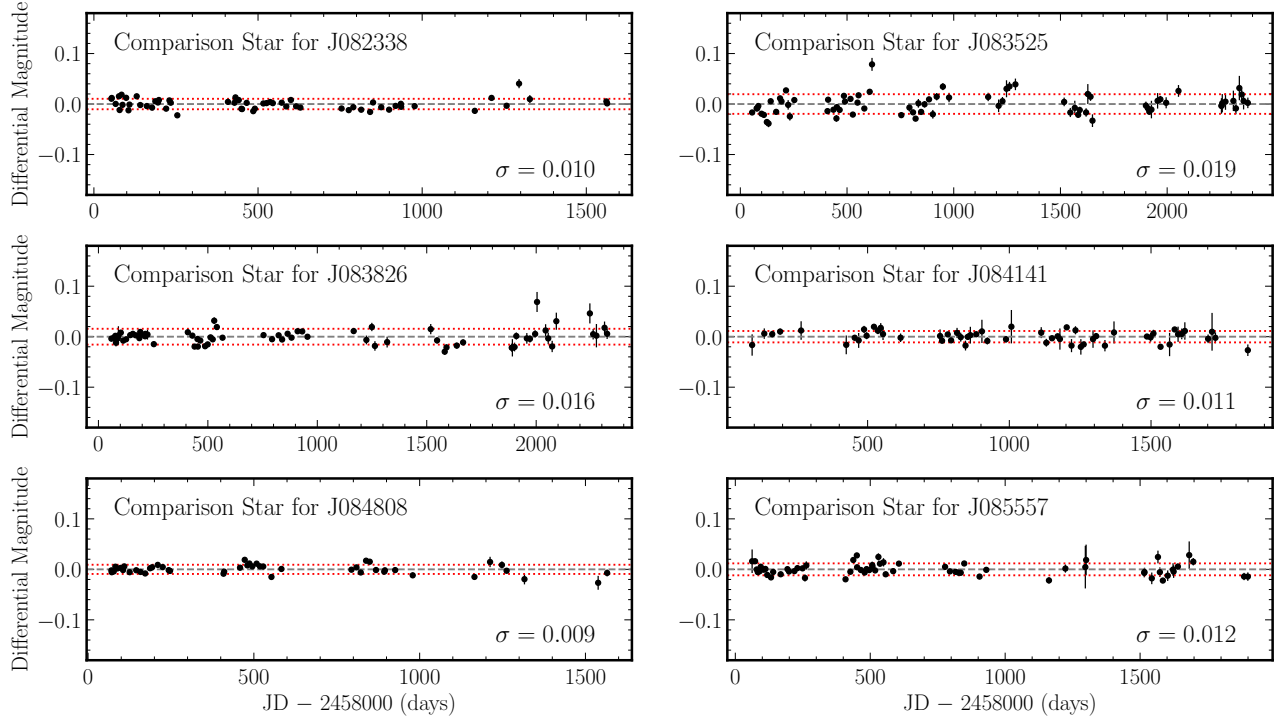


Figure 10. Photometric light curves of comparison stars in the slits. The standard deviations are represented by red dotted lines and explicitly written as σ in each panel.

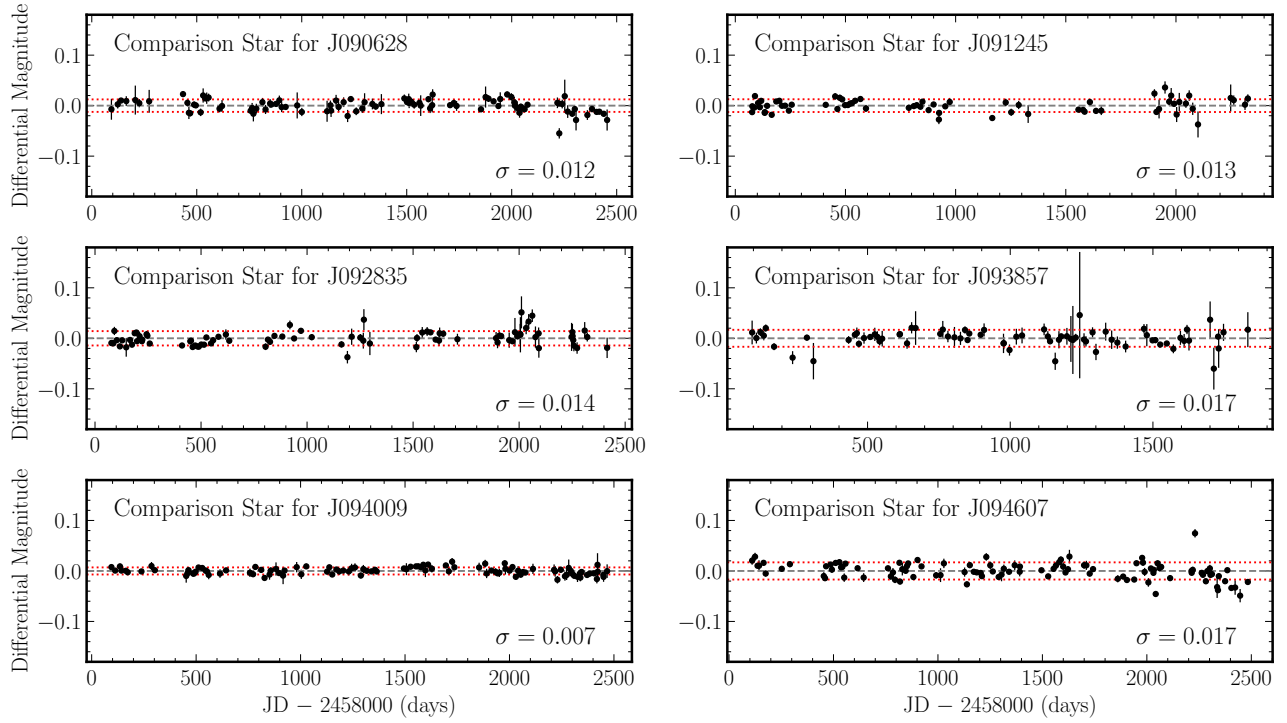


Figure 10. (Continued.)

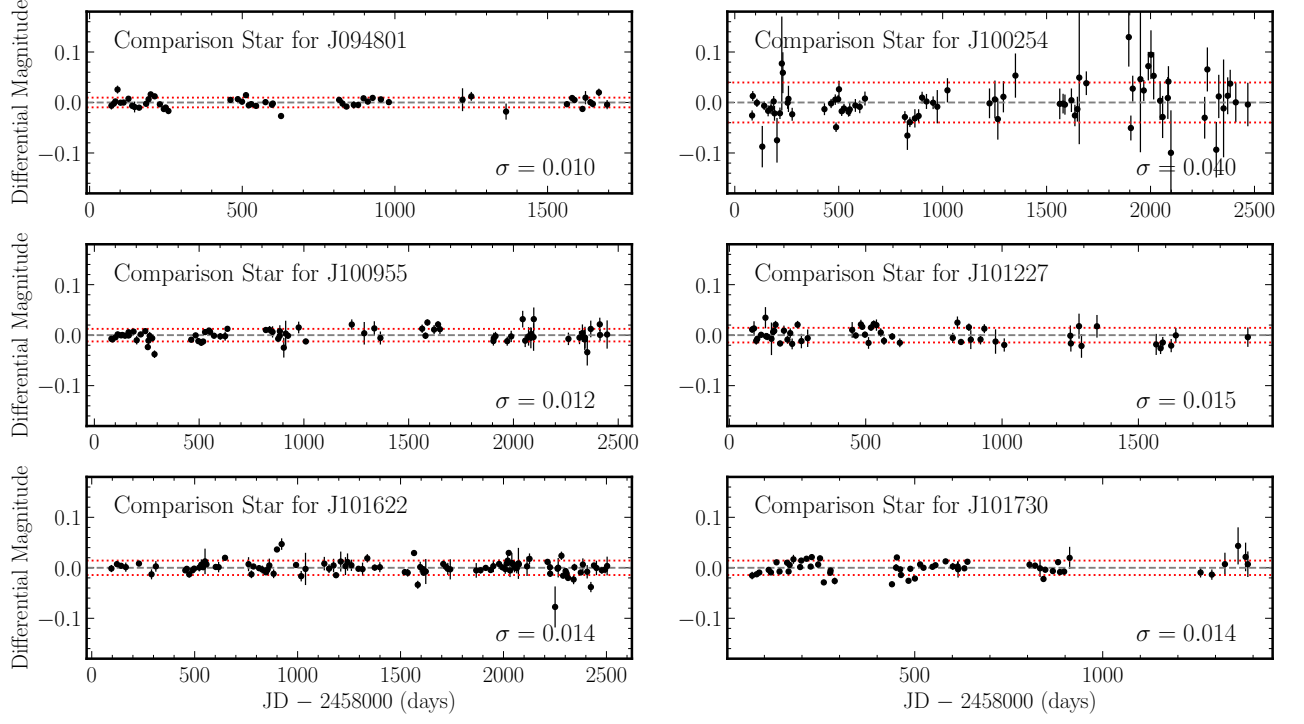


Figure 10. (Continued.)

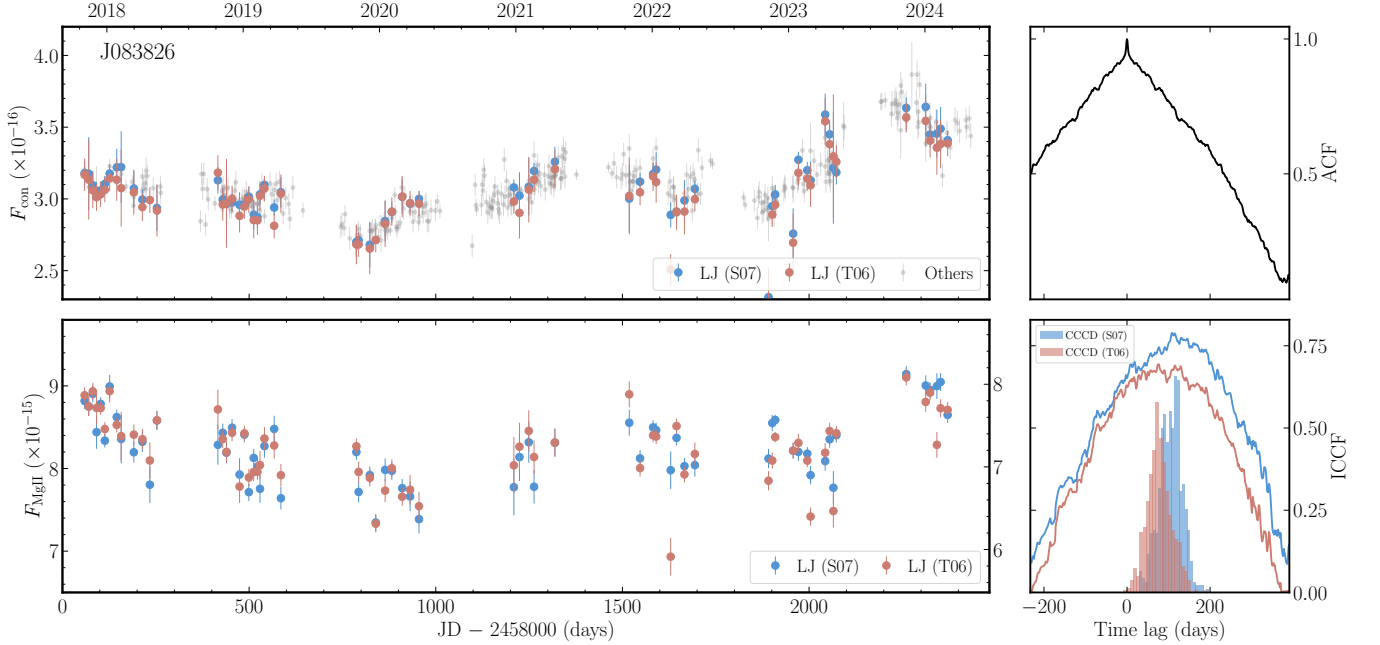


Figure 11. Comparison between light curves and time-lag measurements for using two iron templates: [Salviander et al. \(2007\)](#) and [Tsuzuki et al. \(2006\)](#). Meanings of panels are the same as Figure 3. “LJ/CAHA (S07/T06)” represents the Lijiang/CAHA spectroscopic data measured using the iron template of [Salviander et al. \(2007\)](#) or [Tsuzuki et al. \(2006\)](#). “Others” stands for the photometric data of ZTF or Lijiang/CAHA. Data points of the Mg II light curve corresponding to [Salviander et al. \(2007\)](#) and [Tsuzuki et al. \(2006\)](#) templates should be referenced against the tick labels on the left and right, respectively. The complete figure set (8 images) is available in the online article.

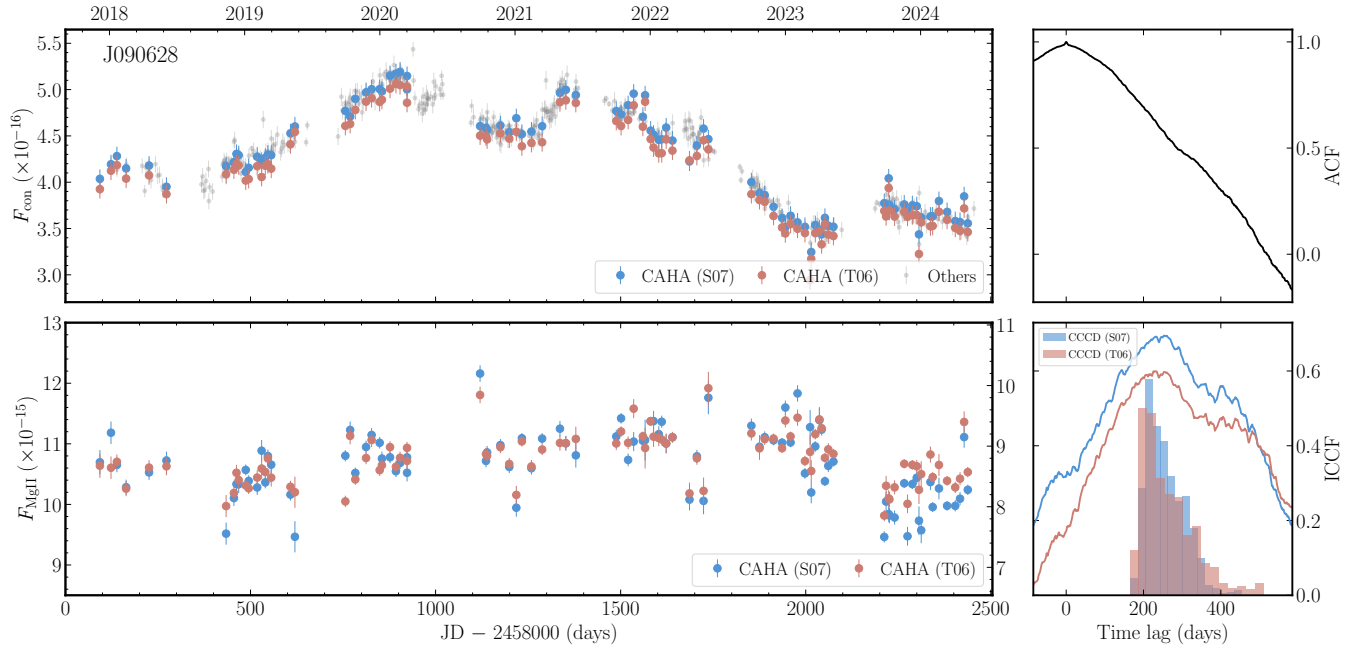


Figure 11. (Continued.)

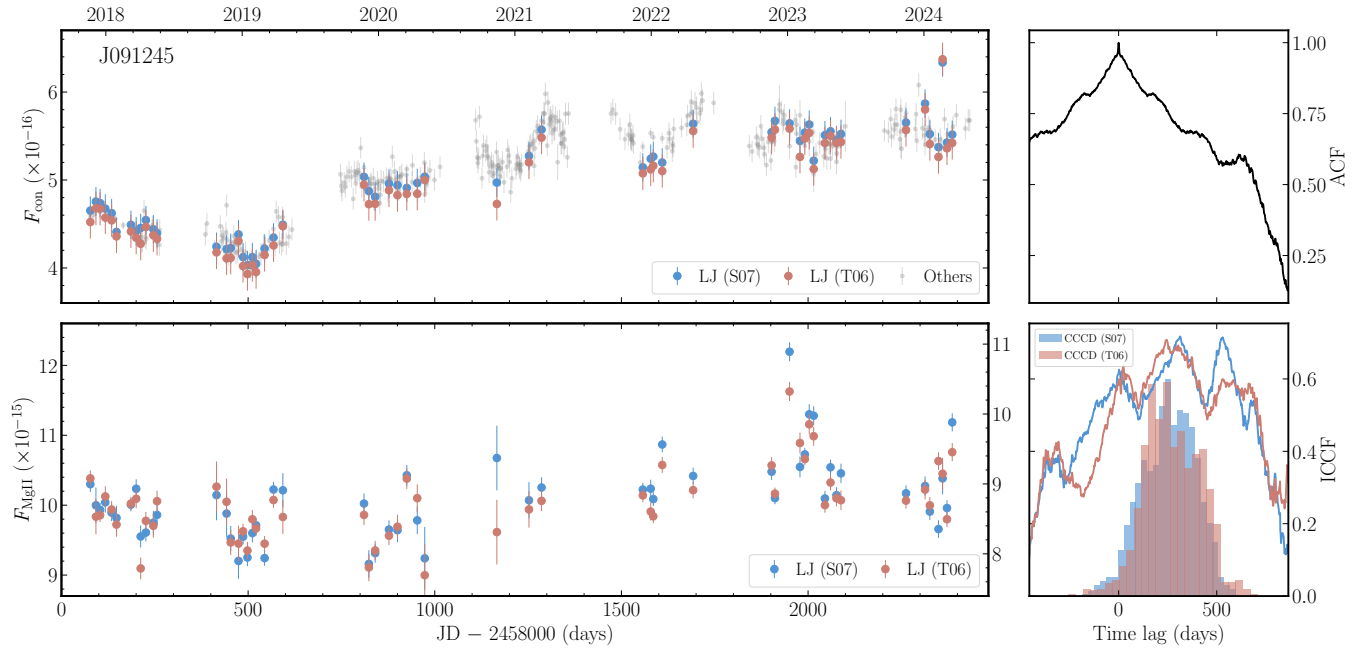


Figure 11. (Continued.)

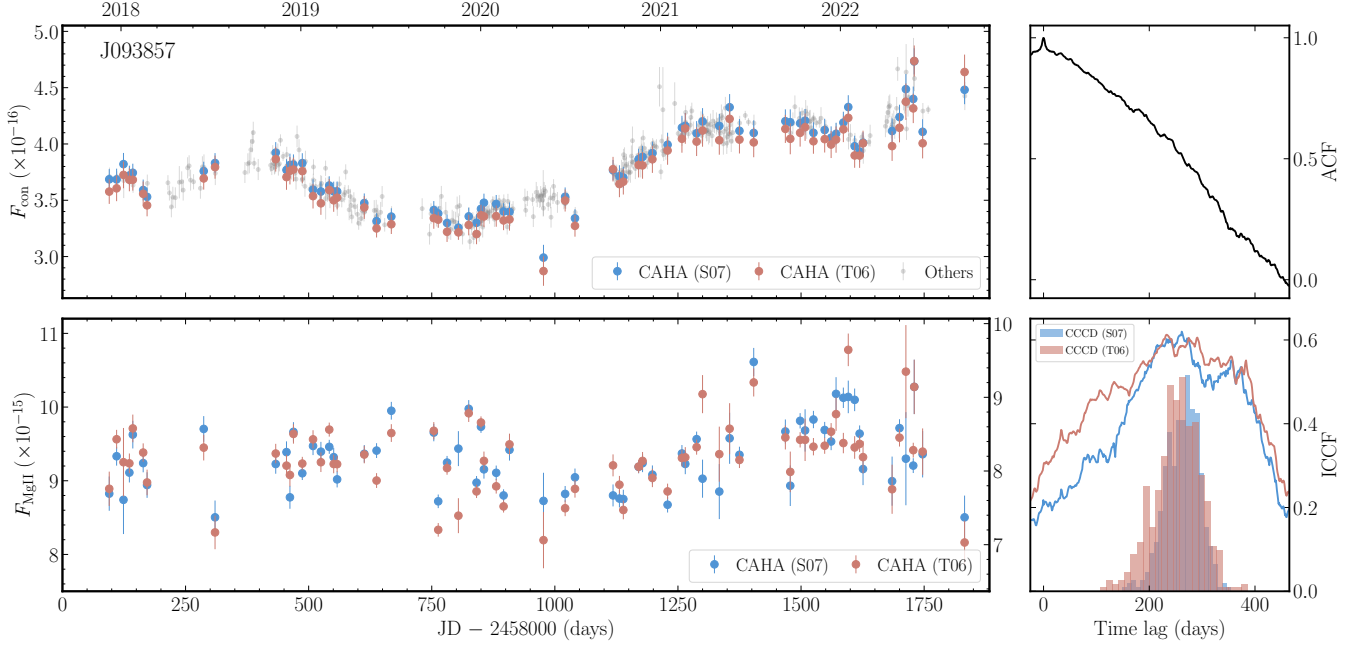


Figure 11. (Continued.)

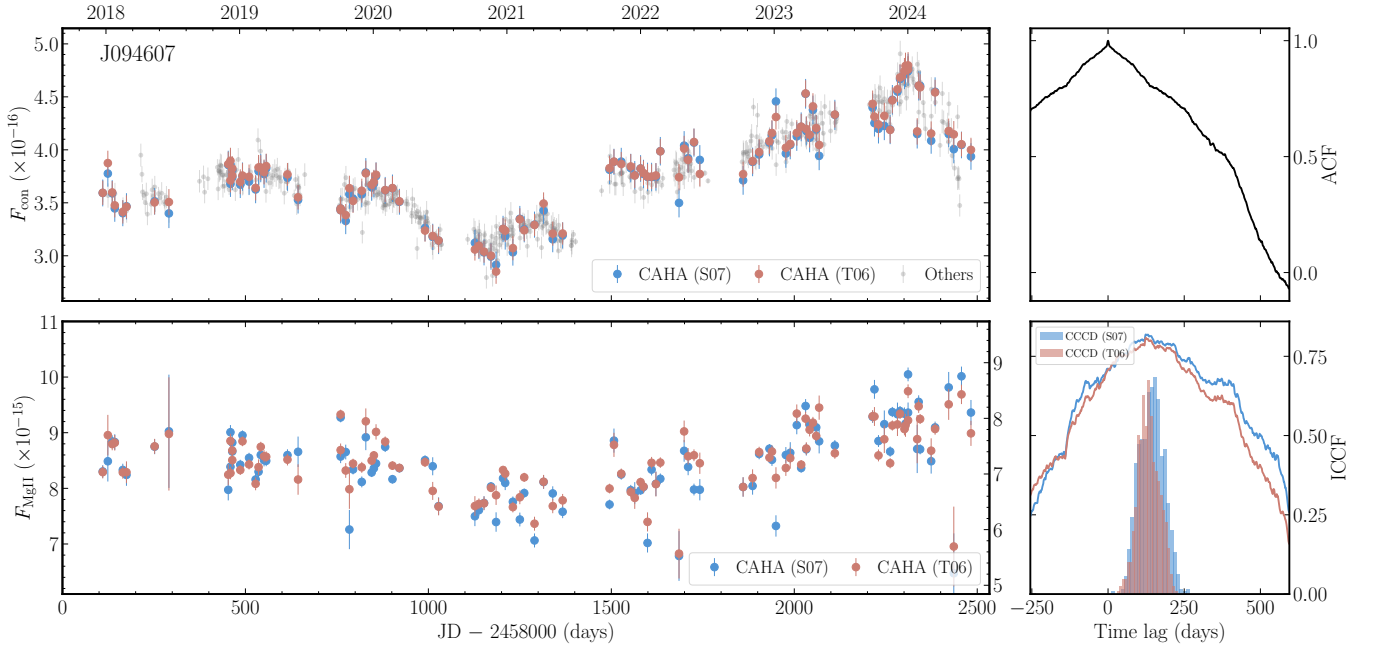


Figure 11. (Continued.)

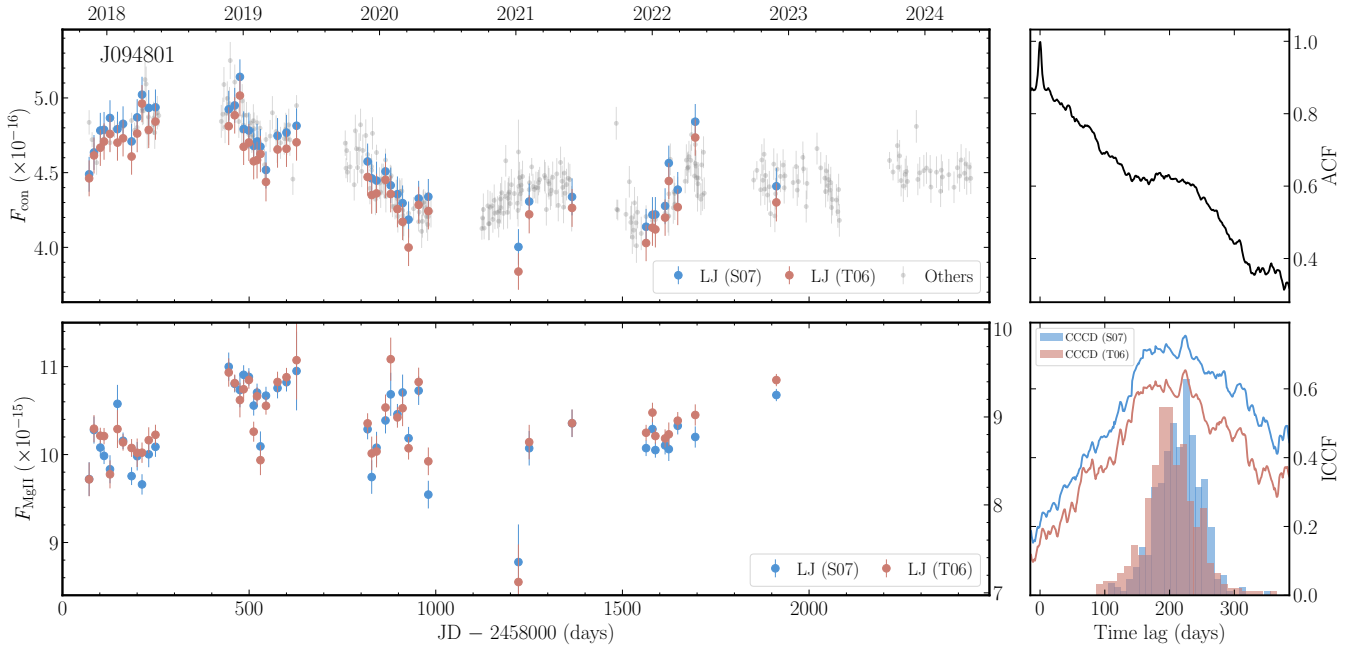


Figure 11. (Continued.)

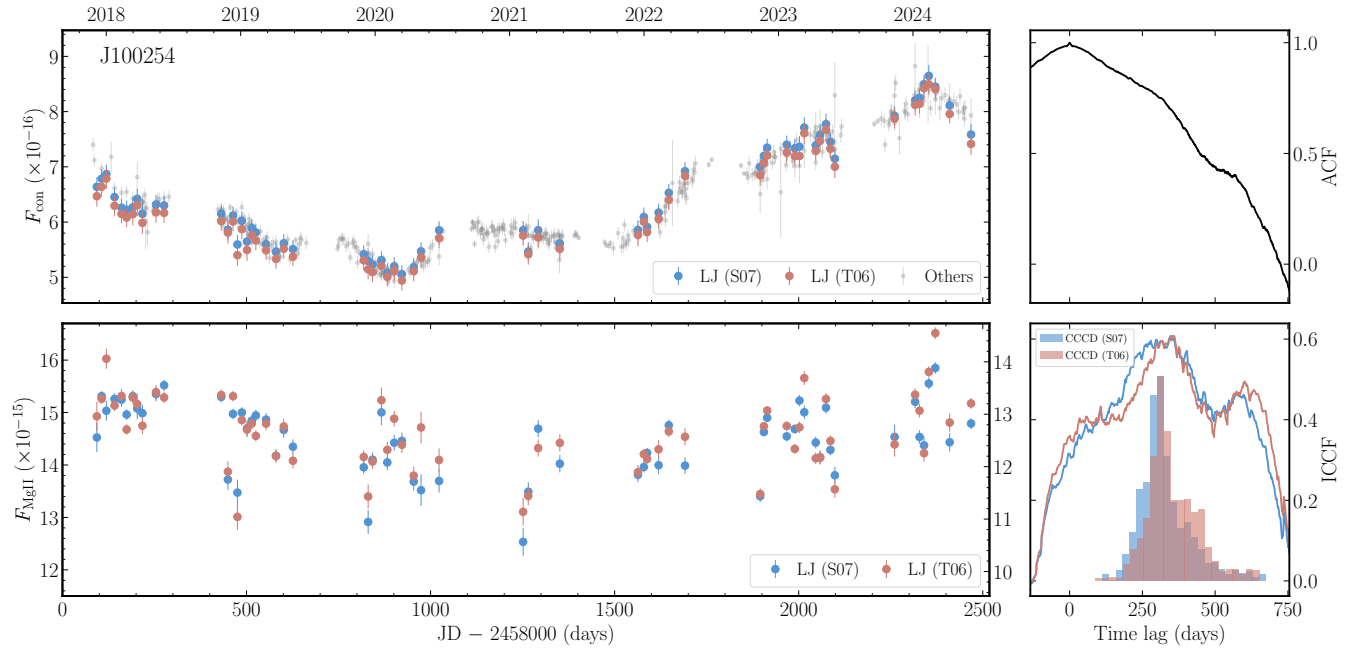


Figure 11. (Continued.)

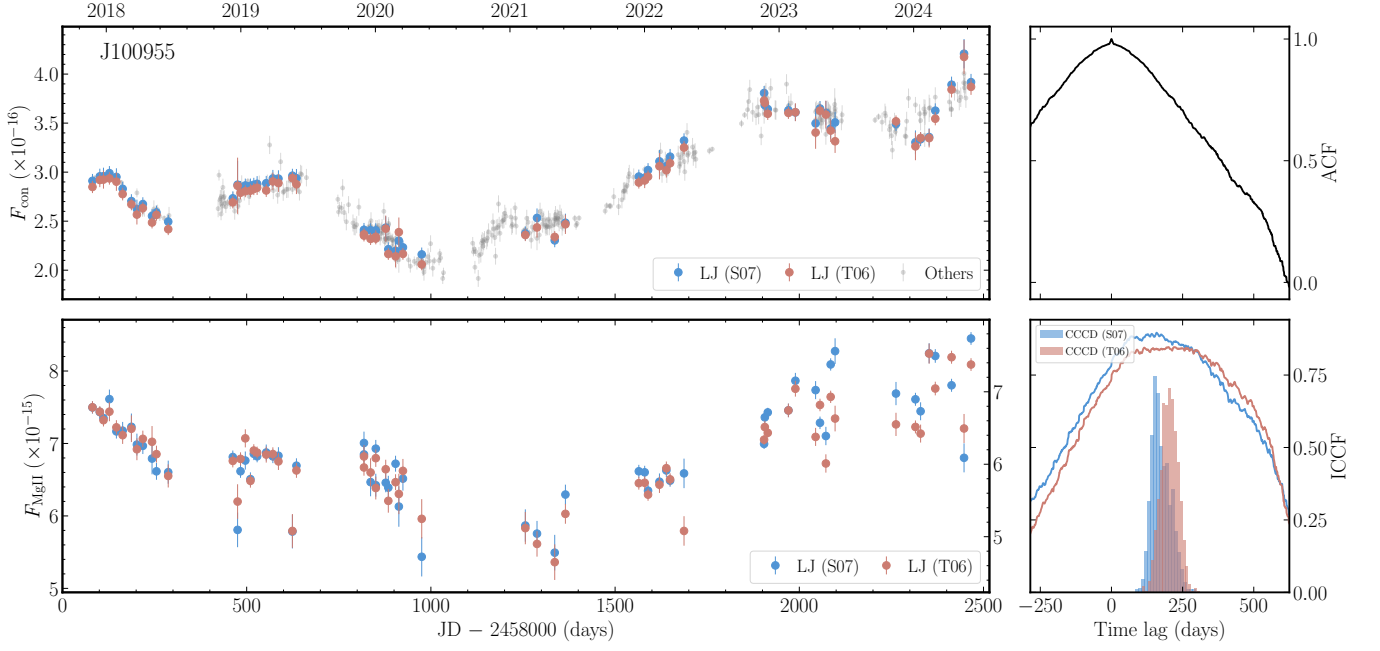


Figure 11. (Continued.)

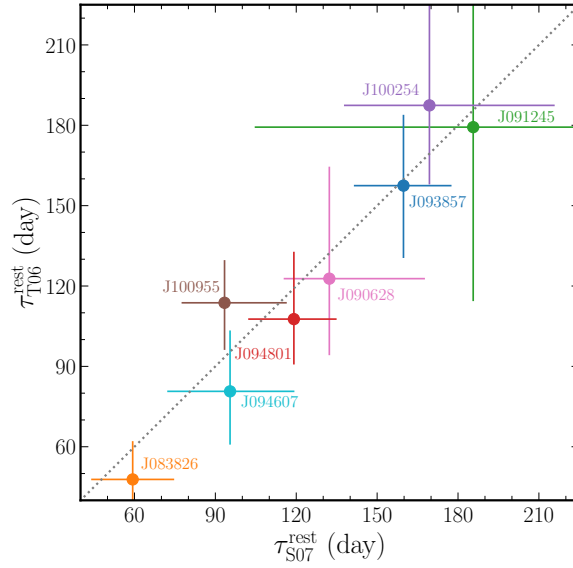


Figure 12. Comparison between the lag in the rest frame derived from the light curve by employing Salviander et al. (2007) ($\tau_{\text{S07}}^{\text{rest}}$) and Tsuzuki et al. (2006) ($\tau_{\text{T06}}^{\text{rest}}$) iron templates, via ICCF method.

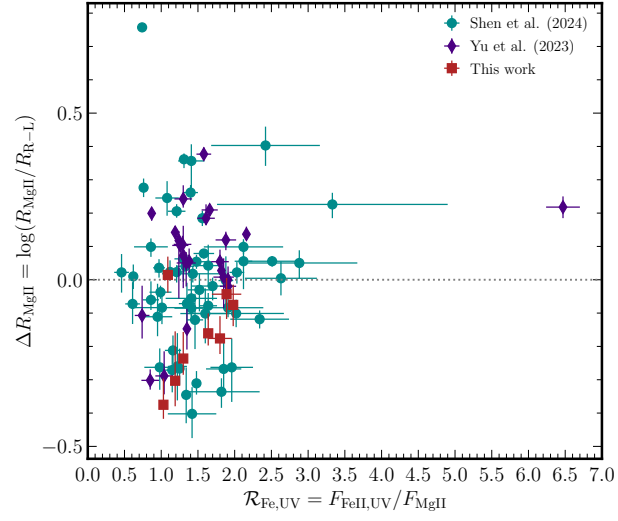


Figure 13. Correlation of ΔR_{MgII} with the UV iron strength $\mathcal{R}_{\text{Fe,UV}}$ by employing iron template from Tsuzuki et al. (2006). The figure is plotted in the same manner as Figure 7.

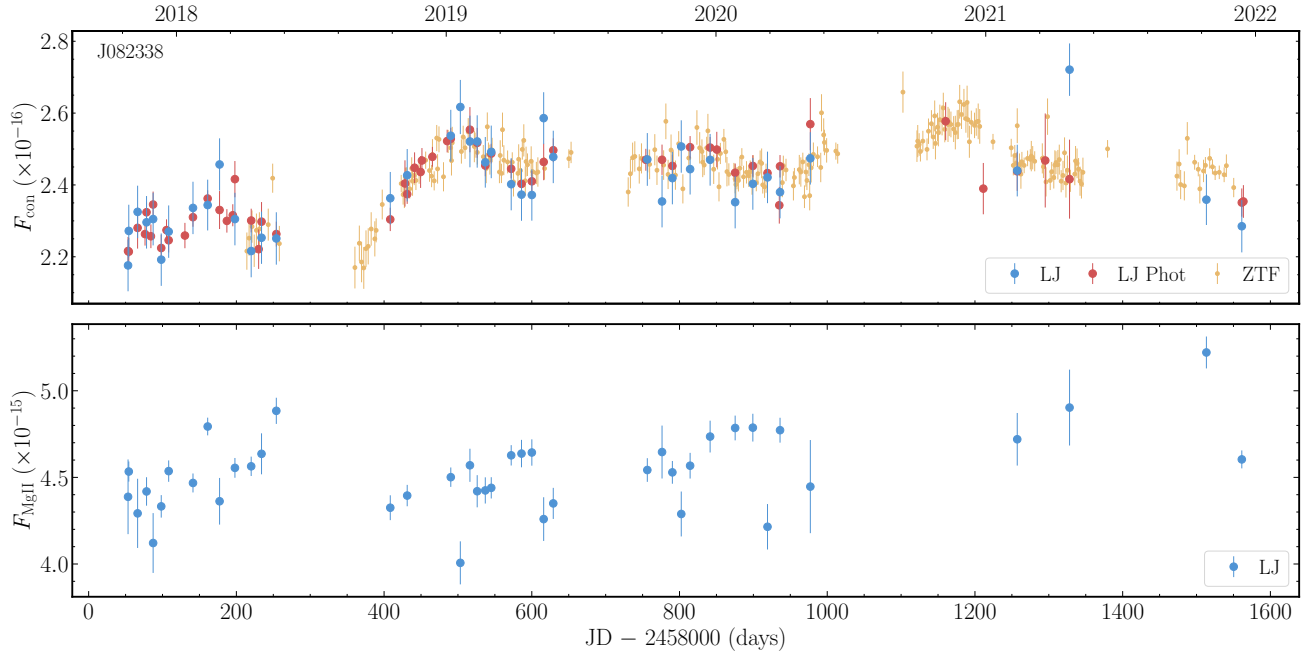


Figure 14. Light curves of targets without successful lag measurements, plotted in the same manner as in Figure 3. The complete figure set (10 images) is available in the online article.

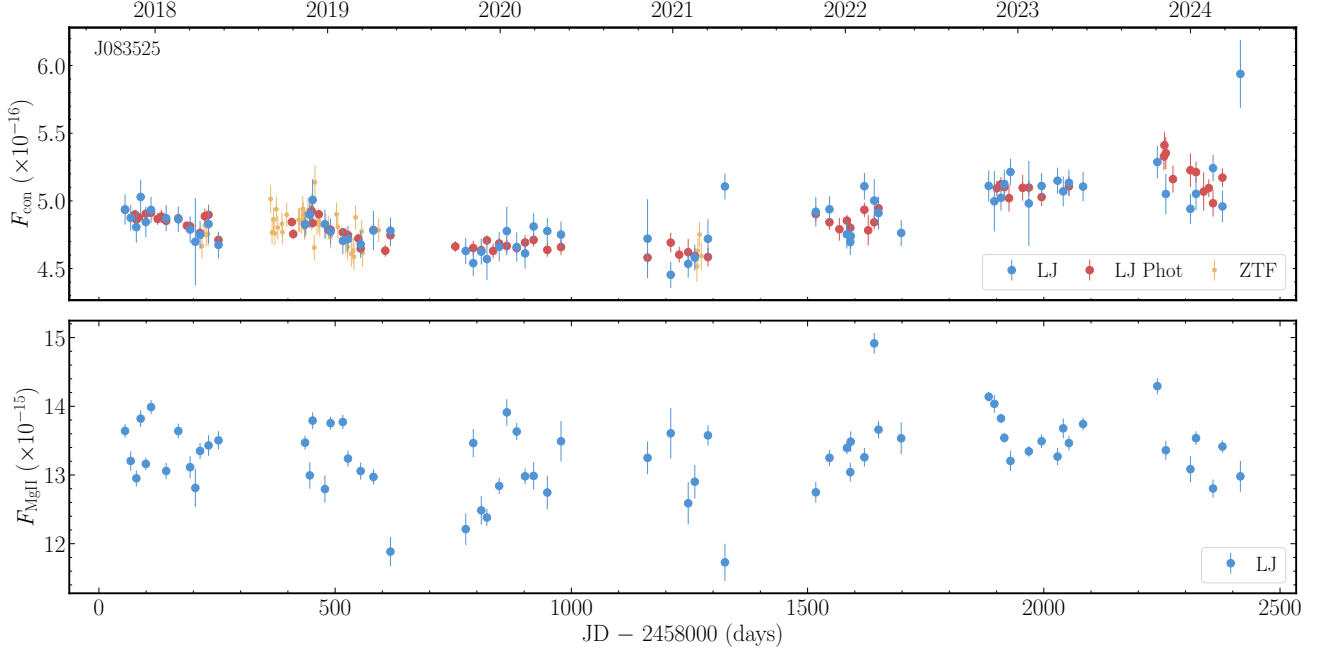


Figure 14. (Continued.)

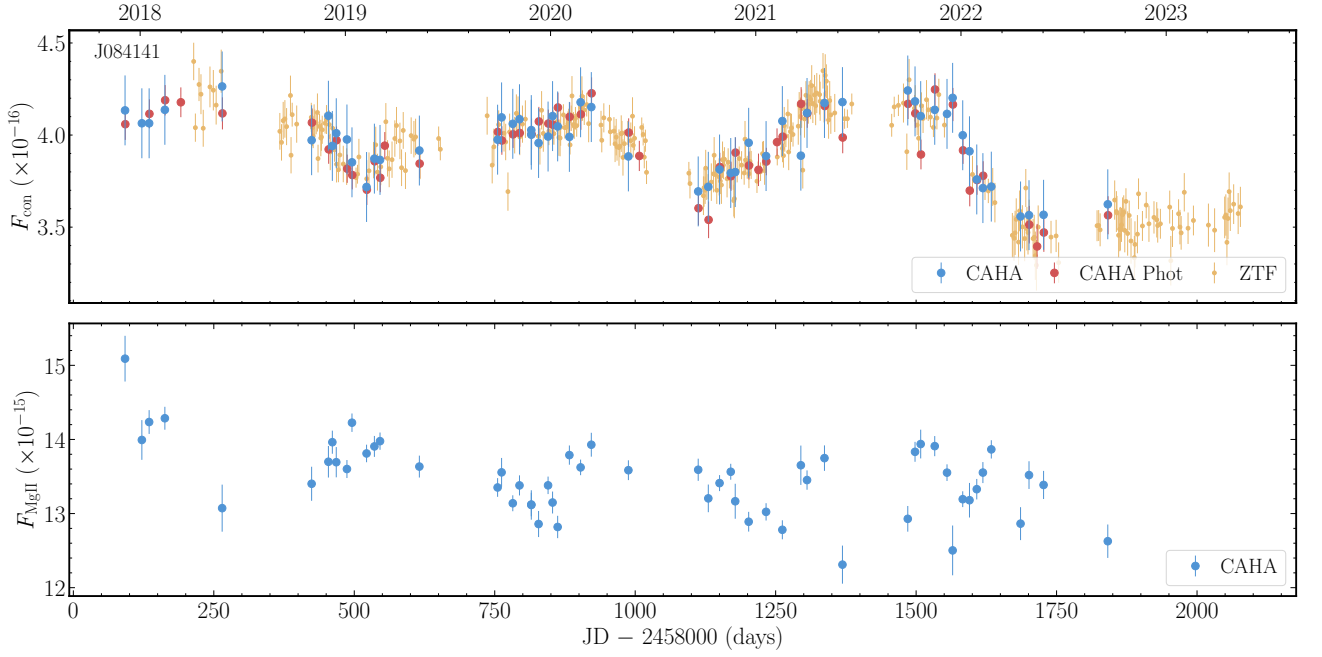


Figure 14. (Continued.)

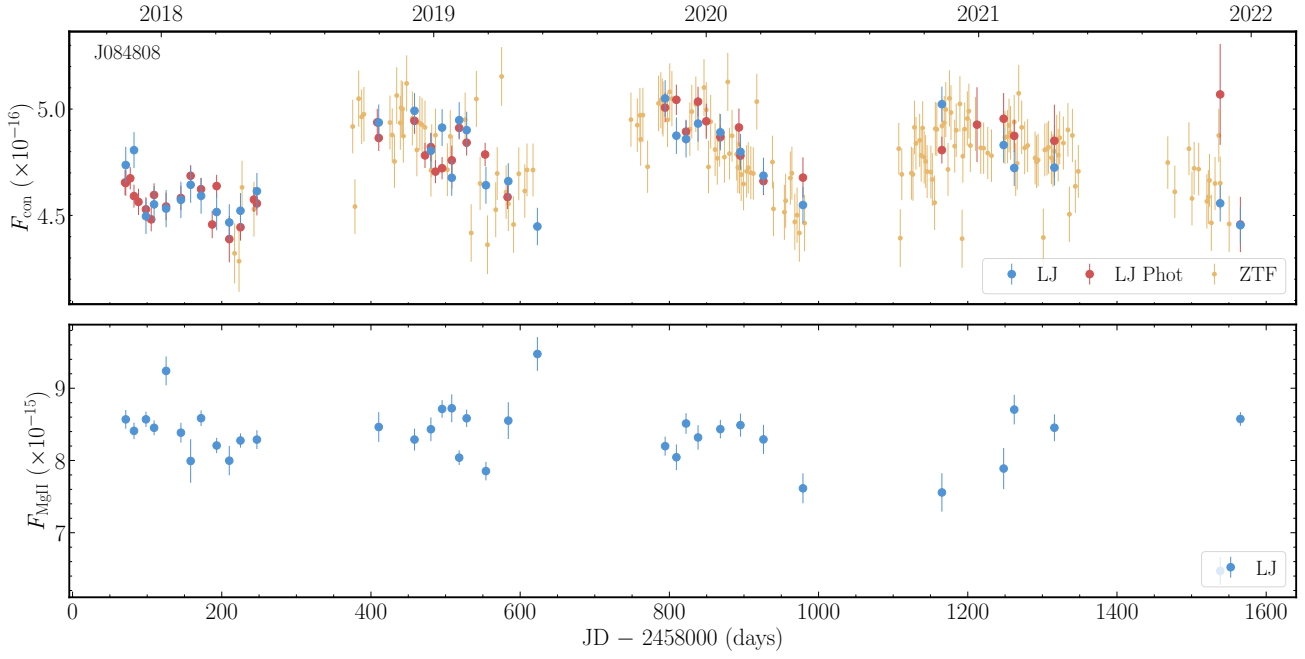


Figure 14. (Continued.)

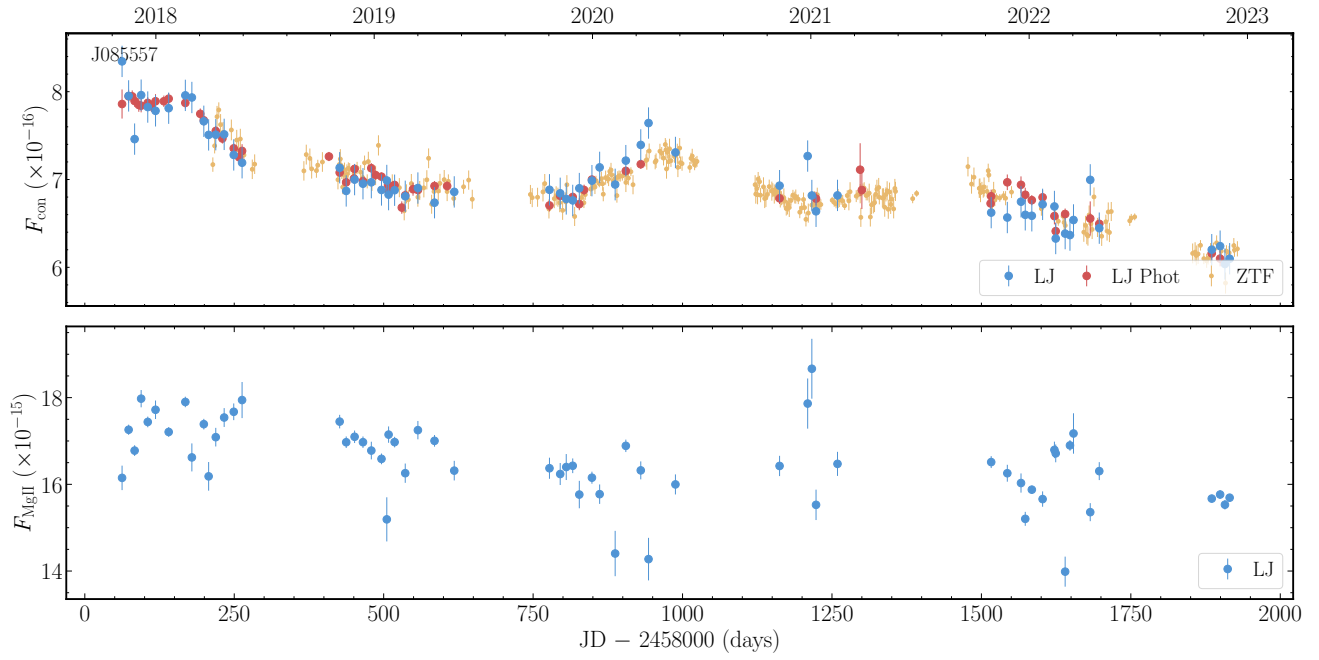


Figure 14. (Continued.)

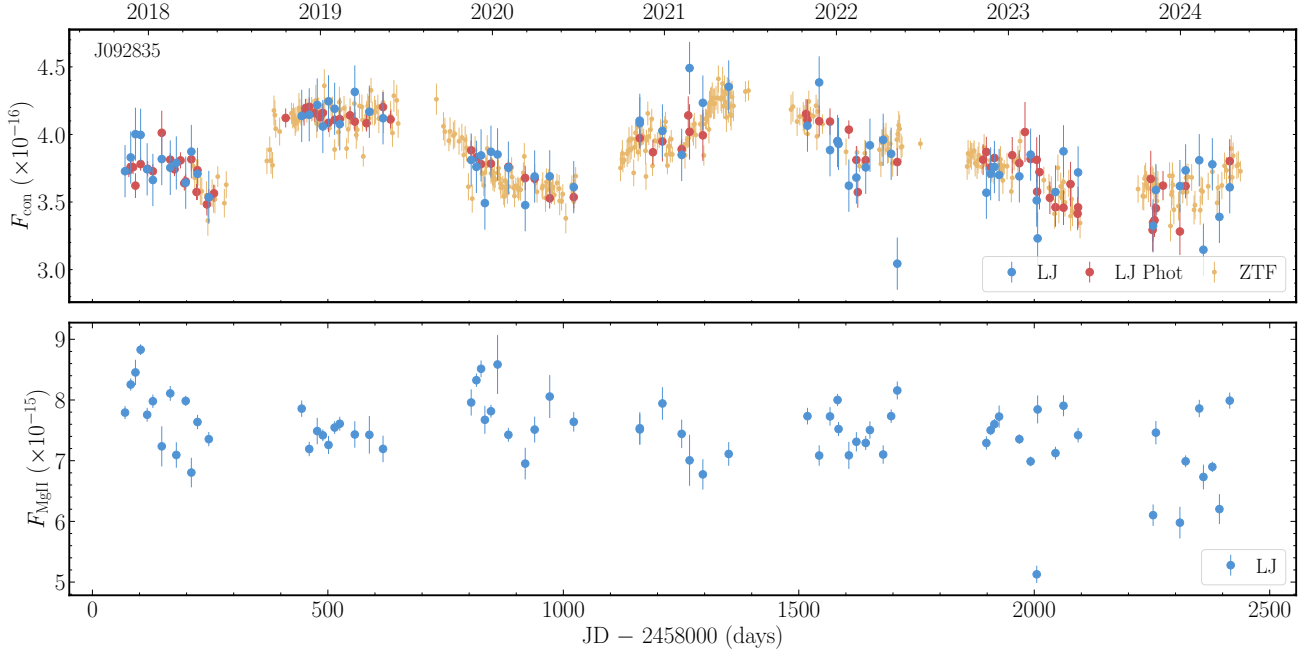


Figure 14. (Continued.)

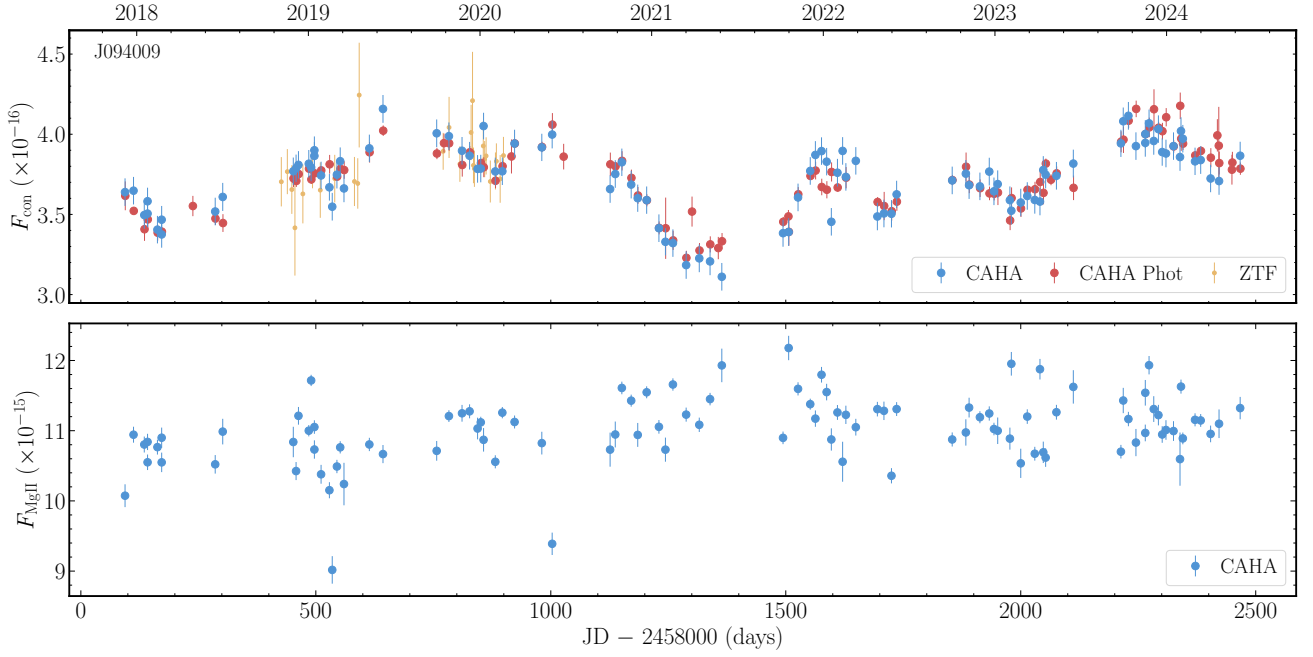


Figure 14. (Continued.)

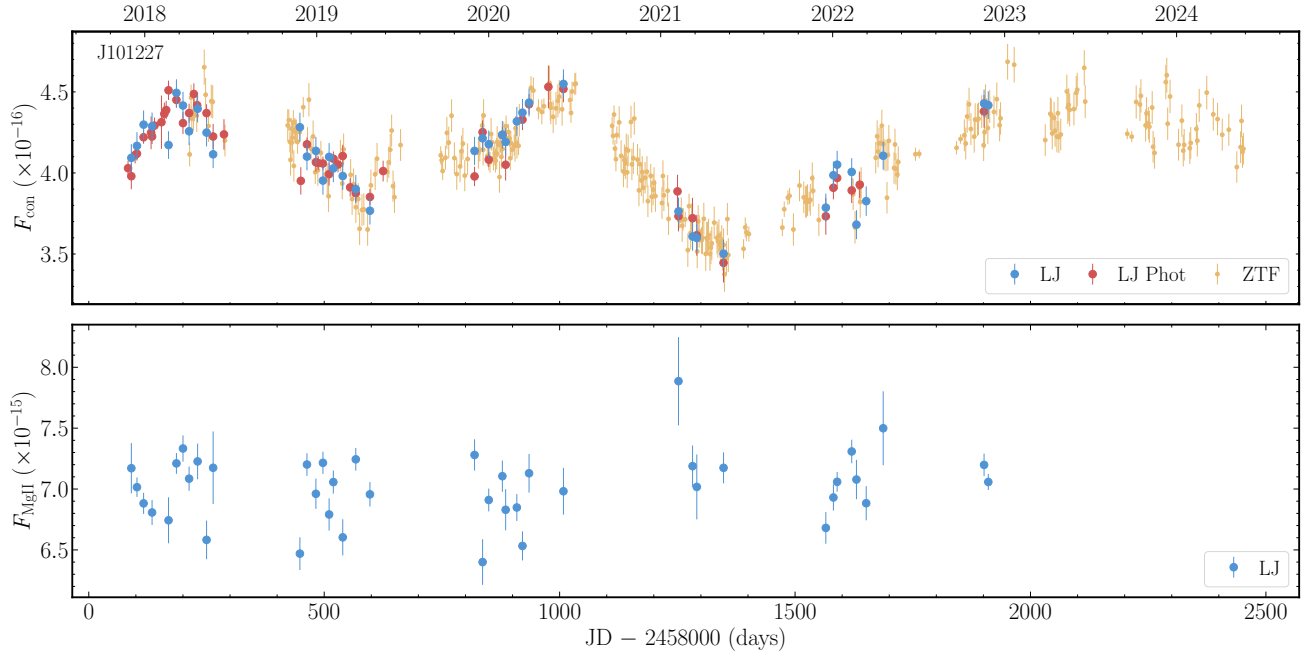


Figure 14. (Continued.)

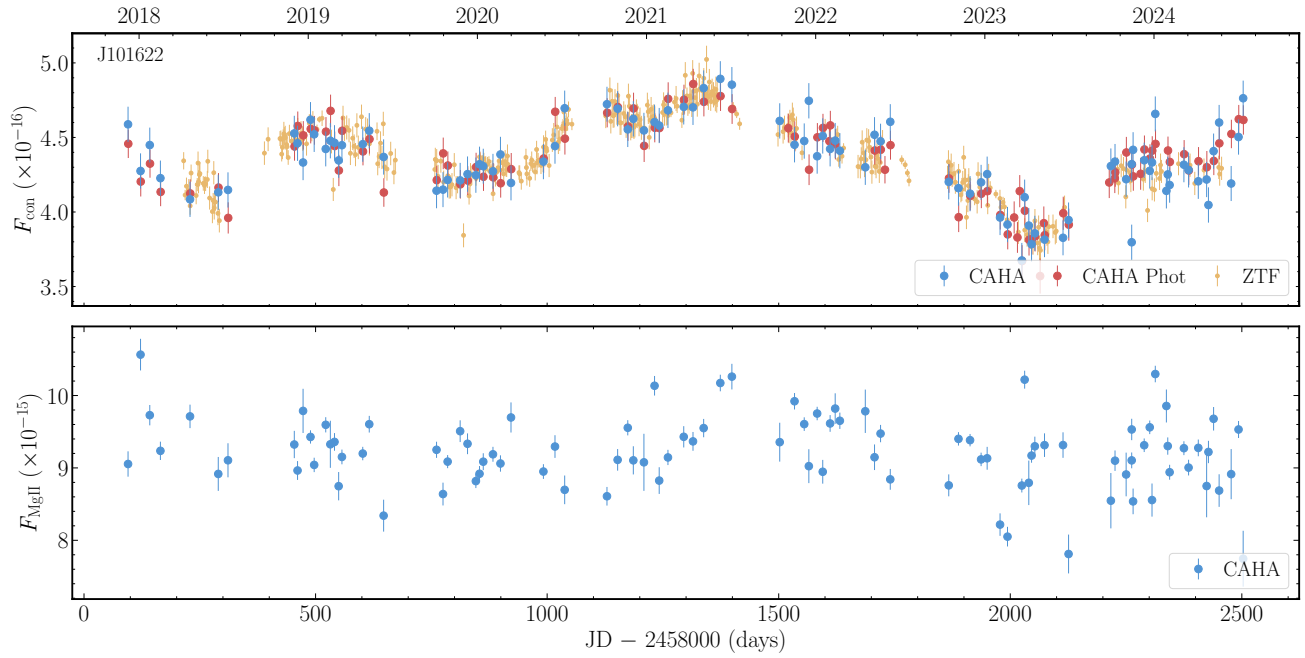


Figure 14. (Continued.)

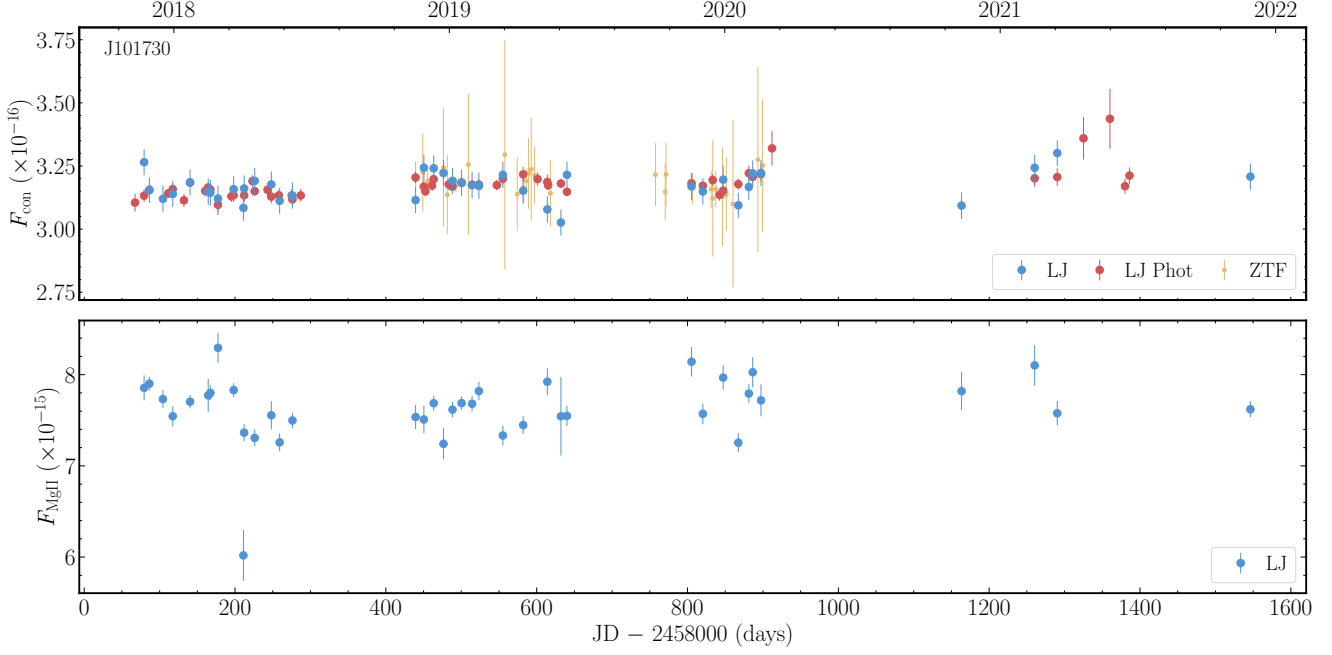


Figure 14. (Continued.)

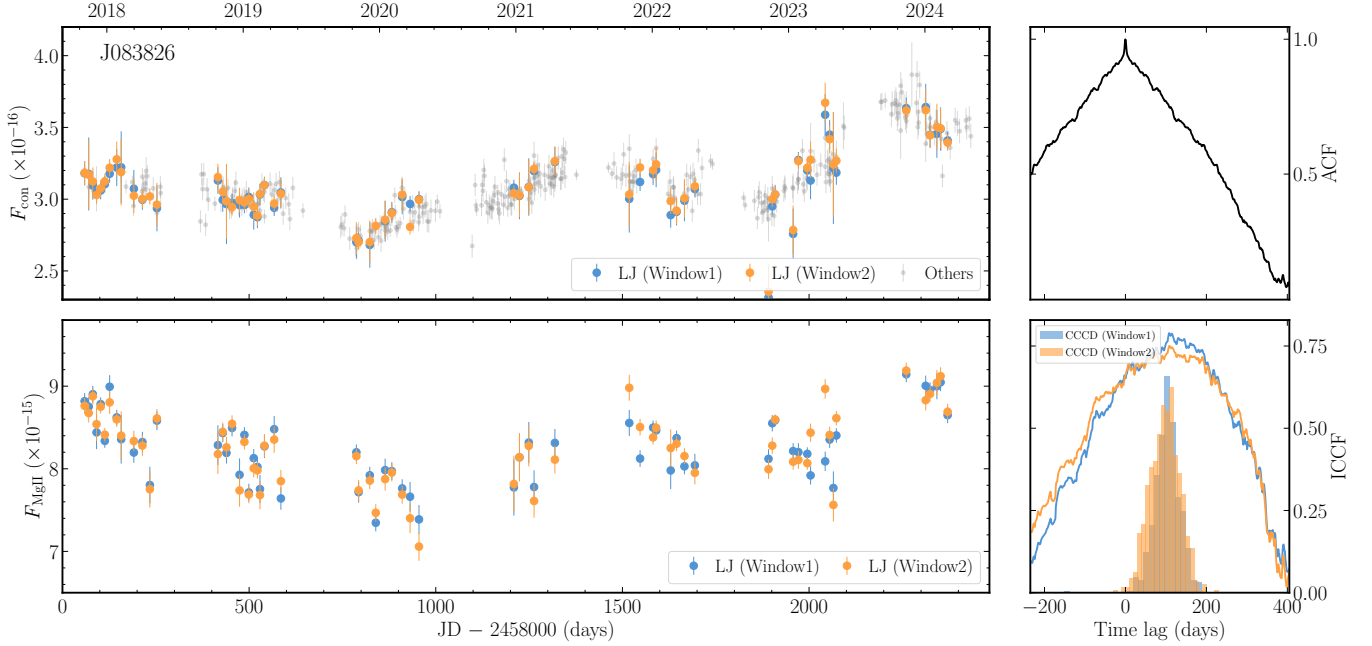


Figure 15. Comparison between light curves and time-lag measurements for two fitting windows: Window 1 (2260-3050 Å) and Window 2 (2260-3400 Å). Meanings of panels are the same as Figure 3. “LJ/CAHA (Window1/2)” represents the Lijiang/CAHA spectroscopic data using the corresponding fitting window. “Others” stands for the photometric data of ZTF or Lijiang/CAHA. The complete figure set (8 images) is available in the online article.

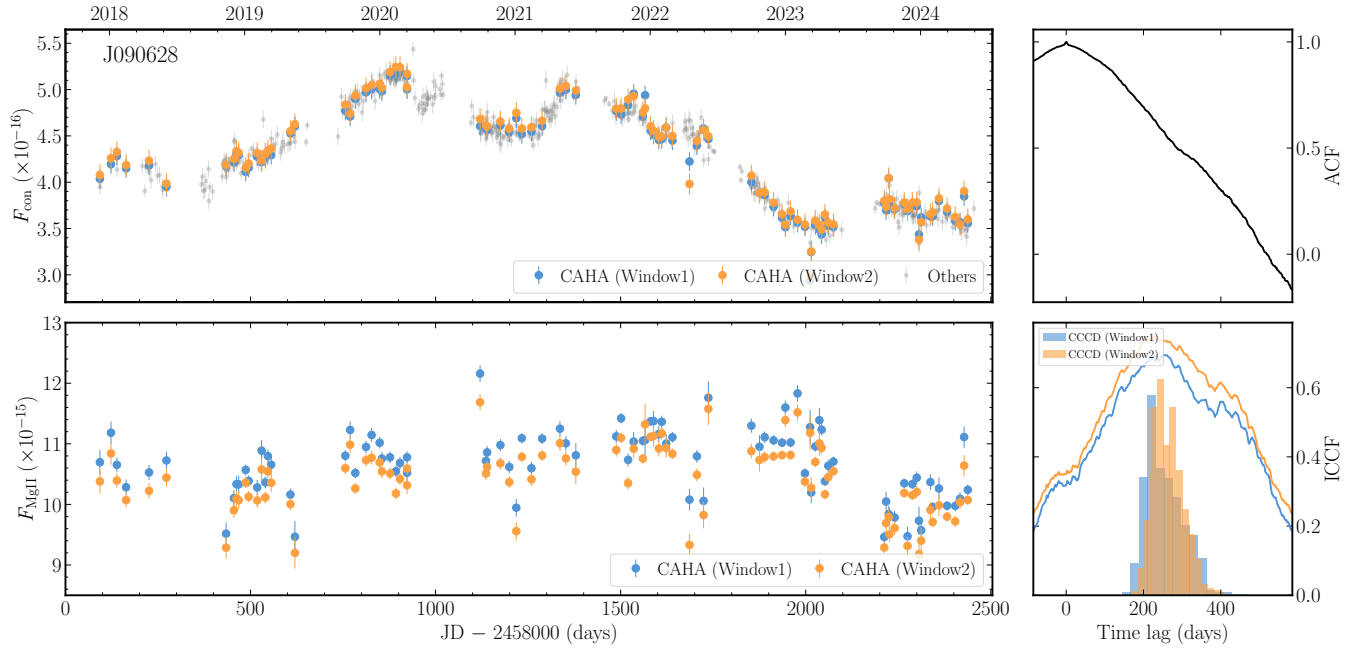


Figure 15. (Continued.)

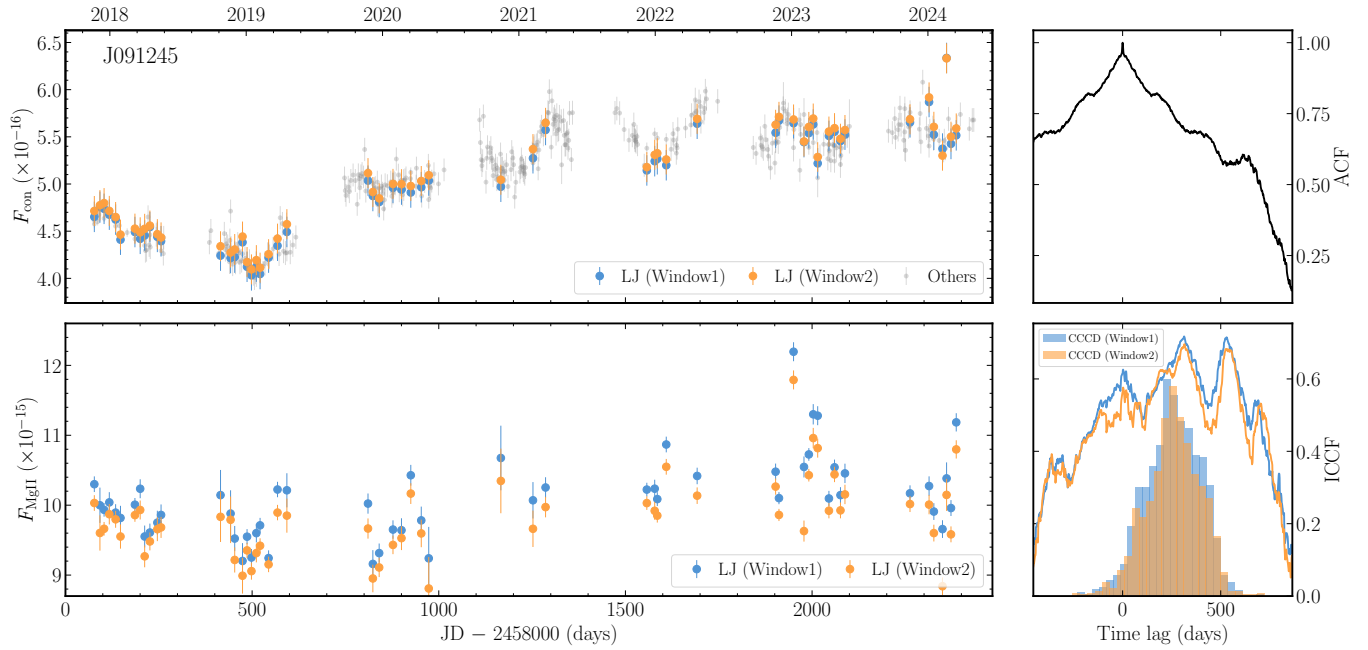


Figure 15. (Continued.)

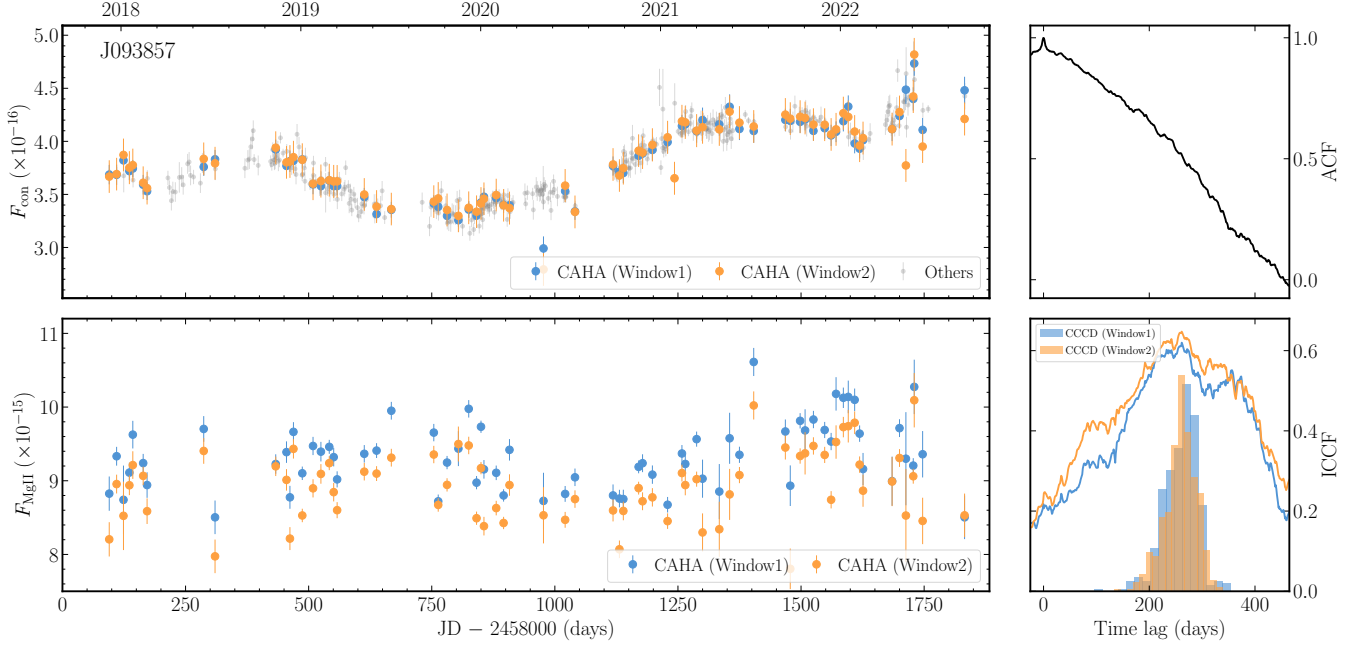


Figure 15. (Continued.)

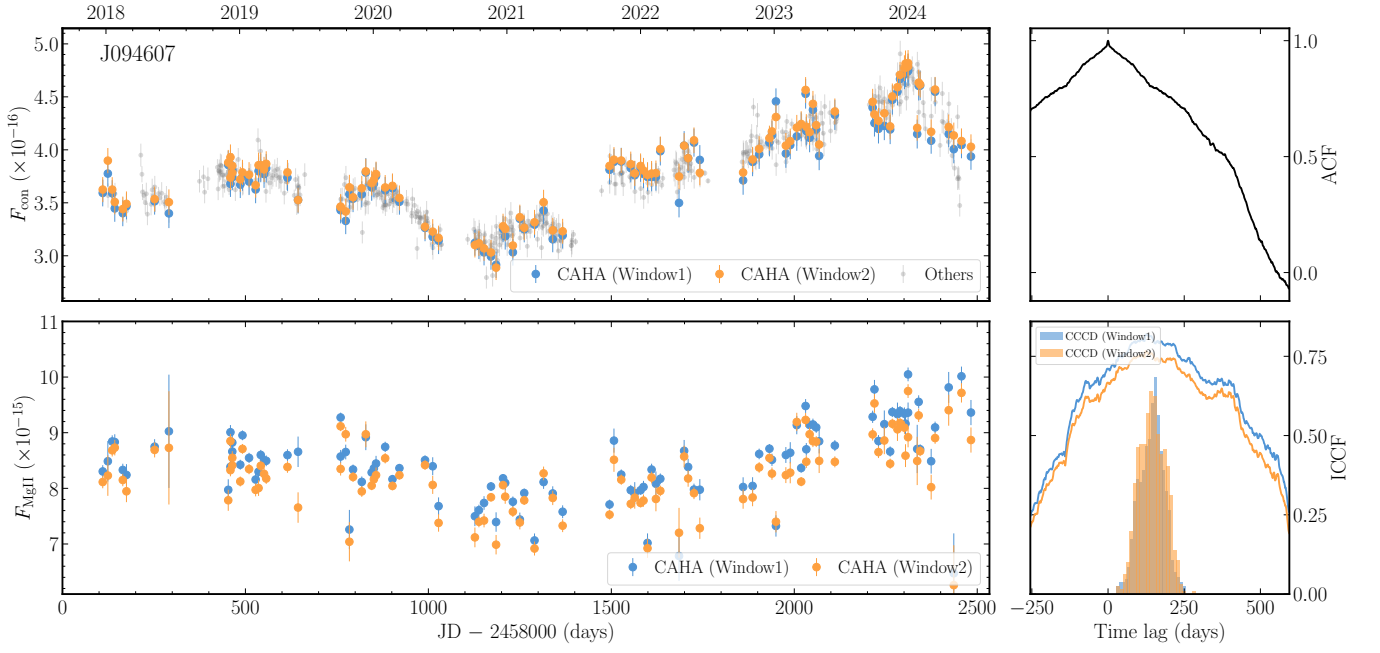


Figure 15. (Continued.)

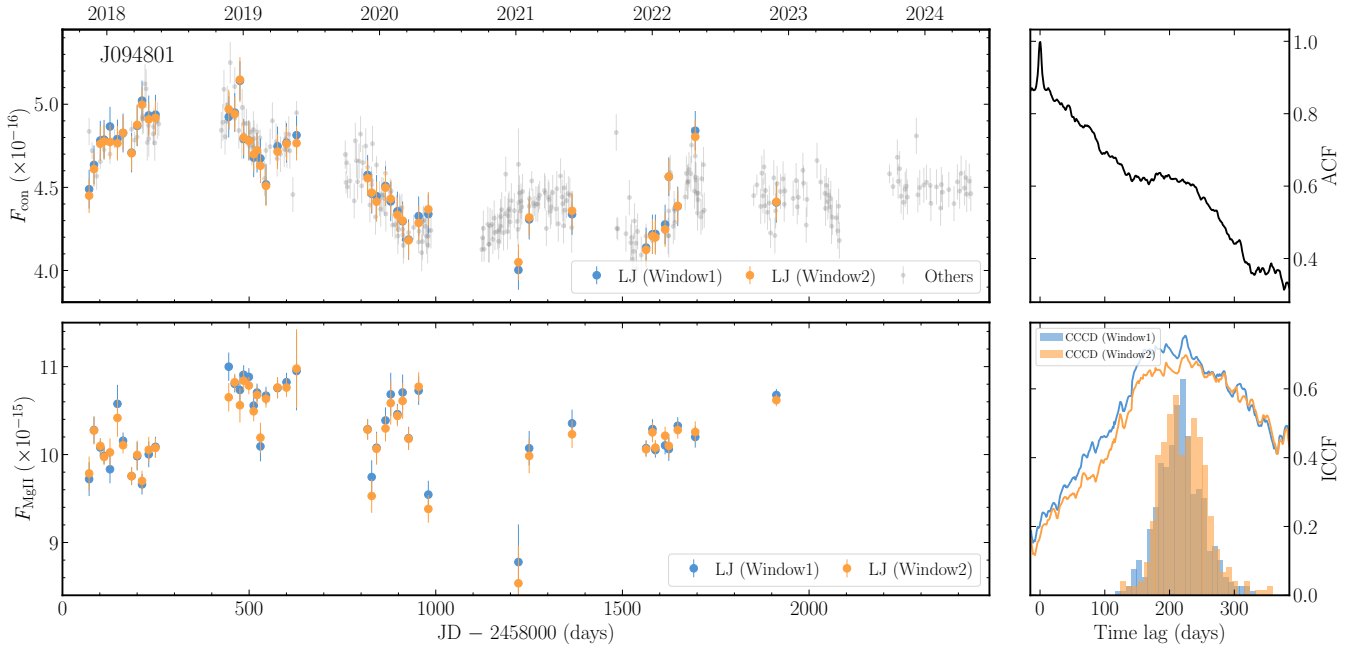


Figure 15. (Continued.)

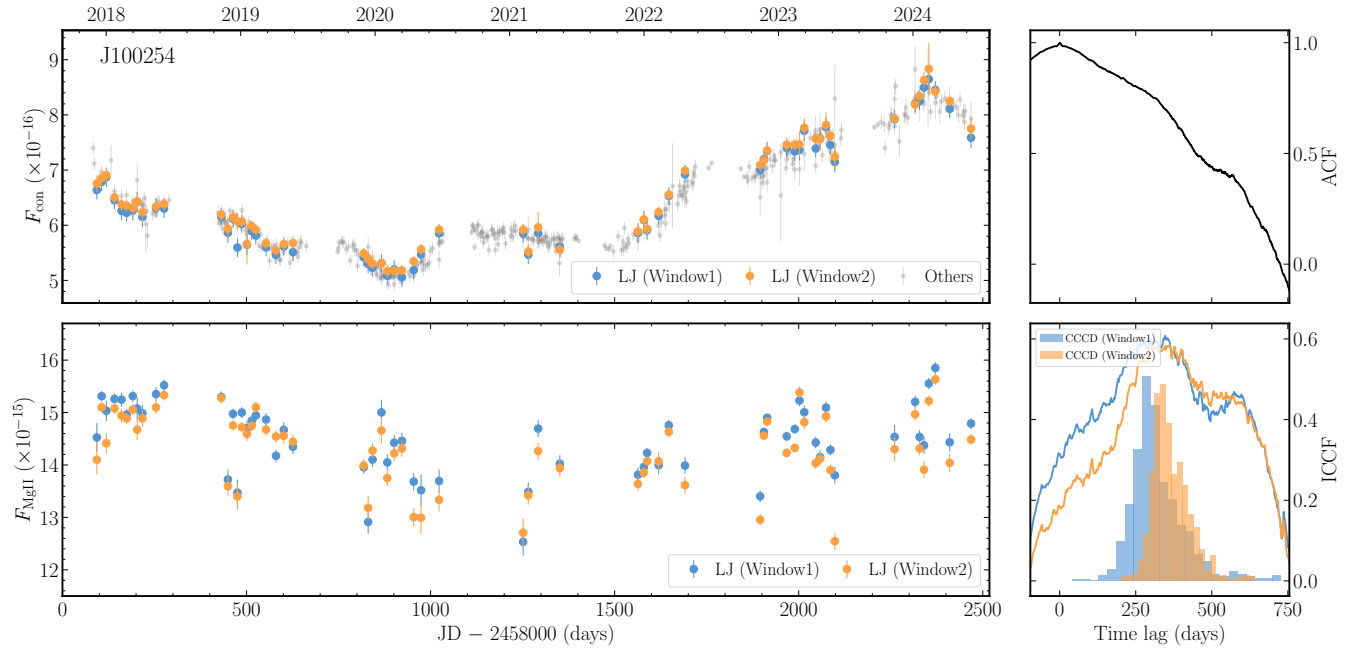


Figure 15. (Continued.)

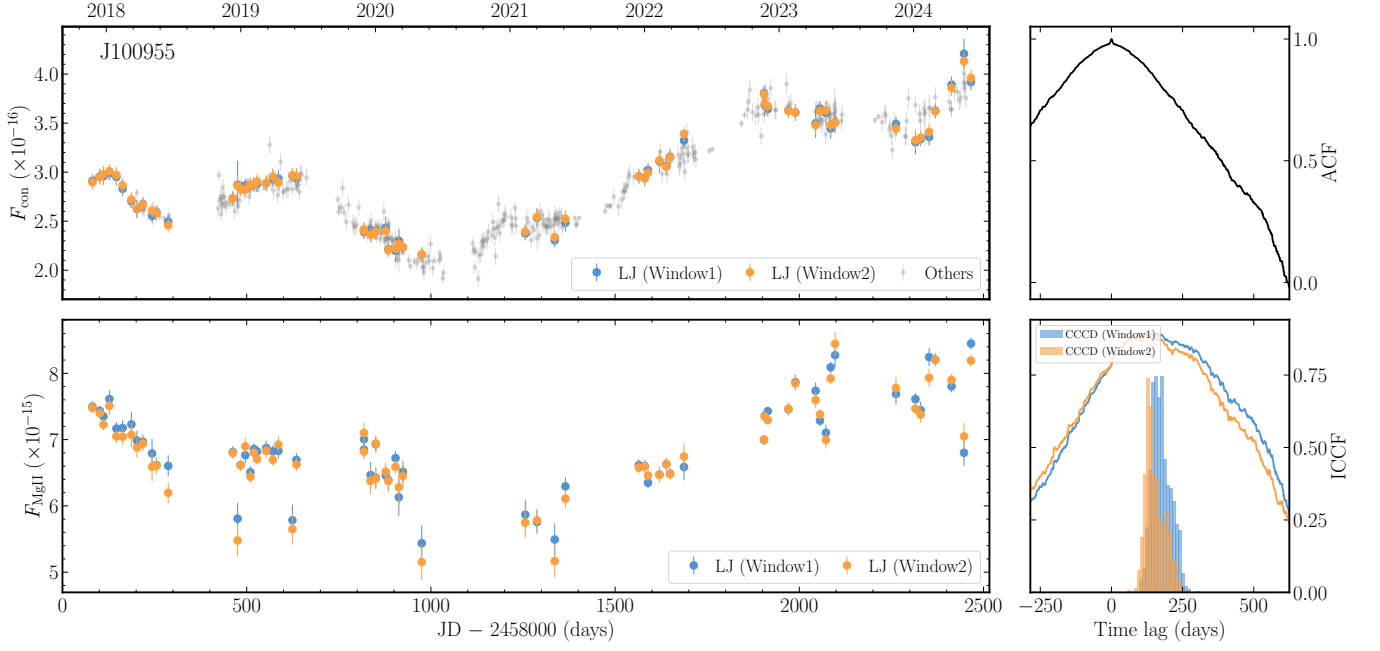


Figure 15. (Continued.)

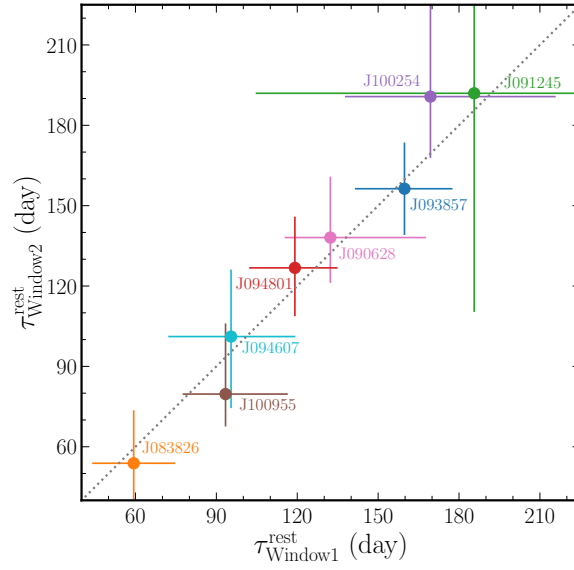


Figure 16. Comparison between the lag in the rest frame derived from the light curve using fitting range Window 1 ($\tau_{\text{Window1}}^{\text{rest}}$) and Window 2 ($\tau_{\text{Window2}}^{\text{rest}}$), via ICCF method.

Table 5. The results of partial correlation analysis between ΔR_{MgII} and $\log \mathcal{M}$ when taking the lag τ_{MgII} or the luminosity L_{3000} as a confounding variable. ρ and p are the partial correlation coefficient and the p -value, respectively.

Correlation	Confounding Variable	ρ	p
ΔR_{MgII} vs. $\log \mathcal{M}$	τ_{MgII}	-0.85	9.0×10^{-27}
	L_{3000}	-0.70	9.9×10^{-15}

Dong, X.-B., Wang, J.-G., Ho, L. C., et al. 2011, *ApJ*, 736, 2, 86. doi:10.1088/0004-637X/736/2/86

Du, P., Hu, C., Lu, K.-X., et al. 2014, *ApJ*, 782, 45. doi:10.1088/0004-637X/782/1/45

Du, P., Hu, C., Lu, K.-X., et al. 2015, *ApJ*, 806, 22. doi:10.1088/0004-637X/806/1/22

Du, P., Lu, K.-X., Zhang, Z.-X., et al. 2016a, *ApJ*, 825, 126. doi:10.3847/0004-637X/825/2/126

Du, P., Wang, J.-M., Hu, C., et al. 2016b, *ApJL*, 818, 1, L14. doi:10.3847/2041-8205/818/1/L14

Du, P., Lu, K.-X., Hu, C., et al. 2016c, *ApJ*, 820, 1, 27. doi:10.3847/0004-637X/820/1/27

Du, P., Zhang, Z.-X., Wang, K., et al. 2018a, *ApJ*, 856, 1, 6. doi:10.3847/1538-4357/aaae6b

Du, P., Brotherton, M. S., Wang, K., et al. 2018b, *ApJ*, 869, 142. doi:10.3847/1538-4357/aaed2c

Du, P. & Wang, J.-M. 2019, *ApJ*, 886, 42. doi:10.3847/1538-4357/ab4908

Du, P., Zhai, S., & Wang, J.-M. 2023, *ApJ*, 942, 112. doi:10.3847/1538-4357/aca52a

Du, P. 2024, Zenodo, v0.8.1. doi:10.5281/zenodo.12702951

Edelson, R., Turner, T. J., Pounds, K., et al. 2002, *ApJ*, 568, 610. doi:10.1086/323779

Fausnaugh, M. M., Denney, K. D., Barth, A. J., et al. 2016, *ApJ*, 821, 56. doi:10.3847/0004-637X/821/1/56

Ferrarese, L. & Ford, H. 2005, *SSRv*, 116, 523. doi:10.1007/s11214-005-3947-6

Gaskell, C. M. & Peterson, B. M. 1987, *ApJS*, 65, 1. doi:10.1086/191216

Goad, M. R., Koratkar, A. P., Axon, D. J., et al. 1999, *ApJL*, 512, L95. doi:10.1086/311884

GRAVITY Collaboration, Sturm, E., Dexter, J., et al. 2018, *Nature*, 563, 657. doi:10.1038/s41586-018-0731-9

GRAVITY Collaboration, Amorim, A., Bauböck, M., et al. 2020, *A&A*, 643, A154. doi:10.1051/0004-6361/202039067

GRAVITY Collaboration, Amorim, A., Bauböck, M., et al. 2021, *A&A*, 648, A117. doi:10.1051/0004-6361/202040061

Greene, J. E. & Ho, L. C. 2005, *ApJ*, 630, 122. doi:10.1086/431897

Grier, C. J., Peterson, B. M., Pogge, R. W., et al. 2012, *ApJ*, 755, 60. doi:10.1088/0004-637X/755/1/60

Grier, C. J., Martini, P., Watson, L. C., et al. 2013, *ApJ*, 773, 90. doi:10.1088/0004-637X/773/2/90

Guo, H., Shen, Y., He, Z., et al. 2020, *ApJ*, 888, 58. doi:10.3847/1538-4357/ab5db0

Ho, L. C., Goldoni, P., Dong, X.-B., et al. 2012, *ApJ*, 754, 1, 11. doi:10.1088/0004-637X/754/1/11

Ho, L. C. & Kim, M. 2014, *ApJ*, 789, 1, 17. doi:10.1088/0004-637X/789/1/17

Homayouni, Y., Trump, J. R., Grier, C. J., et al. 2020, *ApJ*, 901, 55. doi:10.3847/1538-4357/ababa9

Hryniewicz, K., Czerny, B., Pych, W., et al. 2014, *A&A*, 562, A34. doi:10.1051/0004-6361/201322487

Hu, C., Wang, J.-M., Ho, L. C., et al. 2008, *ApJ*, 687, 1, 78. doi:10.1086/591838

Hu, C., Du, P., Lu, K.-X., et al. 2015, *ApJ*, 804, 2, 138. doi:10.1088/0004-637X/804/2/138

Hu, C., Li, S.-S., Yang, S., et al. 2021, *ApJS*, 253, 20. doi:10.3847/1538-4365/abd774

Hu, C., Yao, Z.-H., Chen, Y.-J., et al. 2025, *ApJS*, 278, 2, 61. doi:10.3847/1538-4365/add40b

Jiang, D., Onoue, M., Jiang, L., et al. 2024, *ApJ*, 975, 2, 214. doi:10.3847/1538-4357/ad7d09

Kaspi, S., Smith, P. S., Netzer, H., et al. 2000, *ApJ*, 533, 631. doi:10.1086/308704

Kelly, B. C. 2007, *ApJ*, 665, 1489. doi:10.1086/519947

Khadka, N., Zajaček, M., Panda, S., et al. 2022, *MNRAS*, 515, 3, 3729. doi:10.1093/mnras/stac1940

Kokubo, M., Morokuma, T., Minezaki, T., et al. 2014, *ApJ*, 783, 46. doi:10.1088/0004-637X/783/1/46

Korista, K. T. & Goad, M. R. 2000, *ApJ*, 536, 284. doi:10.1086/308930

Korista, K. T. & Goad, M. R. 2004, *ApJ*, 606, 2, 749. doi:10.1086/383193

Kormendy, J. & Ho, L. C. 2013, *ARA&A*, 51, 511.

Kovačević-Dojčinović, J. & Popović, L. Č. 2015, *ApJS*, 221, 2, 35. doi:10.1088/0067-0049/221/2/35

Le, H. A. N., Woo, J.-H., & Xue, Y. 2020, *ApJ*, 901, 35. doi:10.3847/1538-4357/abada0

Li, Y.-R., Wang, J.-M., Hu, C., et al. 2014, *ApJL*, 786, L6. doi:10.1088/2041-8205/786/1/L6

Li, Y.-R., Wang, J.-M., & Bai, J.-M. 2016, *ApJ*, 831, 206. doi:10.3847/0004-637X/831/2/206

Li, Y.-R., Songsheng, Y.-Y., Qiu, J., et al. 2018, *ApJ*, 869, 2, 137. doi:10.3847/1538-4357/aaee6b

Li, Y.-R., Wang, J.-M., Songsheng, Y.-Y., et al. 2022, *ApJ*, 927, 1, 58. doi:10.3847/1538-4357/ac4bcb

Li, Y.-R. 2024a, Zenodo, v0.2.3. doi:10.5281/zenodo.10700132

Li, Y.-R. 2024b, Zenodo, v2.1.3. doi:10.5281/zenodo.11082109

- Li, Y.-R., Shangguan, J., Wang, J.-M., et al. 2025, *ApJ*, 988, 1, 42. doi:10.3847/1538-4357/addf40
- Lira, P., Kaspi, S., Netzer, H., et al. 2018, *ApJ*, 865, 56. doi:10.3847/1538-4357/aada45
- Maoz, D., Netzer, H., Leibowitz, E., et al. 1990, *ApJ*, 351, 75. doi:10.1086/168445
- Martínez-Aldama, M. L., Zajaček, M., Czerny, B., et al. 2020, *ApJ*, 903, 86. doi:10.3847/1538-4357/abb6f8
- Marziani, P., Sulentic, J. W., Zwitter, T., et al. 2001, *ApJ*, 558, 2, 553. doi:10.1086/322286
- Marziani, P., Sulentic, J. W., Plauchu-Frayn, I., et al. 2013, *A&A*, 555, A89. doi:10.1051/0004-6361/201321374
- Masci, F. J., Laher, R. R., Rusholme, B., et al. 2019, *PASP*, 131, 995, 018003. doi:10.1088/1538-3873/aae8ac
- McGill, K. L., Woo, J.-H., Treu, T., et al. 2008, *ApJ*, 673, 703. doi:10.1086/524349
- McLure, R. J. & Jarvis, M. J. 2002, *MNRAS*, 337, 109. doi:10.1046/j.1365-8711.2002.05871.x
- Mejía-Restrepo, J. E., Trakhtenbrot, B., Lira, P., et al. 2016, *MNRAS*, 460, 1, 187. doi:10.1093/mnras/stw568
- Metzroth, K. G., Onken, C. A., & Peterson, B. M. 2006, *ApJ*, 647, 901. doi:10.1086/505525
- Morton, D. C. 1991, *ApJS*, 77, 119. doi:10.1086/191601
- Onken, C. A. & Peterson, B. M. 2002, *ApJ*, 572, 746. doi:10.1086/340351
- Onken, C. A., Ferrarese, L., Merritt, D., et al. 2004, *ApJ*, 615, 2, 645. doi:10.1086/424655
- Pan, Z., Jiang, L., Guo, W.-J., et al. 2025, *ApJ*, 987, 1, 48. doi:10.3847/1538-4357/add7dd
- Pancoast, A., Brewer, B. J., & Treu, T. 2011, *ApJ*, 730, 2, 139. doi:10.1088/0004-637X/730/2/139
- Pancoast, A., Brewer, B. J., Treu, T., et al. 2014, *MNRAS*, 445, 3, 3073. doi:10.1093/mnras/stu1419
- Panda, S., Marziani, P., & Czerny, B. 2019, *ApJ*, 882, 2, 79. doi:10.3847/1538-4357/ab3292
- Peterson, B. M. 1993, *PASP*, 105, 247. doi:10.1086/133140
- Peterson, B. M., Wanders, I., Horne, K., et al. 1998, *PASP*, 110, 660. doi:10.1086/316177
- Peterson, B. M. & Wandel, A. 1999, *ApJL*, 521, L95. doi:10.1086/312190
- Peterson, B. M. & Wandel, A. 2000, *ApJL*, 540, L13. doi:10.1086/312862
- Peterson, B. M., Ferrarese, L., Gilbert, K. M., et al. 2004, *ApJ*, 613, 682. doi:10.1086/423269
- Planck Collaboration, Aghanim, N., Akrami, Y., et al. 2020, *A&A*, 641, A6. doi:10.1051/0004-6361/201833910
- Popović, L. Č., Kovačević-Dojčinović, J., & Marčeta-Mandić, S. 2019, *MNRAS*, 484, 3, 3180. doi:10.1093/mnras/stz157
- Press, W. H., Teukolsky, S. A., Vetterling, W. T., et al. 1992, , Numerical recipes in FORTRAN. The art of scientific computing.
- Prince, R., Zajaček, M., Czerny, B., et al. 2022, *A&A*, 667, A42. doi:10.1051/0004-6361/202243194
- Prince, R., Zajaček, M., Panda, S., et al. 2023, *A&A*, 678, A189. doi:10.1051/0004-6361/202346738
- Rakshit, S., Stalin, C. S., & Kotilainen, J. 2020, *ApJS*, 249, 1, 17. doi:10.3847/1538-4365/ab99c5
- Richards, G. T., Lacy, M., Storrie-Lombardi, L. J., et al. 2006, *ApJS*, 166, 470. doi:10.1086/506525
- Rodríguez-Pascual, P. M., Alloin, D., Clavel, J., et al. 1997, *ApJS*, 110, 9. doi:10.1086/312996
- Salviander, S., Shields, G. A., Gebhardt, K., et al. 2007, *ApJ*, 662, 131. doi:10.1086/513086
- Schlafly, E. F. & Finkbeiner, D. P. 2011, *ApJ*, 737, 2, 103. doi:10.1088/0004-637X/737/2/103
- Shen, Y., Greene, J. E., Strauss, M. A., et al. 2008, *ApJ*, 680, 169. doi:10.1086/587475
- Shen, Y., Richards, G. T., Strauss, M. A., et al. 2011, *ApJS*, 194, 45. doi:10.1088/0067-0049/194/2/45
- Shen, Y. & Liu, X. 2012, *ApJ*, 753, 2, 125. doi:10.1088/0004-637X/753/2/125
- Shen, Y. & Ho, L. C. 2014, *Nature*, 513, 7517, 210. doi:10.1038/nature13712
- Shen, Y., Horne, K., Grier, C. J., et al. 2016, *ApJ*, 818, 30. doi:10.3847/0004-637X/818/1/30
- Shen, Y., Hall, P. B., Horne, K., et al. 2019, *ApJS*, 241, 2, 34. doi:10.3847/1538-4365/ab074f
- Shen, Y., Grier, C. J., Horne, K., et al. 2024, *ApJS*, 272, 26. doi:10.3847/1538-4365/ad3936
- Shin, J., Nagao, T., Woo, J.-H., et al. 2019, *ApJ*, 874, 1, 22. doi:10.3847/1538-4357/ab05da
- Shin, J., Woo, J.-H., Nagao, T., et al. 2021, *ApJ*, 917, 2, 107. doi:10.3847/1538-4357/ac0adf
- Sulentic, J. W., Zwitter, T., Marziani, P., et al. 2000, *ApJL*, 536, 1, L5. doi:10.1086/312717
- Sun, M., Trump, J. R., Shen, Y., et al. 2015, *ApJ*, 811, 42. doi:10.1088/0004-637X/811/1/42
- Trevese, D., Paris, D., Stirpe, G. M., et al. 2007, *A&A*, 470, 491. doi:10.1051/0004-6361:20077237
- Tsuzuki, Y., Kawara, K., Yoshii, Y., et al. 2006, *ApJ*, 650, 57. doi:10.1086/506376
- U, V., Barth, A. J., Vogler, H. A., et al. 2022, *ApJ*, 925, 52. doi:10.3847/1538-4357/ac3d26
- Valdes, F., Gupta, R., Rose, J. A., et al. 2004, *ApJS*, 152, 2, 251. doi:10.1086/386343
- Verner, E. M., Verner, D. A., Korista, K. T., et al. 1999, *ApJS*, 120, 101. doi:10.1086/313171

- Vestergaard, M. & Wilkes, B. J. 2001, *ApJS*, 134, 1.
doi:10.1086/320357
- Vestergaard, M. & Peterson, B. M. 2006, *ApJ*, 641, 689.
doi:10.1086/500572
- Villafañã, L., Williams, P. R., Treu, T., et al. 2023, *ApJ*, 948, 2, 95.
doi:10.3847/1538-4357/accc84
- Wang, J.-G., Dong, X.-B., Wang, T.-G., et al. 2009, *ApJ*, 707, 1334. doi:10.1088/0004-637X/707/2/1334
- Wang, J.-M., Du, P., Hu, C., et al. 2014, *ApJ*, 793, 108.
doi:10.1088/0004-637X/793/2/108
- Wang, J.-M., Songsheng, Y.-Y., Li, Y.-R., et al. 2020, *Nature Astronomy*, 4, 517. doi:10.1038/s41550-019-0979-5
- Wills, B. J., Netzer, H., Uomoto, A. K., et al. 1980, *ApJ*, 237, 319.
doi:10.1086/157871
- Woo, J.-H. 2008, *AJ*, 135, 1849.
doi:10.1088/0004-6256/135/5/1849
- Woo, J.-H., Yoon, Y., Park, S., et al. 2015, *ApJ*, 801, 38.
doi:10.1088/0004-637X/801/1/38
- Woo, J.-H., Le, H. A. N., Karouzos, M., et al. 2018, *ApJ*, 859, 138.
doi:10.3847/1538-4357/aabf3e
- Woo, J.-H., Wang, S., Rakshit, S., et al. 2024, *ApJ*, 962, 67.
doi:10.3847/1538-4357/ad132f
- Yang, Q., Shen, Y., Chen, Y.-C., et al. 2020, *MNRAS*, 493, 5773.
doi:10.1093/mnras/staa645
- Yang, J., Wang, F., Fan, X., et al. 2023, *ApJL*, 951, L5.
doi:10.3847/2041-8213/acc9c8
- Yang, S., Du, P., & Wang, J.-M. 2024, *ApJS*, 274, 2, 24.
doi:10.3847/1538-4365/ad61e3
- Yu, Z., Martini, P., Penton, A., et al. 2021, *MNRAS*, 507, 3771.
doi:10.1093/mnras/stab2244
- Yu, Z., Martini, P., Penton, A., et al. 2023, *MNRAS*, 522, 4132.
doi:10.1093/mnras/stad1224
- Zajaček, M., Czerny, B., Martinez-Aldama, M. L., et al. 2020, *ApJ*, 896, 146. doi:10.3847/1538-4357/ab94ae
- Zajaček, M., Czerny, B., Martinez-Aldama, M. L., et al. 2021, *ApJ*, 912, 10. doi:10.3847/1538-4357/abe9b2
- Zhu, D., Sun, M., & Wang, T. 2017, *ApJ*, 843, 30.
doi:10.3847/1538-4357/aa76e7